Satellite-based Quantum Communications with Hybrid Protocols

Hung Do

A thesis in fulfilment of the requirements for the degree of

Doctor of Philosophy

School of Electrical Engineering and Telecommunications

Faculty of Engineering

The University of New South Wales

May 2022

THE UNIVERSITY OF NEW SOUTH WALES
Thesis/Dissertation Sheet

Surname or Family name: **Do**

First name: **Hung** Other name/s:

Abbreviation for degree as given in the University calendar: **PhD**

School: **School of Electrical Engineering and Telecommunications** Faculty: **Faculty of Engineering**

Title: Satellite-based Quantum Communications with Hybrid Protocols

Abstract

In many traditional quantum–information protocols, quantum entanglement is carried by either discrete variables (DV) or continuous variables (CV). In DV mode, the quantum information is usually encoded into the polarization or the number of photons. In CV mode, the quantum information is encoded into the quadrature of the optical field. Compared to DV protocols, CV protocols use homodyne (or heterodyne) detectors which are faster and more efficient. In the context of satellite communication, it is of great interest to interconnect terrestrial devices running on mixed technologies by exploring the use of hybrid teleportation protocols. As a proof of concept, the Micius experiment has demonstrated an experiment for QKD between a satellite in Low-Earth-Orbit (LEO), which is about 500km above the ground, and a ground station. However, the engineering and deployment of quantum satellite payloads are very challenging. Once the satellite is deployed, it is very difficult to modify the payload for different functionalities. Hybrid technologies, in contrast, can interoperate with both the DV and CV protocols. In this thesis, I investigate hybrid protocols where the teleportation channel is a CV entangled state (which will henceforth be called the CV channel) and apply them to different quantum communication protocols over long distances. In these protocols, instead of directly distributing quantum entanglement from the satellite (direct distribution scheme), where the transmission loss directly affects the DV modes, the CV channel is pre-distributed from the satellite to teleport different quantum states. As a result, the satellite loss enters indirectly through the teleportation channel. My first contribution shows that using a CV channel to transfer one mode of a DV entangled state yields higher entanglement quality than directly distributing the DV entanglement from the satellite. In my second contribution, by using the CV channel to teleport a Schrödinger's cat state, I also show that the teleportation protocol can preserve higher fidelity than a fixed-attenuation channel. In my last contribution, I investigate the teleportation of a hybrid entangled state over the CV channel. My results show that for the typical loss of the Satellite-Earth channel, teleportation is always better than direct distribution.

ORIGINALITY STATEMENT

☑ I hereby declare that this submission is my own work and to the best of my knowledge it contains no materials previously published or written by another person, or substantial proportions of material which have been accepted for the award of any other degree or diploma at UNSW or any other educational institution, except where due acknowledgement is made in the thesis. Any contribution made to the research by others, with whom I have worked at UNSW or elsewhere, is explicitly acknowledged in the thesis. I also declare that the intellectual content of this thesis is the product of my own work, except to the extent that assistance from others in the project's design and conception or in style, presentation and linguistic expression is acknowledged.

COPYRIGHT STATEMENT

☑ I hereby grant the University of New South Wales or its agents a non-exclusive licence to archive and to make available (including to members of the public) my thesis or dissertation in whole or part in the University libraries in all forms of media, now or here after known. I acknowledge that I retain all intellectual property rights which subsist in my thesis or dissertation, such as copyright and patent rights, subject to applicable law. I also retain the right to use all or part of my thesis or dissertation in future works (such as articles or books).

For any substantial portions of copyright material used in this thesis, written permission for use has been obtained, or the copyright material is removed from the final public version of the thesis.

AUTHENTICITY STATEMENT

☑ I certify that the Library deposit digital copy is a direct equivalent of the final officially approved version of my thesis.

UNSW is supportive of candidates publishing their research results during their candidature as detailed in the UNSW Thesis Examination Procedure.

Publications can be used in the candidate's thesis in lieu of a Chapter provided:

- The candidate contributed **greater than 50%** of the content in the publication and are the "primary author", i.e. they were responsible primarily for the planning, execution and preparation of the work for publication.
- The candidate has obtained approval to include the publication in their thesis in lieu of a Chapter from their Supervisor and Postgraduate Coordinator.
- The publication is not subject to any obligations or contractual agreements with a third party that would constrain its inclusion in the thesis.

☑ The candidate has declared that **some of the work described in their thesis has been published and has been documented in the relevant Chapters with acknowledgement**.

A short statement on where this work appears in the thesis and how this work is acknowledged within chapter/s:

> My thesis is partially comprised of three papers where I contributed as the first author. I performed all the calculations while the other authors contributed in terms of ideas, insights, and scientific arguments. Recognition of the work of the other authors has been made in my Acknowledgements section. The results from the "Hybrid Entanglement Swapping for Satellite-based Quantum Communications" paper, in the Proceedings of IEEE Globecom, are contained in parts in Chapters 3. The results from the "Teleportation of a Schrodinger's Cat State via Satellite-based Quantum Communications" paper, in the Proceedings of IEEE Globecom Workshop, are contained in parts in Chapters 4. The results from the "Satellite-based distribution of hybrid entanglement" paper, in the journal of Quantum Engineer, are contained in parts in Chapter 5.

Candidate's Declaration

I declare that I have complied with the Thesis Examination Procedure.

Acknowledgement

Firstly, I would like to express my sincere gratitude to my supervisors - Prof. Robert Malaney and Dr. Hendra Nurdin, for their continuous advice and guidance throughout my PhD candidature. I appreciate how they could inspire and correct my direction while still giving me enough freedom and flexibility to carry out my own research. I would like to express my very great appreciation to my collaborator - Dr. Jonathan Green from the Northrop Grumman Corporation - who provided expertise that greatly assisted the research and the writing up of the papers. I would also like to thank all the fellow PhD students - especially Ziqing, Mingjian, Xiaoyu, and Waheeda - for the insightful discussions and support, without which I would not be able to conceive ideas and solutions for my research problems.

Secondly, I would like to acknowledge the University International Postgraduate Award from UNSW, as well as the additional funding from the Northrop Grumman Corporation, which allowed me to pursue my PhD research and attend conferences in the USA.

Last but not the least, I would like to thank my family, especially my parents and my sister, for supporting me spiritually through all the ups and downs of these four years. The PhD was a very long commitment that requires some patience and determination to complete. The journey was difficult at times, however, at the end, I am very surprised and in awe of the depth and scale of research that I was able to achieve.

List of Publications

Publications with my major contribution:

- H. Do, R. Malaney and J. Green, "Hybrid Entanglement Swapping for Satellite-based Quantum Communications", Proceedings of IEEE Globecom, p. 1, 2019.
- H. Do, R. Malaney and J. Green, "Teleportation of a Schrodinger's Cat State via Satellite-based Quantum Communications", Proceedings of IEEE Globecom Workshop, p. 1, 2019.
- H. Do, R. Malaney and J. Green, "Satellite-based distribution of hybrid entanglement", Quantum Engineering, p. 776, 2021.

Publication not included in this thesis:

- R. Malaney, X. Ai, H. Do, M. He, E. Villasenor, Z. Wang and J. Green, "Quantum Communications: From Space to the Nano", Proceedings ACM International Conference on Nanoscale Computing and Communication, p. 1, 2019.

Abstract

In many traditional quantum–information protocols, quantum entanglement is carried by either discrete variables (DV) or continuous variables (CV). In DV mode, the quantum information is usually encoded into the polarization or the number of photons. In CV mode, the quantum information is encoded into the quadrature of the optical field. Compared to DV protocols, CV protocols use homodyne (or heterodyne) detectors which are faster and more efficient. In the context of satellite communication, it is of great interest to interconnect terrestrial devices running on mixed technologies by exploring the use of hybrid teleportation protocols. As a proof of concept, the Micius experiment has demonstrated an experiment for QKD between a satellite in Low-Earth-Orbit (LEO), which is about 500km above the ground, and a ground station. However, the engineering and deployment of quantum satellite payloads are very challenging. Once the satellite is deployed, it is very difficult to modify the payload for different functionalities. Hybrid technologies, in contrast, can interoperate with both the DV and CV protocols. In this thesis, I investigate hybrid protocols where the teleportation channel is a CV entangled state (which will henceforth be called the CV channel) and apply them to different quantum communication protocols over long distances. In these protocols, instead of directly distributing quantum entanglement from the satellite (direct distribution scheme), where the transmission loss directly affects the DV modes, the CV channel is pre-distributed from the satellite to teleport different quantum states. As a result, the satellite loss enters indirectly through the teleportation channel. My first contribution shows that using a CV channel to transfer one mode of a DV entangled state yields higher entanglement quality than directly distributing the DV entanglement from the satellite. In my second contribution, by using the CV channel to teleport a Schrödinger's cat state, I also show that the teleportation protocol can preserve higher fidelity than a fixed-attenuation channel. In my last contribution, I investigate the teleportation of a hybrid entangled state over the CV channel. My results show that for the typical loss of the Satellite-Earth channel, teleportation is always better than direct distribution.

Contents

List of Figures

Abbreviations

BSM	Bell-State Measurement
CV	Continuous Variable
DV	Discrete Variable
LEO	Low-Earth Orbit
QKD	Quantum Key Distribution
SMSV	Single-Mode Squeezed Vacuum
TMSV	Two-Mode Squeezed Vacuum

Chapter 1

Introduction, thesis outlines and contributions

1.1 Introduction

In quantum communication, the information can be encoded by either discrete variables (DVs) or continuous variables (CVs), analogous to discrete and analog signals in traditional electronics. DVs are comprised of discrete degrees of freedom such as the polarization or the number of the photons, while CVs refer to continuous degrees of freedom like the quadratures (position and momentum) of the optical field.

In this thesis, I investigate a CV teleportation channel with hybrid protocols to interface two different technologies - DV and CV. I then apply these protocols to quantum communication over long distances, taking into account the imperfection in the channels. Specifically, I study the channel loss in the context of a satellite in Low-Earth Orbit (LEO). The mathematical models in this thesis remain general enough for other applications with different types of channel loss.

1.2 Thesis outlines and contributions

In chapter 2, I review some basic quantum mechanical concepts relevant to my thesis. In chapter 3, I study the CV teleportation channel created between two ground receivers via direct lossy-distribution from a LEO satellite. Such a flexible teleportation protocol has the potential to interconnect a global array of quantum-enabled devices regardless of the different intrinsic technology upon which the devices are built. However, past studies of hybrid entanglement swapping have not accounted for channel transmission loss. Here I derive the general framework for teleporting an arbitrary input mode over a lossy CV teleportation channel. I investigate the specific case where the input modes are part of DV states entangled in the photon number basis, then identify the optimal teleportation strategy. My results show that, relative to DV photon-number entanglement sourced directly from the satellite, there are circumstances where my teleported DV states retain higher entanglement quality. I discuss the implications of my new results in the context of generating a global network of ultra-secure communications between different quantum-enabled devices which possess line-of-sight connections to LEO satellites. Specifically, I illustrate the impact the teleportation process has on the key rates from a Quantum Key Distribution (QKD) protocol. The main contents of this chapter have resulted in the following publication:

- H. Do, R. Malaney and J. Green, "Hybrid Entanglement Swapping for Satellite-based Quantum Communications", Proceedings of IEEE Globecom, p. 1, 2019.

In chapter 4, I study the CV teleportation of the cat state via a satellite in LEO. Past studies have shown that the quantum character of the cat state can be preserved after CV teleportation, even when taking into account the detector efficiency. However, the channel transmission loss has not been taken into consideration. Traditionally, optical fibers with fixed attenuation are used as teleportation channels. My results show that in such a setup, the quantum character of the cat state is lost after 5dB of channel loss. I then investigate the free-space channel between the Earth and a satellite, where the loss is caused by atmospheric turbulence. For a down-link channel of less than 500km and

30dB of loss, I find that the teleported state preserves higher fidelity relative to a fixed attenuation channel. The results in this work will be important for deployments over Earth-Satellite channels of protocols dependent on cat-state qubits. The main contents of this chapter have resulted in the following publication:

- H. Do, R. Malaney and J. Green, "Teleportation of a Schrodinger's Cat State via Satellite-based Quantum Communications", Proceedings of IEEE Globecom Workshop, p. 1, 2019.

In chapter 5, I explore, for the first time, the use of Two-Mode Squeezed Vacuum (TMSV) states, distributed from satellites, as a teleportation resource for the re-distribution of my candidate hybrid entanglement pre-stored within terrestrial quantum networks. I determine the loss conditions under which teleportation via the TMSV resource outperforms direct-satellite distribution of the hybrid entanglement, in addition to quantifying the advantage of teleporting the DV mode relative to the CV mode. My detailed calculations show that under the loss conditions anticipated from LEO, DV teleportation via the TMSV resource will always provide for significantly improved outcomes, relative to other means for distributing hybrid entanglement within heterogeneous quantum networks. The main contents of this chapter have resulted in the following publication:

- H. Do, R. Malaney and J. Green, "Satellite-based distribution of hybrid entanglement", Quantum Engineering, p. 776, 2021.

In chapter 6, I will conclude the thesis, identify some general problems, and propose some potential directions for future work.

For the ease of understanding of the reader, it is important to mention that some variable names used in each chapter might not correlate to the variables using the same letter or symbol in other chapters; they are confined to each chapter solely.

Chapter 2

Background

2.1 Discrete Variable (DV) and Continuous Variable (CV)

In quantum physics, information can be encoded in either DV or CV. DV refers to a degree of freedom with a finite number of discrete values, such as the polarization or number of photons. On the other hand, CV refers or a continuous degree of freedom, such as the position or momentum (quadratures) of the optical field. In this section, I will introduce both types of encoding and discuss the method to measure the quadratures of the state.

2.1.1 DV in the photon number basis

For an optical field with frequency ω, the quantum harmonic oscillator can be expressed by the Hamiltonian [1, 2]

$$\hat{H} = \hbar\omega \left(\hat{n} + \frac{1}{2} \right), \tag{2.1}$$

where $\hbar$ is the Plank constant and $\hat{n}$ is the photon number operator. We have $\hat{n} = \hat{a}^\dagger \hat{a}$, where $\hat{a}^\dagger$ and $\hat{a}$ are the creation and annihilation operator, respectively. The solution of the quantum harmonic oscillator are the Fock states $\{|n\rangle\}$ with $n \in \mathbb{N}$, and

$$\hat{a}^\dagger |n\rangle = \sqrt{n+1}|n+1\rangle, \quad \hat{a}|n\rangle = \sqrt{n}|n-1\rangle. \tag{2.2}$$

The photon number basis is a DV degree of freedom.

2.1.2 CV in the field quadratures

In classical electromagnetism, the CVs are the amplitude and phase of the electric field. In quantum optics, CVs refer to the quadratures (position and momentum) of the state. The most basic CV state is the coherent state, which is the eigenstate ($|\alpha\rangle$) of the annihilator operator $\hat{a}$

$$\hat{a}|\alpha\rangle = \alpha|\alpha\rangle, \tag{2.3}$$

where α is a complex number analogous to the amplitude of a coherent laser field.

Another type of CV state is the Schrödenger's cat state, which is a superposition of coherent states with opposite amplitude

$$|cat_{\pm}\rangle = \frac{|\alpha\rangle \pm |-\alpha\rangle}{N_{\pm}}, \tag{2.4}$$

with $N_{\pm}$ being the normalization factor

$$N_{\pm} = \sqrt{2 \pm 2e^{-2|\alpha|^2}}. \tag{2.5}$$

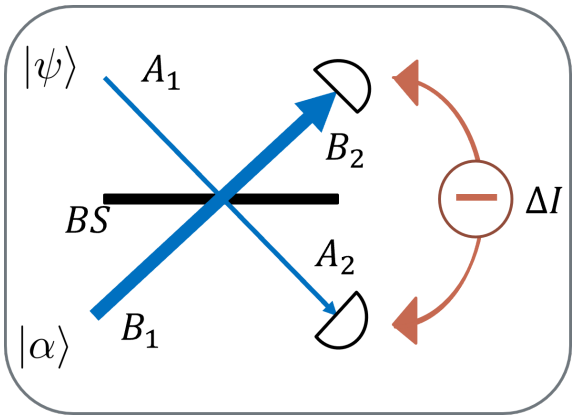

Figure 2.1: Diagram of the homodyne measurement to measure the field quadratures. The input signal (A_1) and the local oscillator (B_1) interfere through a balanced beam splitter. The intensity difference ($\Delta I \equiv I_{A_2} - I_{B_2}$) is measured between the two photodetectors, giving information about the quadratures.

Alternatively, we can express the creation and annihilation operators by the position and

momentum operators [2, 3]

$$\hat{a} = \frac{1}{\sqrt{2\hbar\omega}}(\omega\hat{X} + j\hat{P}), \quad \hat{a}^\dagger = \frac{1}{\sqrt{2\hbar\omega}}(\omega\hat{X} - j\hat{P}), \tag{2.6}$$

where j is the imaginary unit. By letting $\hbar = \frac{1}{2}$, we define the dimensionless position and momentum operators

$$\hat{x} = \frac{\hat{a} + \hat{a}^\dagger}{2}, \quad \hat{p} = \frac{\hat{a} - \hat{a}^\dagger}{2j}. \tag{2.7}$$

The generalized quadrature operator is given by

$$\begin{aligned} \hat{Q}(\theta) &= \hat{x}\, cos\theta + \hat{p}\, sin\theta \\ &= \frac{e^{j\theta}\hat{a}^\dagger + e^{-j\theta}\hat{a}}{2}. \end{aligned} \tag{2.8}$$

When $\theta = 0$, the quadrature becomes the position ($\hat{Q}(0) = \hat{x}$), and when $\theta = \frac{\pi}{2}$, the quadrature becomes the momentum ($\hat{Q}(\frac{\pi}{2}) = \hat{p}$).

The quadratures of the states can be measured by homodyne measurements as in Fig. 2.1. In the homodyne measurement scheme, the state to be measure $|\psi\rangle$ is sent through mode A_1, and a strong coherent state $|\alpha\rangle$ is sent through mode B_1. These two modes are combined at the beam splitter of phase θ, giving

$$\begin{aligned} \hat{a}^\dagger_{A_2} &= \frac{\hat{a}^\dagger_{A_1} + e^{j\theta}\hat{a}^\dagger_{B_1}}{\sqrt{2}}, \\ \hat{a}^\dagger_{B_2} &= \frac{-\hat{a}^\dagger_{A_1} + e^{j\theta}\hat{a}^\dagger_{B_1}}{\sqrt{2}}. \end{aligned} \tag{2.9}$$

The intensities in modes A_2 and B_2 are given by

$$\begin{aligned} I_{i_2} &= \hat{a}^\dagger_{i_2}\hat{a}_{i_2} \\ &= \frac{\hat{a}^\dagger_{A_1}\hat{a}_{A_1} + \hat{a}^\dagger_{B_1}\hat{a}_{B_1}}{2} \pm \frac{e^{j\theta}\hat{a}_{A_1}\hat{a}^\dagger_{B_1} + e^{-j\theta}\hat{a}^\dagger_{A_1}\hat{a}_{B_1}}{2}, \end{aligned} \tag{2.10}$$

where $i_2 \in \{A_2, B_2\}$, while the $\pm$ sign represents $+$ for mode A_2 and $-$ for mode B_2. The difference in intensity is given by

$$\Delta I \equiv I_{A_2} - I_{B_2} = e^{j\theta}\hat{a}_{A_1}\hat{a}^\dagger_{B_1} + e^{-j\theta}\hat{a}^\dagger_{A_1}\hat{a}_{B_1}. \tag{2.11}$$

From the input states, the expectation value of this operator is given by

$$\langle\psi, \alpha|\Delta I|\psi, \alpha\rangle = 2\alpha\langle\psi|e^{j\theta}\hat{a}_{A_1} + e^{-j\theta}\hat{a}^\dagger_{B_1}|\psi\rangle = 2\alpha\langle\hat{Q}(-\theta)\rangle. \tag{2.12}$$

From Eq. (2.8), when $\theta = 0$, $\langle \hat{Q}(-\theta) \rangle$ becomes the expectation value of the position $\langle \hat{x} \rangle$, and when $\theta = \pi/2$, $\langle \hat{Q}(-\theta) \rangle$ becomes the expectation value of the momentum $\langle \hat{p} \rangle$.

2.2 Entanglement

In this section, I introduce different types of bipartite entanglement between two spatial modes A and B, and then present how they are generated.

2.2.1 DV entanglement

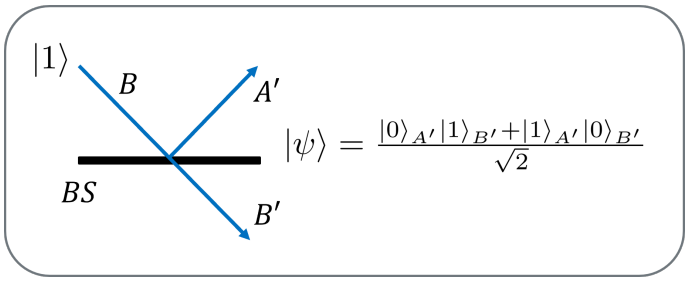

Figure 2.2: A photon-number-based DV entangled state can be produced by letting a single photon through a beam splitter.

In this thesis, I use DV entanglement that is based on the photon-number basis, so that it can interface easily with CV entangled states. Photon-number entanglement can be easily generated by letting a single photon through a beam splitter as illustrated in Fig. 2.2. When a single photon in mode B incidents on a beam splitter with transmissivity T, the transformation can be written as

$$|1\rangle_B = \hat{a}_B^\dagger |0\rangle_B \rightarrow \left(\sqrt{T}\hat{a}_{B'}^\dagger + \sqrt{1-T}\hat{a}_{A'}^\dagger\right)|0\rangle_{A'}|0\rangle_{B'}. \tag{2.13}$$

When the beam splitter is balanced, $T = 1/\sqrt{2}$, the resulting entangled state becomes

$$|\psi\rangle = \frac{|0\rangle_{A'}|1\rangle_{B'} + |1\rangle_{A'}|0\rangle_{B'}}{\sqrt{2}}. \tag{2.14}$$

Thus, if there is one photon in the spatial mode A', there must be no photon in the spatial mode B', and vice versa.

2.2.2 CV entanglement

Theoretically, the CV entangled state can be described by applying a two-mode squeezing operator on a two-mode vacuum state, thereby obtaining a TMSV state [1,2]

$$|TMSV\rangle = S(\xi)|0,0\rangle = \exp\left(\xi\hat{a}_A^\dagger\hat{a}_B^\dagger - \xi^*\hat{a}_A\hat{a}_B\right)|0,0\rangle_{ab}, \tag{2.15}$$

where $\xi = re^{i\phi}$, with r being the two-mode squeezing parameter (henceforth referred to as the initial squeezing), and ϕ being the phase. $\hat{a}_l$ and $\hat{a}_l^\dagger$ represent the annihilation and creation operators of the optical field, respectively, with $l \in \{A, B\}$ denoting the spatial modes. After expanding the exponential, we have

$$\begin{aligned} |TMSV\rangle &= \frac{1}{\cosh r}\sum_{n=0}^{\infty} e^{jn\phi}(\tanh r)^n|n\rangle_A|n\rangle_B \\ &= \sqrt{1-q^2}\sum_{n=0}^{\infty} q^n|n\rangle_A|n\rangle_B, \end{aligned} \tag{2.16}$$

where we have defined $q = \tanh r$ and set $\phi = 0$. Thus, if there are n photons in mode A, there must be n photons in mode B, and vice versa.

Experimentally, a TMSV state can be generated by letting two single-mode squeezed vacuum states (SMSV) through a balanced beam splitter [(1)]. Let $\hat{c}$ and $\hat{d}$ be the annihilator operators of the two SMSV input modes

$$|SMSV\rangle_l = \exp\left(-\frac{\xi}{2}\hat{l}^{\dagger 2} + \frac{\xi^*}{2}\hat{l}^{\,2}\right)|0\rangle_l, \tag{2.17}$$

where $l \in \{c, d\}$. The modes after the beam splitter are given by

$$\hat{a} = \frac{\hat{c}+\hat{d}}{\sqrt{2}}, \quad \hat{b} = \frac{\hat{d}-\hat{c}}{\sqrt{2}}. \tag{2.18}$$

We have

$$\frac{\hat{d}^2 - \hat{c}^2}{2} = \hat{a}\hat{b}, \tag{2.19}$$

[(1)]In this paper, I assume that there is no loss at this beam splitter. When the loss is taken into account, see [4].

thus

$$
\begin{aligned}
&|SMSV\rangle_c|SMSV\rangle_d \\
&= \exp\left(-\frac{\xi}{2}\hat{c}^{\dagger 2} + \frac{\xi^*}{2}\hat{c}^2\right)|0\rangle_c \exp\left(\frac{\xi}{2}\hat{d}^{\dagger 2} - \frac{\xi^*}{2}\hat{d}^2\right)|0\rangle_d \\
&= \exp\left(\xi\hat{a}^\dagger\hat{b}^\dagger - \xi^*\hat{a}\hat{b}\right)|0,0\rangle_{ab} \\
&= |TMSV\rangle_{ab}\,.
\end{aligned} \tag{2.20}
$$

2.2.3 Hybrid entanglement

Hybrid entanglement is the entanglement between a DV mode and a CV mode. In this thesis, I focus on the entanglement between cat states and qubit states

$$|\psi\rangle_h = \frac{|cat_-\rangle_C|0\rangle_D + |cat_+\rangle_C|1\rangle_D}{\sqrt{2}}, \tag{2.21}$$

where $|0\rangle$ and $|1\rangle$ are the vacuum state and the single photon state in the photon-number basis, while the Schrödinger cat states are given by Eq. (2.4).

Hybrid entanglement with large cat states can be deterministically generated by a weak and dispersive light-matter interaction [5], or by a cross-Kerr nonlinear interaction between a coherent state and a photon-number qubit state [6, 7]. However, due to experimental challenges in nonlinear optics, hybrid entanglement with small cat states can be more easily produced by using linear optics and a probabilistic heralded scheme [8–11]. The latter setup takes a small cat state ($|cat_+\rangle$) as an input, then produces hybrid entanglement between small cat states and qubit states (see Fig. (2.3)). The advantage of the heralded scheme is that the loss in the heralding channel only affects the success rate but not the fidelity of the final entanglement. Such a scheme is particularly beneficial for long-distance communication [10]. In addition, the heralded setup in [9] has the potential to be extended for cat states with higher amplitudes.

In the following, I present the mathematical details of the heralded generation of hybrid entanglement [10] as depicted in Fig. 2.3. A small-amplitude Schrödenger's cat state is

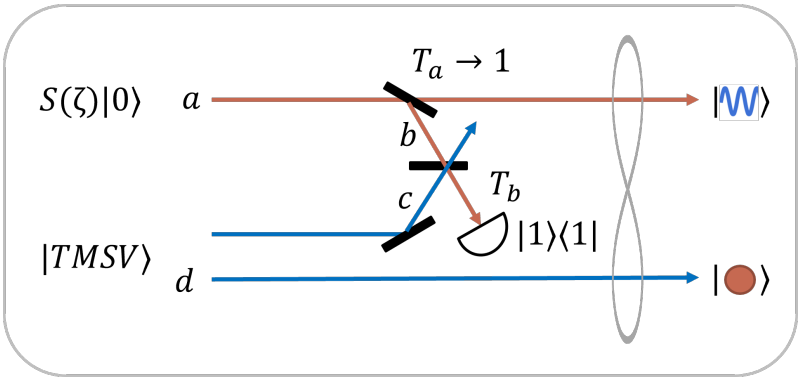

Figure 2.3: The heralded scheme to generate hybrid entanglement probabilistically.

approximated by a squeezed vacuum state

$$|cat_+\rangle \approx \hat{S}|0\rangle, \tag{2.22}$$

and is injected into mode a. A small fraction of light is reflected from mode a with an amplitude reflectivity of

$$r_a = \sin(\theta) \approx \theta \ll 1. \tag{2.23}$$

Let the beam splitter operator be

$$\hat{B}(\theta) = e^{\theta\left(\hat{a}\hat{b}^\dagger - \hat{a}^\dagger\hat{b}\right)}, \tag{2.24}$$

the states of mode a and b after the beam splitter is

$$\hat{B}(\theta)|cat_+\rangle_a|0\rangle_b \approx (1 + \theta\hat{a}\hat{b}^\dagger)|cat_+\rangle_a|0\rangle_b. \tag{2.25}$$

The input in modes c and d is a TMSV state with a small squeezing factor $\lambda \ll 1$

$$|TMSV\rangle_{c,d} \approx |0\rangle_c|0\rangle_d + \lambda|1\rangle_c|1\rangle_d = (1 + \lambda\hat{c}^\dagger\hat{d}^\dagger)|0\rangle_c|0\rangle_d\,. \tag{2.26}$$

Mode b and c are combined through a beam splitter with the transformations

$$\hat{b}^\dagger \to t\hat{b}^\dagger + r\hat{c}^\dagger, \quad \hat{c} \to r\hat{b}^\dagger - t\hat{c}^\dagger, \tag{2.27}$$

resulting in the four-mode state

$$\left(1 + \theta r\hat{a}\hat{c}^\dagger + \theta t\hat{a}\hat{b}^\dagger\right)\left(1 - \lambda t\hat{c}^\dagger\hat{d}^\dagger + \lambda r\hat{b}^\dagger\hat{d}^\dagger\right)|cat_+\rangle_a|0,0,0\rangle_{bcd}\,. \tag{2.28}$$

We then place a single-photon detector at mode b, where each detection will herald a hybrid entangled state on mode a and d. Mathematically, we perform a projection into the subspace where there is only one photon in mode b, then trace out mode c and keep only the first-order terms of θ and λ, giving

$$\begin{aligned} |\psi\rangle_{ab} &= \theta t \hat{a}|cat_+\rangle_a|0\rangle_d + \lambda r|cat_+\rangle_a|1\rangle_d \\ &= \frac{\theta t \alpha N_-|0\rangle_d|cat_-\rangle_a + \lambda r N_+|1\rangle_d|cat_+\rangle_a}{N_+}\,, \end{aligned} \tag{2.29}$$

where we have substituted $\hat{a}|cat_+\rangle = \alpha\frac{N_-}{N_+}|cat_-\rangle$. By adjusting the transmissivity and reflectivity of the beam splitter, we achieve a balanced hybrid state

$$|\psi\rangle_{ab} = \frac{|0\rangle_d|cat_-\rangle_a + |1\rangle_d|cat_+\rangle_a}{\sqrt{2}}\,. \tag{2.30}$$

2.3 Applications of hybrid entanglement as DV/CV qubit converter

Hybrid entanglement can be applied to transfer quantum information from DV encoding to CV encoding [10] and vice versa [12]. In such protocols, the hybrid entangled state acts as a bi-directional teleportation channel which can teleport information from a DV qubit to a CV qubit and vice versa.

2.3.1 Conversion from DV to CV qubit

The protocol for converting DV to CV encoding is outlined in Fig. 2.4a. The hybrid entangled state is first generated from an even cat state and a TMSV state by a heralded scheme. The DV mode of the hybrid state (mode A) is then combined with the DV qubit (mode C) through a beam splitter. The detection of a single photon on one of the output ports of the beam splitter will herald a CV qubit in mode B.

In this setting, the hybrid entangled state is initially in mode $A-B$, while the single DV

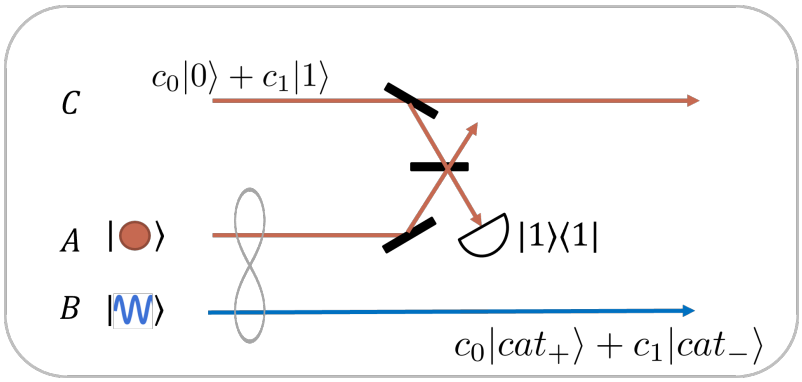

(a) DV to CV

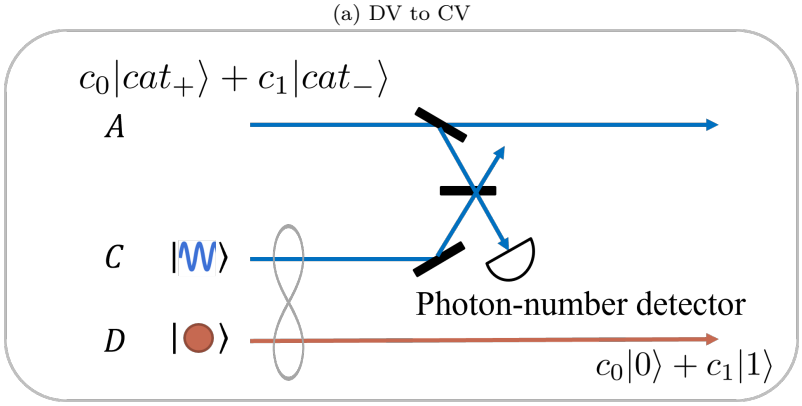

(b) CV to DV

Figure 2.4: The interconversion between DV and CV encoding is assisted by a hybrid entangled state. (a) Conversion from DV to CV encoding. (b) Conversion from CV to DV encoding.

.

qubit is in mode C

$$|\phi\rangle_C = c_0|0\rangle_C + c_1|1\rangle_C, \quad \rho_C = |\phi\rangle_C\langle\phi|. \tag{2.31}$$

The combined state is

$$\frac{1}{\sqrt{2}}(|0\rangle_A|cat_-\rangle_B + |1\rangle_A|cat_+\rangle_B) \otimes (c_0|0\rangle_C + c_1|1\rangle_C). \tag{2.32}$$

After we combine mode A and C through a beam splitter, we have the transformation

$$\begin{aligned} |1\rangle_A = \hat{a}^\dagger|0\rangle_A &\to \frac{\hat{a}^\dagger + \hat{c}^\dagger}{\sqrt{2}}|0\rangle_A, \\ |1\rangle_C = \hat{c}^\dagger|0\rangle_C &\to \frac{\hat{c}^\dagger - \hat{a}^\dagger}{\sqrt{2}}|0\rangle_C, \end{aligned} \tag{2.33}$$

where $\hat{a}^\dagger$ and $\hat{c}^\dagger$ represent the creation operators of modes A and C, respectively. After projecting onto the subspace where mode C has single photon, the combined state then

becomes

$$\frac{1}{2}(c_0|cat_+\rangle_B + c_1|cat_-\rangle_B) \otimes |0\rangle_A. \tag{2.34}$$

Thus, we have a corresponding DV qubit in mode B.

2.3.2 Conversion from CV to DV qubit

The protocol for converting CV to DV encoding is outlined in Fig. 2.4b. After the preparation of the hybrid entangled state $C - D$, the CV mode C is mixed with the input CV qubit A by a beam splitter. The detection of a single photon on one of the output ports of the beam splitter will herald a DV qubit in mode D.

The beam splitter perform the following transformations

$$\begin{aligned} |\alpha\rangle_A|\alpha\rangle_C &\to |\sqrt{2}\alpha\rangle_A|0\rangle_C, \\ |-\alpha\rangle_A|-\alpha\rangle_C &\to |-\sqrt{2}\alpha\rangle_A|0\rangle_C, \\ |\alpha\rangle_A|-\alpha\rangle_C &\to |0\rangle_A|-\sqrt{2}\alpha\rangle_C, \\ |-\alpha\rangle_A|\alpha\rangle_C &\to |0\rangle_A|\sqrt{2}\alpha\rangle_C. \end{aligned} \tag{2.35}$$

We can use a photon-number discriminating detector in channel A to detect the Bell state $|\alpha\rangle_A|\alpha\rangle_C - |-\alpha\rangle_A|-\alpha\rangle_C$. As a result, the effective transformation of the CV-DV converter is

$$c_0|cat_+\rangle + c_1|cat_-\rangle \to \frac{c_0|0\rangle + c_1|1\rangle}{N_+N_-\sqrt{2}}. \tag{2.36}$$

2.4 Alternative formalisms to describe the quantum states

A quantum state is usually represented by the density matrix formalism. However, due to the mathematical complexity of the teleportation and error correction protocols, it is

sometimes helpful to represent the states in other mathematical formalisms instead. In the following, I will discuss two alternative formalisms - the characteristic function and the Wigner function.

2.4.1 Characteristic function formalism

For an arbitrary state ρ, the usual characteristic function is defined as

$$\chi_\rho(\beta) = \mathrm{Tr}\left[\rho D(\beta)\right], \tag{2.37}$$

with complex number $\beta = x + jp$ and displacement operator $D(\beta) = e^{-|\beta|^2/2} e^{\beta \hat{a}^\dagger} e^{-\beta^* \hat{a}}$. For example, for a vacuum state $|0\rangle$, the characteristic function is given by

$$\chi_{vac}(\beta) = \exp\left[-|\beta|^2/2\right]. \tag{2.38}$$

For a SMSV state, let $S(\zeta)$ be the single-mode squeezing operator with $\zeta = se^{j\theta}$, where s is the single-mode squeezing parameter (which is different from the two-mode squeezing parameter r in Eq. (2.16)) and θ is the phase. The characteristic function of the SMSV state can be written as [13] [14]

$$\chi_{SMSV}(\beta) = \exp\left(-\frac{1}{2}|\beta\cosh s - e^{j\theta}\beta^* \sinh s|^2\right) \tag{2.39}$$

$$= \exp\left[-\frac{1}{2}(x^2 e^{-2s} + p^2 e^{2s})\right], \tag{2.40}$$

where the last equality has assumed $\theta = 0$. For a TMSV state given by Eq. (2.16), when there is no channel loss, the characteristic function is given by [14],

$$\chi_{TMSV}(\beta_A, \beta_B)$$

$$= \exp\left[-\frac{1}{2}\left(|\beta_A \cosh r + \beta_B^* e^{j\phi}\sinh r|^2 \ \ + |\beta_B \cosh r + \beta_A^* e^{j\phi}\sinh r|^2\right)\right] \tag{2.41}$$

$$= \exp\left\{-\frac{e^{2r}}{4}\left[(x_A - x_B)^2 + (p_A + p_B)^2\right] - \frac{e^{-2r}}{4}\left[(x_A + x_B)^2 + (p_A - p_B)^2\right]\right\}, \tag{2.42}$$

where the last equality has used $\phi = \pi$ for optimal teleportation fidelity.

For a tensor product of arbitrary density matrices, the characteristic function is a product of individual characteristic functions. For example, for an arbitrary separable state $\rho = \rho_1 \otimes \rho_2$, we have [15]

$$\chi_\rho(\beta_1, \beta_2) = \mathrm{Tr}\left[\rho D(\beta_1) D(\beta_2)\right] = \chi_{\rho_1}(\beta_1)\chi_{\rho_2}(\beta_2). \tag{2.43}$$

The characteristic function is also linear with respect to the density operator, as can be seen from the linearity of the trace function in Eq. (2.37).

The exact density matrix of the hybrid entangled state is given by Eq. (5.1), in which the cat state $|cat_\pm\rangle$ has the characteristic function [2]

$$\begin{aligned}&\chi_{cat_\pm}(\beta) = \\ &\frac{1}{N_\pm^2}\left\{2e^{-\frac{|\beta|^2}{2}}\cos\left[2\mathrm{Im}\left(\beta\alpha_0^*\right)\right]\right. \\ &\left.\pm e^{-\frac{1}{2}|\beta+2\alpha_0|^2} \pm e^{-\frac{1}{2}|\beta-2\alpha_0|^2}\right\}.\end{aligned} \tag{2.44}$$

An exact calculation can be found in appendix A.1.

2.4.2 Wigner function formalism

The Wigner function represents the probability distribution of a quantum state in the phase-space (position and momentum). Let $\alpha = x + jp$, the Wigner function is calculated from the density operator by the transformation

$$W(\alpha) = \frac{1}{\pi^2}\int d^2\beta Tr[\rho D(\beta)] e^{-(\beta\alpha^* - \beta^*\alpha)}, \tag{2.45}$$

which is clearly a Fourier transform of the characteristic function in Eq. (2.37). We can verify that $W(\alpha)$ is indeed a probability distribution by checking the condition $\int W(\alpha) d^2\alpha = \iint W(x,y)dxdy = 1$.

For a coherent state $|\gamma\rangle$, the Wigner function is given by the Gaussian distribution analogous to the classical optical field

$$W_{coh}(\alpha) = \frac{2}{\pi}\exp(-2|\alpha - \gamma|^2). \tag{2.46}$$

For a SMSV state $S^\dagger(\zeta)|0\rangle$ where $\zeta = se^{j\theta}$, we have [2]

$$\begin{aligned} W_{SMSV}(\alpha) &= \frac{1}{\pi^2}\int d^2\beta \langle 0|S^\dagger(\zeta)D(\beta)S(\zeta)|0\rangle] e^{-(\beta\alpha^* - \beta^*\alpha)} \\ &= \frac{\pi}{2}\exp\left(-2|\alpha\cosh s - \alpha^* e^{j\theta}\sinh s|^2\right), \end{aligned} \tag{2.47}$$

where we have applied the well-known relation

$$S^\dagger(\zeta)D(\beta)S(\zeta) = D(\beta') \text{ with } \beta' = \beta\cosh s - \beta^* e^{j\theta}\sinh s. \tag{2.48}$$

Thus, the Wigner function of an SMSV state is a squeezed Gaussian function. For a single-mode squeezed coherent state ($S(\zeta)|\beta\rangle$), the Wigner function is displaced from the center by β

$$W_{S(\zeta)|\beta\rangle}(\alpha) = W_{SMSV}(\alpha - \beta). \tag{2.49}$$

For a photon-number state, the Wigner function can be decomposed to the Laguerre polynomials

$$W_n(\alpha) = \frac{2}{\pi}(-1)^n e^{-2|\alpha|^2} L_n(4|\alpha|^2). \tag{2.50}$$

For the photon-number states, the Wigner function can be negative, which signifies the quantum nature of number states. For example, when $\alpha = 0$, we have $W_n(0) = \frac{2}{\pi}(-1)^n < 0$ for odd values of n.

For a TMSV state with two spatial modes A and B, let us define $\alpha_i = x_i + jp_i$, $\hat{x_i} = \frac{\hat{a_i}^\dagger + \hat{a_i}}{2}$, and $\hat{p_i} = j\frac{\hat{a_i}^\dagger - \hat{a_i}}{2}$, where $i \in \{A, B\}$, the Wigner function is given by [2]

$$\begin{aligned} W_{TMSV}(\alpha_A, \alpha_B) = \frac{4}{\pi^2}\exp(-2|\alpha_A\cosh r - \alpha_B^*\sinh r e^{j\phi}|^2 \\ - 2|-\alpha_A^*\sinh r e^{j\phi} + \alpha_B\cosh r|^2|), \end{aligned} \tag{2.51}$$

which is equivalent to [3]

$$\begin{aligned} W_{TMSV}(x_A, p_A, x_B, p_B) = \frac{4}{\pi^2}\exp\{ \\ - e^{-2r}\left[(x_A + x_B)^2 + (p_A - p_B)^2\right] \\ - e^{+2r}\left[(x_A - x_B)^2 + (p_A + p_B)^2\right]\}. \end{aligned} \tag{2.52}$$

We can see that when $r \to \infty$, this Wigner function approaches $C\delta(x_A - x_B)\delta(p_A + p_B)$, which represents a maximally entangled EPR state: the positions of the two modes are always equal, while the momentum is always opposite.

For a Schrödinger's cat state, we have

$$\rho_{cat_+} = N_+^{-2}\left(|\alpha_0\rangle\langle\alpha_0| + |-\alpha_0\rangle\langle-\alpha_0| + |\alpha_0\rangle\langle-\alpha_0| + |-\alpha_0\rangle\langle\alpha_0|\right) \tag{2.53}$$

The contribution from the terms $|\pm\alpha_0\rangle\langle\pm\alpha_0|$ are identical to the Wigner functions of coherent states in Eq. (2.46). For the cross terms $|\pm\alpha_0\rangle\langle\mp\alpha_0|$, the contribution is [2]

$$\begin{aligned}
&\frac{1}{\pi^2}\int d^2\beta|-\alpha_0\rangle D(\beta)\langle\alpha_0|e^{-(\beta\alpha^*-\beta^*\alpha)} \\
&= \frac{1}{\pi^2}\int d^2\beta|-\alpha_0\rangle e^{a^\dagger\beta}e^{-a\beta^*}\langle\alpha_0|e^{-(\beta\alpha^*-\beta^*\alpha)} \\
&= \frac{1}{\pi^2}\int d^2\beta e^{-\frac{1}{2}|\beta+2\alpha_0|^2-\beta\alpha^*+\beta^*\alpha} \\
&= \frac{2}{\pi}e^{-2|\alpha|^2}e^{2\alpha_0\alpha^*-2\alpha_0^*\alpha},
\end{aligned} \tag{2.54}$$

where the last step is integrated by apply the well-shown relation

$$\frac{1}{\pi}\int e^{-\gamma|\beta|^2}e^{\beta^*\alpha-\beta\alpha^*}d^2\beta = \frac{1}{\gamma}e^{-|\alpha|^2/\gamma}. \tag{2.55}$$

As a result, the Wigner function of the cat state is given by

$$\begin{aligned}
W_{cat_+}(\alpha) =& \frac{2}{\pi N_+^2}\{\exp\left(-2|\alpha-\alpha_0|^2\right) + \exp\left(-2|\alpha+\alpha_0|^2\right) \\
&+ 2e^{-2|\alpha|^2}\cos\left[\phi + 4Im\{\alpha_0^*\alpha\}\right]\}.
\end{aligned} \tag{2.56}$$

2.5 Basic teleportation protocols

Quantum teleportation is the technique to transfer an arbitrary unknown quantum state from one mode to another mode using a shared entanglement channel together with additional classical communication. The teleportation channel can be either DV or CV channel. DV teleportation is known for being probabilistic, however the teleportation outcome can retain high fidelity with the input state. In contrast, CV teleportation is deterministic but the outcome has lower quality [16]. In this section, we will introduce the mathematical basis of both DV and CV teleportation.

2.5.1 DV teleportation

In two-mode qubit systems, every state can be decomposed into the Bell states basis:

$$\begin{aligned}
|\Phi_0\rangle &= I \otimes \sigma_0 |\Phi_0\rangle = \frac{1}{\sqrt{2}} \left(|11\rangle_{AB} + |00\rangle_{AB} \right), \\
|\Phi_1\rangle &= I \otimes \sigma_1 |\Phi_0\rangle = \frac{1}{\sqrt{2}} \left(|10\rangle_{AB} + |01\rangle_{AB} \right), \\
|\Phi_2\rangle &= I \otimes \sigma_2 |\Phi_0\rangle = \frac{j}{\sqrt{2}} \left(|10\rangle_{AB} - |01\rangle_{AB} \right), \\
|\Phi_3\rangle &= I \otimes \sigma_3 |\Phi_0\rangle = \frac{1}{\sqrt{2}} \left(|00\rangle_{AB} - |11\rangle_{AB} \right),
\end{aligned} \tag{2.57}$$

where σ_i indicates the Pauli's matrices

$$\sigma_0 = I = \begin{pmatrix} 1 & 0 \\ 0 & 1 \end{pmatrix}, \ \sigma_1 = \begin{pmatrix} 0 & 1 \\ 1 & 0 \end{pmatrix}, \ \sigma_2 = \begin{pmatrix} 0 & -j \\ j & 0 \end{pmatrix}, \ \sigma_3 = \begin{pmatrix} 1 & 0 \\ 0 & -1 \end{pmatrix}. \tag{2.58}$$

In the DV teleportation protocol, the DV entangled Bell state $|\Phi_0\rangle_{AB}$ is used as the teleportation channel, where mode A is sent to Alice and mode B is sent to Bob. Alice then would like to teleport mode C from her side to Bob, where

$$|\Psi\rangle_C = c_1 |1\rangle_C + c_2 |0\rangle_C. \tag{2.59}$$

Next, Alice performs a Bell State Measurement (BSM) on modes A and C. Mathematically, a BSM is a projection of the two-mode state onto the Bell-state basis

$$\begin{aligned}
|\Psi\rangle_{ABC} &= \frac{1}{2} |\Phi_0\rangle_{AC} \otimes |\Psi\rangle_B + \frac{1}{2} |\Phi_1\rangle_{AC} \otimes \sigma_1 |\Psi\rangle_B + \frac{1}{2} |\Phi_2\rangle_{AC} \otimes \sigma_2 |\Psi\rangle_B + \frac{1}{2} |\Phi_3\rangle_{AC} \otimes \sigma_3 |\Psi\rangle_B \\
&= \sum_{i=0}^{3} \frac{1}{2} |\Phi_i\rangle_{AC} \otimes \sigma_i |\Psi\rangle_B.
\end{aligned} \tag{2.60}$$

After Alice performs BSM, she sends the measurement result, the integer i, to Bob. Bob then applies σ_i to his state. Since $\sigma_i^2 = 1$, Bob retrieves the original input state in mode C.

2.5.2 CV teleportation

The CV teleportation channel is the TMSV state $W_{TMSV}(x_A, p_A, x_B, p_B)$ in Eq. (2.52), where one mode is sent to Alice and the other mode is sent to Bob. The state to be

teleported has the Wigner function $W_C(x_C, p_C)$. The BSM between mode A and mode C is realized by a 50:50 beam splitter that output two mode u and v, followed by Alice's homodyne measurement on the maximally entangled basis of x_u and p_v [3]. The beam splitter transformation is given by

$$\begin{aligned} x_u &= \frac{x_C - x_A}{\sqrt{2}}, \quad p_u = \frac{p_C - p_A}{\sqrt{2}}, \\ x_v &= \frac{x_C + x_A}{\sqrt{2}}, \quad p_v = \frac{p_C + p_A}{\sqrt{2}}, \end{aligned} \tag{2.61}$$

thus

$$\begin{aligned} x_C &= \frac{x_u + x_v}{\sqrt{2}}, \quad p_C = \frac{p_u + p_v}{\sqrt{2}}, \\ x_A &= \frac{x_v - x_u}{\sqrt{2}}, \quad p_A = \frac{p_v - p_u}{\sqrt{2}}. \end{aligned} \tag{2.62}$$

The three-mode state $W(\alpha_u, \alpha_v, \alpha_B)$ can be obtained from the original state $W(\alpha_C, \alpha_A, \alpha_B)$ by a change-of-variable integration

$$\begin{aligned} W(\alpha_u, \alpha_v, \alpha_B) = \int & dx_C dp_C W_C(x_C, p_C) \\ & \times W_{TMSV}(\frac{x_v - x_u}{\sqrt{2}}, \frac{p_v - p_u}{\sqrt{2}}, x_B, p_B) \\ & \times \delta\left[\frac{x_u + x_v}{\sqrt{2}} - x_C\right] \delta\left[\frac{p_u + p_v}{\sqrt{2}} - p_C\right]. \end{aligned} \tag{2.63}$$

Then, the homodyne detection of x_u and p_v is performed mathematically by tracing out the modes x_v and p_u

$$\begin{aligned} \int dx_v dp_u W(\alpha_u, \alpha_v, \alpha_B) = 2 \int & dx dp W_C(x, p) \\ & \times W_{TMSV}(x - \sqrt{x_u}, \sqrt{p_v} - p, x_b, p_B). \end{aligned} \tag{2.64}$$

Finally, Alice sends her results of x_u and p_v to Bob, so that Bob can displace his state as

$$x'_B = x_B - \sqrt{2} x_u, \quad p'_B = p_B - \sqrt{2} p_v. \tag{2.65}$$

The final ensemble of states is given by integrating the Wigner function over x_u and p_v, giving

$$\begin{aligned} W_B(x'_B, p'_B) &= \frac{1}{\pi e^{-2r}} \int d^2\alpha W_C(x, p) \exp\left(-\frac{|\alpha'_B - \alpha|^2}{e^{-2r}}\right) \\ &\equiv W_C * G_{\sigma_{tel}}, \end{aligned} \tag{2.66}$$

where $G_{\sigma_{tel}}$ is a Gaussian state with variance σ_{tel}

$$G_{\sigma_{tel}}(x,p) \equiv \frac{1}{\pi\sigma} \exp\left(-\frac{|x^2+p^2|}{\sigma_{tel}}\right), \tag{2.67}$$

with

$$\sigma_{tel} = e^{-2r}. \tag{2.68}$$

When the squeezing r tends to infinity, the teleported state becomes identical to the input state.

2.6 Measures of entanglement

In order to assess the teleportation and entanglement swapping protocols, we need a method to compare the entangled state before and after the protocols. To quantify the level of entanglement in a bipartite quantum state (ρ_{AB}), different mathematical measures (E) have been proposed, which must satisfy two important conditions: E should become zero for separable states and E should not increase under local operations and classical communication (LOCC) [17–19]. For a pure state, we can simply use the measure of entanglement entropy as a measure of entanglement

$$E_E(\rho_{AB}) = -Tr(\rho_{AB} \ln \rho_{AB}) = -\sum_i \lambda_i \ln \lambda_i, \tag{2.69}$$

where $\{\lambda_i\}$ are the eigenvalues of ρ_{AB}.

For a mixed state with finite dimension, we can use the measures of distillable entanglement or the measure of entanglement cost, which quantify operationally how much entanglement resource is needed to produce ρ_{AB}. However, these measures are very difficult to calculate, so another measure called the "entanglement of formation" is proposed. Let a pure-state decomposition of ρ_{AB} be

$$\rho_{AB} = \sum_i p_i |\psi_i\rangle\langle\psi_i|, \tag{2.70}$$

the entanglement of formation is defined as the minimal averaged entanglement over all possible pure-state decompositions [17]

$$E_F(\rho_{AB}) = inf\{\sum_i p_i E\left(|\psi_i\rangle\langle\psi_i|\right) : \rho_i = p_i|\psi_i\rangle\langle\psi_i|\}, \tag{2.71}$$

where the entropy of entanglement E for a pure state $|\psi\rangle$ is defined as

$$E\left(|\psi\rangle\langle\psi|\right) = S(Tr_A\left[|\psi_i\rangle\langle\psi_i|\right]) = S(Tr_B\left[|\psi_i\rangle\langle\psi_i|\right]), \tag{2.72}$$

with S denoting the von-Neumann entropy

$$S(\rho) = -Tr\left[\rho\log_2\rho\right], \tag{2.73}$$

and $Tr_i(\rho_{AB})$ with $i \in \{A, B\}$ denoting the partial trace over the subspace i.

The regularized (or asymptotic) version of the entanglement of formation was proven to be equal to the entanglement cost (E_C) [17]

$$E_F^{\infty}(\rho_{AB}) = \lim_{n\to\infty}\frac{E_F(\rho_{AB}^{\otimes n})}{n} = E_C(\rho_{AB}). \tag{2.74}$$

For a CV state, where the dimension is infinite, the entanglement of formation becomes not well-defined, and can only be calculated analytically for certain types of Gaussian states. For a general two-mode Gaussian state, the lower bound for entanglement of formation can be calculated numerically. However, for non-Gaussian states, there is currently no known method to calculate the entanglement of formation [19].

Even though the measures introduced above are considered more comprehensive, they are all very hard to compute, especially for the non-Gaussian states that I am going to study in the following chapters. Thus, in this thesis, I will use the measures of logarithmic negativity and fidelity. The measure of logarithmic negativity is relatively easy to calculate, even though this measure does not have strong asymptotic continuity and strong super additivity. The logarithmic negativity is widely used for all types of entangled state, especially for mixed states with infinite dimensions like the lossy teleported hybrid entangled state. To relatively compare the teleported state with the original entangled state, I will also use the measure of fidelity between the two states. The mathematical details of the logarithmic negativity and the fidelity are given below.

2.6.1 The logarithmic negativity

The negativity of an arbitrary state ρ is defined by the sum of the negative eigenvalues [20]

$$E_N(\rho) = \frac{1}{2}\sum_i \left(|\lambda_i| - \lambda_i\right), \tag{2.75}$$

where λ_i are the eigenvalues of the partial transpose of the entangled state ρ. The logarithmic negativity is related to the negativity by [20]

$$E_{LN}(\rho) = \log_2[1 + 2E_N(\rho)]. \tag{2.76}$$

The logarithmic negativity E_{LN} of a two-mode state ρ is a number between 0 and 1 that measures the level of entanglement in the state. When $E_{LN} > 0$, ρ is an entangled state. When $E_{LN} = 1$, ρ should be a pure entangled state [4]. For a two-mode state ρ_{AB}, the logarithmic negativity can also be calculated by using the relation

$$E_{LN}(\rho_{AB}) \equiv \log_2 ||\rho_{AB}^{T_A}||, \tag{2.77}$$

where

$$||\rho_{AB}|| = \mathrm{Tr}\left[\left(\rho_{AB}^{\dagger}\rho_{AB}\right)^{1/2}\right], \tag{2.78}$$

and T_A denotes the partial transpose on mode A. For a bi-partie state ρ_{AB}, the partial transpose over the subspace A is defined as T_A, such that

$$\rho_{AB}^{T_A} = \sum_j \left(\rho_{Aj} \otimes \rho_{Bj}\right)^{T_A} = \sum_j \left(\rho_{Aj}^{T_A} \otimes \rho_{Bj}\right). \tag{2.79}$$

2.6.2 The fidelity

The fidelity is a measure of similarity between two quantum mechanical states. For two general states ρ and ρ', the fidelity is given by

$$F(\rho, \rho') = \left[Tr\left(\sqrt{\sqrt{\rho'}\rho\sqrt{\rho'}}\right)\right]^2. \tag{2.80}$$

When the states are pure, $\rho = |\psi\rangle\langle\psi|$ and $\rho' = |\psi'\rangle\langle\psi'|$, the fidelity can be simplified to

$$F(|\psi\rangle, |\psi'\rangle) = |\langle\psi'|\psi\rangle|^2. \tag{2.81}$$

In the characteristic function formalism, the fidelity can be calculated by

$$F\left(\chi(\beta), \chi^{'}(\beta)\right) = \frac{1}{\pi^2}\int d\beta^2 \chi(\beta)\chi^{'}(-\beta). \tag{2.82}$$

2.7 Device-Independent Quantum Key Distribution (DIQKD) protocol for the photon-number basis

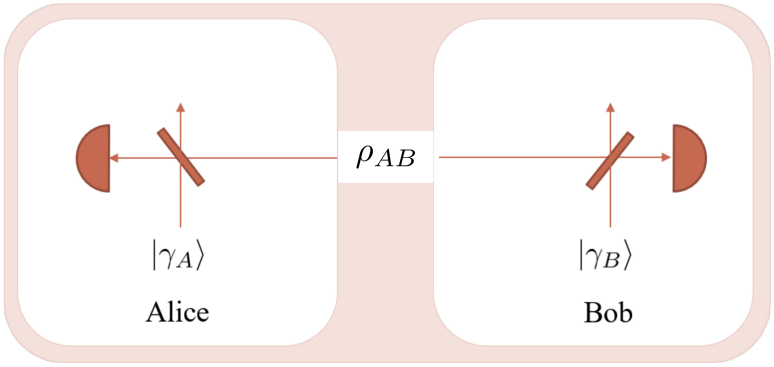

Figure 2.5: The device-independent QKD protocol for entanglement in the photon-number basis.

In this section, we apply a DV entangled state to the DIQKD protocol in Fig. 2.5

$$|\psi_{max}\rangle_{AB} = \frac{|0\rangle_A|1\rangle_B - |1\rangle_A|0\rangle_B}{\sqrt{2}}, \tag{2.83}$$

where A and B denote two spatial modes of the entanglement. The protocol exploits the CH nonlocality testing for DV entanglement in the photon-number basis. Each spatial mode of the DV entanglement is mixed with a coherent state $|\gamma_i\rangle$, with $i \in \{A, B\}$, via a beam splitter with transmissivity T_i, then detected by a photon-counter. When $T_i \to \infty$ and $\gamma_i \to \infty$, the effect of the beam-splitter is described by the displacement operator $\hat{D}(\alpha_i)$, where $\hat{D}$ is the coherent displacement operator and $\alpha_i = \sqrt{1 - T_i}\gamma_i$. We assume that the detector is threshold-gated and can only distinguish between vacuum and

non-vacuum. Mathematically, the measurement is described by a pair of two orthogonal projection operators

$$\hat{Q}(\alpha_i) = \hat{D}(\alpha_i)|0\rangle_i\langle 0|\hat{D}^\dagger(\alpha_i), \tag{2.84}$$

$$\hat{P}(\alpha_i) = \hat{D}(\alpha_i)\sum_{n=1}^{\infty}|n\rangle_i\langle n|\hat{D}^\dagger(\alpha_i), \tag{2.85}$$

such that

$$\hat{Q}(\alpha_i) + \hat{P}(\alpha_i) = \mathbb{1}. \tag{2.86}$$

In the QKD protocol, mode A is sent to Alice while mode B is sent to Bob. Alice and Bob randomly choose between two possible measurement settings $\alpha_A \in \{0, s\}$ and $\alpha_B \in \{0, -s\}$. The secret keys are generated by assigning the logical value 0 (or 1) to the event that only Alice's (or Bob's) detector clicks. The probability that each detector does not click is given by

$$\begin{aligned} Q_A(\alpha_A) &= \langle \hat{Q}_A(\alpha_A) \otimes \mathbb{1}_B\rangle, \\ Q_B(\alpha_B) &= \langle \mathbb{1}_A \otimes \hat{Q}_B(\alpha_B)\rangle. \end{aligned} \tag{2.87}$$

The probability that both detectors do not click is given by

$$Q_{AB}(\alpha_A, \alpha_B) = \langle \hat{Q}_A(\alpha_A) \otimes \hat{Q}_B(\alpha_B)\rangle. \tag{2.88}$$

Given an arbitrary entangled state, the CH inequality is given by [21]

$$\begin{aligned} \langle CH\rangle =& Q_{AB}(0,0) + Q_{AB}(s,0) + Q_{AB}(0,-s) \\ &- Q_{AB}(s,-s) - Q_A(0) - Q_B(0). \end{aligned} \tag{2.89}$$

Let $J = |\alpha_i|^2$, we have $J \in \{0, |s|^2\}$. For a general DV entangled state of the form

$$\begin{aligned} \rho = & a_0|0\rangle_A\langle 0| \otimes |0\rangle_B\langle 0| \\ & + a_1|0\rangle_A\langle 0| \otimes |1\rangle_B\langle 1| + c_{-1}|1\rangle_A\langle 1| \otimes |0\rangle_B\langle 0| \\ & - b_0|1\rangle_A\langle 0| \otimes |0\rangle_B\langle 1| - b_0|0\rangle_A\langle 1| \otimes |1\rangle_B\langle 0|, \end{aligned} \tag{2.90}$$

we derive the clicking probabilities

$$\begin{aligned} Q_{AB}(0,0) &= a_0, \\ Q_{AB}(s,0) &= e^{-J}(a_0 + c_{-1}J), \\ Q_{AB}(0,-s) &= e^{-J}(a_0 + Ja_1), \\ Q_{AB}(s,-s) &= e^{-2J}(a_0 + Ja_1 + Jc_{-1} + 2Jb_0), \\ Q_A(0) &= a_0 + a_1, \\ Q_B(0) &= a_0 + c_{-1}. \end{aligned} \tag{2.91}$$

For a vacuum state, we have $a_0 = 1$ while all other coefficients are 0, the CH value is

$$\langle CH_{vac} \rangle = -e^{-2J} + 2e^{-J} - 1. \tag{2.92}$$

For the maximally DV-entangled state $|\psi_{max}\rangle$ (Eq. (2.83)), we have $a_0 = 0$ while other coefficients are $1/2$, the CH value is given by

$$\langle CH_{max} \rangle = -2Je^{-2J} + Je^{-J} - 1. \tag{2.93}$$

The security of the DIQKD protocol is analyzed against the individual attack where the eavesdropper is only constrained by no-signaling theory [21, 22]. The bound on the key rate is calculated by [21]

$$K \geq 1 - 2(\langle CH \rangle + 1.5) - h(p_e), \tag{2.94}$$

where p_e is the estimated bit error rate.

Chapter 3

Hybrid Entanglement Swapping for Satellite-based Quantum Communications

In this chapter, I study for the first time the effect of attenuation on the CV teleportation channel created between two ground stations via a LEO satellite. Firstly, I will derive the general mathematical model for the teleportation of an arbitrary state through a lossy CV teleportation channel. Next, I will study the special case where the mode to be teleported is part of a DV entangled state in the photon number basis. I will present conditions where the teleported DV states can retain a stronger level of entanglement as compared to the direct distribution from the satellite. As an application, I will present the key rate obtained when applying the teleported state to a QKD protocol.

3.1 Introduction

Quantum communication via LEO satellites offers the possibility of an information-theoretically secure global network [23]. The security of this network is provided by QKD, in which

secret keys are encoded and distributed between two parties using quantum states of light. Beyond QKD, other quantum-information protocols will be relayed over this new global network, with teleportation being one of the most important [24].

Terrestrial quantum communication has been limited to a few hundred kilometers because of the exponential loss in optical fibers. What is more, according to the no-cloning theorem, the quantum signal cannot be noiselessly amplified [25–27]. A QKD experiment in 2007 achieved the communication range of 200km, which corresponds to 40dB of loss [28], while a more recent study in 2015 used ultra-low-loss fiber to achieve a range of 300km with 50dB of total loss [29]. In contrast, the satellite-Earth channel is only affected by a thin layer of atmospheric turbulence in a zone roughly between the ground level and 12 km high. For a satellite in LEO (400 to 600km from Earth), the average channel attenuation is only around 5-10dB for a down-link and 20-30dB for an up-link transmission [30]. Thus, the satellite works as a relay that can potentially extend quantum communication to a global scale.

In many traditional quantum-information protocols, quantum entanglement is carried by either DV or CV. In DV the quantum information is usually encoded into the polarization or the number of photons. In CV the quantum information is encoded in the quadratures of the optical field. Compared to DV protocols, CV protocols use homodyne (or heterodyne) detectors which are faster and more efficient. As a result, it is potentially easier to achieve higher performance levels for certain CV quantum-information protocols.

In this chapter, I will investigate hybrid teleportation (Fig. 4.1), where the CV entanglement is used as a teleportation channel ($A'-B'$), while the entangled state to be teleported ($C-D$) can be encoded in either DV or CV. Such a hybrid teleportation protocol has the potential to leverage the versatility of the satellite. The design and implementation of a quantum satellite-payload often involves a great engineering effort. Once a satellite is deployed, there is little freedom in altering the payload and its functionality. However, if we place a source of CV entanglement on the satellite and beam the states down to the ground, we will have a CV teleportation channel that can teleport both DV and CV entangled states. This, in turn, opens up the possibility of inter-connecting quantum-enabled

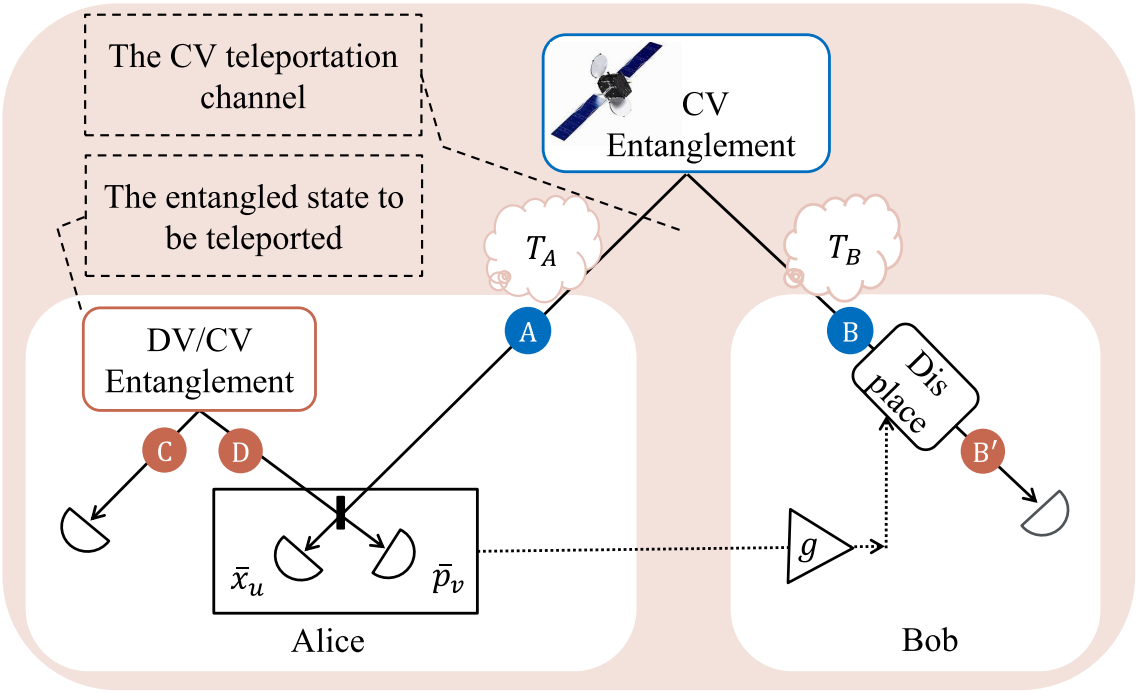

Figure 3.1: In the hybrid scheme, the attenuated CV entanglement $A' - B'$ is used as a teleportation channel. The entangled state to be teleported, $C - D$, can be encoded in either DV or CV. (Taken from [31].)

devices that may be processing quantum information internally on quite different hardware architectures - conditioned only on the premise that these devices have external laser links to satellites. In this chapter, I explore this possibility, focussing on the teleportation of DV states over a CV teleportation channel (CV teleportation via a CV teleportation channel has been well studied previously [32, 33], however, it usually leads to low-quality outputs unless the channel is highly squeezed. It will be shown later in chapter 5 that teleporting the DV mode yields better results for certain input states).

Previous studies of entanglement swapping only focused on the context of local measurements without transmission loss [3, 4, 16, 32–35]. In this chapter, I extend such previous studies to the more difficult setting of photonic loss. My main contributions and findings in this paper are:

- I derive a mathematical model for hybrid teleportation over a CV teleportation channel, taking into account transmission losses, and propose a strategy for gain-tuning in order to optimize the teleportation outcome.

- I then perform a comparison between teleported and directly distributed DV entanglement (in the photon-number basis), showing that such teleported DV entanglement can retain a higher quality, especially for an optical link loss of about 5 to 10dB.

- I calculate the key rates for a robust form of the device-independent QKD protocol, showing that key rate reduces to zero at around 2dB of loss. As a result, the teleported entanglement does not show a higher key rate relative to the directly-distributed entanglement.

The structure of the remainder of this chapter is as follows. Section 3.2 studies how channel transmissivities affect the quality of the CV teleportation channel. Section 3.3 studies hybrid entanglement swapping using an attenuated CV teleportation channel. Section 3.4 studies the effect of channel attenuation on a directly-distributed DV entangled state. Section 3.6 shows my simulations, while section 3.7 summarizes my findings.

3.2 Attenuation on a CV teleportation channel

This section outlines how channel attenuation[(1)] affects the quality of the CV teleportation channel, where the CV channel is given by the TMSV state in Eqs. (2.15) and (2.52). Let A and B be the two spatial mode of the TMSV state. For each spatial mode let $i \in \{A, B\}$, the channel attenuation can be modeled by a beam-splitter with transmissivity T_i. The beam-splitter transformation can then be written as

$$\hat{a}_i{}^\dagger \to \sqrt{T_i}\hat{a}_i{}^\dagger + \sqrt{1-T_i}\hat{a}_{i_v}^\dagger, \tag{3.1}$$

where the subscript v denotes the auxiliary vacuum mode. Let $G_\sigma(x,p)$ denote a Gaussian function with variance σ as defined in Eq. (2.67). In the Wigner-function formalism, each

[(1)]Note, that in the downlink channel from the satellite some fading will exist. However, this can be mitigated by large receiving telescopes and/or advanced adaptive optical tracking techniques, and in this exploratory work I will assume the channel loss is fixed (no fading).

beam-splitter transformation is equivalent to a convolution between the input and a Gaussian function $G_{\sigma_{T_i}}$ with variance $\sigma_{T_i} = \frac{2T_i}{1-T_i}$, followed by a rescaling of $1/\sqrt{T_i}$ in phase space [4]. For a TMSV state, when the modes are sent through two channels with different transmissivities T_A and T_B (see Fig. 4.1), we can perform the beam-splitter transformation sequentially on each mode: $W_{TMSV}(x_A, p_A, x_B, p_B) \rightarrow W^{(T_A,1)}_{TMSV}(x'_A, p'_A, x_B, p_B) \rightarrow W^{(T_A,T_B)}_{TMSV}(x'_A, p'_A, x'_B, p'_B)$. Let $*$ denote the convolution operator, the first transformation (where x_B and p_B are taken as constants) is given by

$$\begin{aligned} W^{(T_A,1)}_{TMSV}(x'_A, p'_A, x_B, p_B) &= \frac{1}{T_A}\left[W_{TMSV} * G_{\sigma_{T_A}}\right]\left(\frac{x'_A, p'_A}{\sqrt{T_A}}\right) \\ &= \frac{1}{T_A}\iint dx_A\, dy_A W_{TMSV}(x_A, p_A, x_B, p_B) \times \frac{1}{\pi\sigma_{T_A}} \times \\ &\exp\left\{-\frac{1}{\sigma_{T_A}}\left[\left(\frac{x'_A}{\sqrt{T_A}} - x_A\right)^2 + \left(\frac{p'_A}{\sqrt{T_A}} - p_A\right)^2\right]\right\}, \end{aligned} \tag{3.2}$$

with the second transformation being similar, giving

$$\begin{aligned} W^{(T_A,T_B)}_{TMSV}(x'_A, p'_A, x'_B, p'_B) &= \frac{4}{\pi^2\tau}\exp\{ \\ &- \frac{e^{-2r}}{\tau}\left[\left(x'_A\sqrt{T_B} + x'_B\sqrt{T_A}\right)^2 + \left(p'_A\sqrt{T_B} - p'_B\sqrt{T_A}\right)^2\right] \\ &- \frac{e^{+2r}}{\tau}\left[\left(x'_A\sqrt{T_B} - x'_B\sqrt{T_A}\right)^2 + \left(p'_A\sqrt{T_B} + p'_B\sqrt{T_A}\right)^2\right] \\ &- \frac{2}{\tau}\left[(1-T_B)\left(x'^2_A + p'^2_A\right) + (1-T_A)\left(x'^2_B + p'^2_B\right)\right]\}, \end{aligned} \tag{3.3}$$

where τ is given by

$$\tau = 1 + [\cosh(2r) - 1]\,(T_A + T_B - 2T_AT_B). \tag{3.4}$$

3.3 Teleportation by an attenuated CV teleportation channel

3.3.1 Teleportation of an arbitrary mode with gain tuning

The CV teleportation by a perfect TMSV channel was described in section 2.5.2. To describe an attenuated CV teleportation channel ($A' - B'$ in Fig. 4.1), we use the CV

state in Eq. (3.3). The channel can teleport any modes, be it DV or CV, from Alice to Bob. Let $\alpha_i = x_i + jp_i$ where i indicates the mode, the arbitrary input mode to be teleported (e.g. mode D) can be denoted as $W_{in}(\alpha_{in})$. The teleportation process starts with a BSM. [3, 32, 33]. Experimentally, this is done by combining the input mode with mode A through a 50:50 beam splitter, which results in two new modes u and v such that

$$\begin{aligned} \hat{x}_u &= \frac{\hat{x}_{in} - \hat{x}'_A}{\sqrt{2}}, \quad \hat{p}_u = \frac{\hat{p}_{in} - \hat{p}'_A}{\sqrt{2}}, \\ \hat{x}_v &= \frac{\hat{x}_{in} + \hat{x}'_A}{\sqrt{2}}, \quad \hat{p}_v = \frac{\hat{p}_{in} + \hat{p}'_A}{\sqrt{2}}. \end{aligned} \tag{3.5}$$

We have $\alpha'_A = (\alpha_v - \alpha_u)/\sqrt{2}$. After the beam splitter, the three-mode Wigner function is transformed to [3]

$$\begin{aligned} W(\alpha_u, \alpha_v, \alpha'_B) &= \iint dx_{in} dp_{in} W_{in}(\alpha_{in}) \\ &\times W_{TMSV}^{(T_A,T_B)} \left(\frac{\alpha_v - \alpha_u}{\sqrt{2}}, \alpha'_B \right) \\ &\times \delta \left(\frac{x_u + x_v}{\sqrt{2}} - x_{in} \right) \delta \left(\frac{p_u + p_v}{\sqrt{2}} - p_{in} \right), \end{aligned} \tag{3.6}$$

and Alice performs homodyne detections for x_u and p_v. Alice's measurements of x_u and p_v are described by integration over x_v and p_u, respectively. After a change of variable: $x_v \to x = (x_u + x_v)/\sqrt{2}$ and $p_u \to p = (p_u + p_v)/\sqrt{2}$, we have

$$\begin{aligned} \iint dx_v dp_u W(\alpha_u, \alpha_v, \alpha'_B) &= 2 \iint dx dp W_{in}(x + jp) \\ &\times W_{TMSV}^{(T_A,T_B)} \left[x - \sqrt{2}x_u + j \left(\sqrt{2}p_v - p \right), \alpha'_B \right]. \end{aligned} \tag{3.7}$$

After the BSM, Alice sends the result of (x_u, p_v) to Bob who displaces his mode B from α'_B to α''_B such that $x'_B = (x''_B - g\sqrt{2}x_u)$ and $p'_B = (p''_B - g\sqrt{2}p_v)$. The parameter g denotes the gain during the transformation, which can be experimentally tuned to optimize the output quality (see section 3.6). When Alice teleports an ensemble of input modes, the output should be averaged over all possible values of x_u and p_v. The output of the whole

teleportation process is

$$W_{out}(\alpha''_B) = 2\iint dxdpW_{in}(x+jp) \times \iint dx_u dp_v W^{(T_A,T_B)}_{TMSV}[x-\sqrt{2}x_u + j\left(\sqrt{2}p_v - p\right), x''_B - g\sqrt{2}x_u + j\left(p''_B - g\sqrt{2}p_v\right)]. \quad (3.8)$$

After performing the integration over x_u and p_v, we find that the output function is a Gaussian convolution of the input, followed by a rescaling of $\alpha''_B \to \alpha''_B/g$ in phase space

$$\begin{aligned} W_{out}(\alpha''_B) &= \frac{1}{g^2}\left[W_{in} * G_{\sigma_{tel}}\right]\left(\frac{\alpha''_B}{g}\right) \\ &= \frac{1}{g^2}\iint dxdpW_{in}(\alpha)G_{\sigma_{tel}}\left(\frac{\alpha''_B}{g} - \alpha\right). \end{aligned} \quad (3.9)$$

Here $G_{\sigma_{tel}}$ is the Gaussian function defined in Eq. (2.67) with variance σ_{tel} given by

$$\begin{aligned} \sigma_{tel} = \frac{1}{4g^2}\ [\ & e^{+2r}(g\sqrt{T_A} - \sqrt{T_B})^2 \\ & + e^{-2r}(g\sqrt{T_A} + \sqrt{T_B})^2 \\ & + 2g^2\ (1-T_A) + 2(1-T_B)\ ]. \end{aligned} \quad (3.10)$$

Eq. (3.10) agrees with previous findings for simpler scenarios where there is no channel attenuation [34], or where the gain is set to unity [3]. When there is no channel attenuation, $T_A = T_B = 1$, we have $\sigma_{tel} = \left[e^{2r}(1-g)^2 + e^{-2r}(1+g)^2\right]/(4g^2)$. When the gain is set to unity, $g = 1$, the variance is further simplified to $\sigma_{tel} = e^{-2r}$ as in Eq. (2.68).

3.3.2 Teleportation of a DV entangled state

In the previous subsection, I have discussed how to teleport an arbitrary input mode by an attenuated CV teleportation channel. In this section, I discuss the special case of hybrid DV-CV entanglement swapping (see Fig. 4.1). In this scenario, the input mode D is part of the DV entangled pair $C-D$. The teleportation is carried out by the CV teleportation channel $A-B$, which teleports the mode D to B''. As a result, the teleportation output $\rho_{CB''}$ is a DV entangled state. In the Wigner formalism, the transformation of mode D is described by Eqs. (3.9) to (3.10). Since we are dealing here with a DV input, we will

convert the above equations to the density matrix representation and provide a measure to qualify its level of entanglement.

In this chapter, I assume that the state $C-D$ is entangled in the photon-number basis. Experimentally, ρ_{CD} is produced by passing a single photon through a balanced beam splitter, giving

$$|\psi\rangle_{CD} = (|01\rangle - |10\rangle)/\sqrt{2}, \quad \rho_{CD} = |\psi\rangle_{CD}\langle\psi| \ . \tag{3.11}$$

In the Wigner-function representation, the teleportation will transform the subspace of mode D according to [4]:

$$W_{in}^{|m\rangle_D\langle n|}(\alpha_D) \to \frac{1}{g^2}\left[W_{in}^{|m\rangle_D\langle n|}(\alpha_D) * G_{\sigma_{tel}}\right]\left(\frac{\alpha''_B}{g}\right), \tag{3.12}$$

where $m, n \in \{0, 1\}$ and $G_{\sigma_{tel}}$ is the Gaussian function of Eq. (2.67), with variance σ_{tel} defined in Eq. (3.10). In the density-matrix representation, the output state can be decomposed to [4]

$$\begin{aligned}
\rho_{CB''} &= \sum_{k=-1}^{\infty} \rho_k, \text{ where} \\
\rho_k &= a_k|0\rangle_C\langle 0| \otimes |k\rangle_{B''}\langle k| \\
&\quad - b_k|1\rangle_C\langle 0| \otimes |k\rangle_{B''}\langle k+1| - b_k|0\rangle_C\langle 1| \otimes |k+1\rangle_{B''}\langle k| \\
&\quad + c_k|1\rangle_C\langle 1| \otimes |k+1\rangle_{B''}\langle k+1|, \text{ where}
\end{aligned} \tag{3.13}$$

$$\begin{aligned}
a_k &= \frac{1}{2}T_{11\to kk}\,(k \geq 0), \text{or } 0\ (k=-1), \\
b_k &= \frac{1}{2}T_{10\to k+1\,k}\,(k \geq 0), \text{or } 0\ (k=-1), \\
c_k &= \frac{1}{2}T_{00\to k+1\,k+1}\,(k \geq -1), \text{ and where}
\end{aligned} \tag{3.14}$$

$$\begin{aligned}
T_{00\to kk} &= \frac{2(\gamma-1)^k}{(\gamma+1)^{k+1}}, \\
T_{11\to kk} &= \frac{2(\gamma-1)^{k-1}}{(\gamma+1)^{k+2}}\left[(\gamma-2g^2+1)(\gamma-1)+4kg^2\right] \\
T_{10\to k+1\,k} &= \frac{4g\sqrt{k+1}(\gamma-1)^k}{(\gamma+1)^{k+2}},
\end{aligned} \tag{3.15}$$

with

$$\gamma \equiv g^2(2\sigma_{tel} + 1). \tag{3.16}$$

In the limit where $T_A = T_B = 1$, $r \to \infty$ and $g = 1$ (which leads to $\gamma = 1$), we have $a_1 = b_0 = c_{-1} = 1/2$ while all other coefficients tend to 0. The output state $\rho_{CB''}$ becomes the same as ρ_{CD} in Eq. (3.11), which is a maximally entangled state.

In order to assess the entanglement in $\rho_{CB''}$, we use the logarithmic negativity described in section 2.6.1. For the teleported state (Eq. 3.13), the logarithmic negativity is [4]

$$E_{LN}(\rho_{CB''}) = \log_2 \left[1 + \sum_{k=-1}^{\infty} \left(|\lambda_k^-| - \lambda_k^- \right) \right], \tag{3.17}$$

where $\lambda_k^{\pm}$ are the eigenvalues of ρ_k

$$\lambda_k^{\pm} = \frac{1}{2} \left[a_k + c_k \pm \sqrt{(a_k - c_k)^2 + 4b_k^2} \right]. \tag{3.18}$$

3.4 Directly distributed DV entangled state

In the last section, I have discussed how to teleport a DV-entangled state by a CV teleportation channel. In this section, I study the case when the DV entangled state $(A - B)$ is directly distributed from the satellite. I also assume that the state is entangled in the photon-number basis[(2)], and, for simplicity, that the two down-link channels have equal transmissivity of $T_A = T_B = T$. Let us denote the two modes of the state to be directly distributed as A and B with corresponding creation operators $\hat{a_A}^\dagger$ and $\hat{a_B}^\dagger$. The state can be written as

$$\begin{aligned} |\psi\rangle_{AB} &= \frac{1}{\sqrt{2}} \left(|01\rangle_{AB} - |10\rangle_{AB} \right) |00\rangle_{v_A v_B} \\ &= \frac{1}{\sqrt{2}} (\hat{a_A}^\dagger - \hat{a_B}^\dagger) |00\rangle_{AB} |00\rangle_{v_A v_B}, \end{aligned} \tag{3.19}$$

[(2)]Please note, conversion from DV-polarization coding to DV-photon-number encoding is possible, and it is part of my future work to thoroughly study hybrid entanglement swapping in the context of attenuated CV teleportation when the states to be teleported are encoded in polarization.

where v_A and v_B denotes the auxiliary vacuum modes of mode A and B, respectively. For each mode of the entanglement, the channel attenuation can be modeled by a beam-splitter with transmissivity T. In the Heisenberg picture, the beam-splitter transformation can be written as in Eq. (3.1), which transforms the state to

$$\begin{aligned}|\psi'\rangle_{AB} = \sqrt{\frac{1}{2}}(&\sqrt{T}\hat{a_A}^\dagger + \sqrt{1-T}\hat{a_A}_v^\dagger \\ &- \sqrt{T}\,\hat{a_B}^\dagger - \sqrt{1-T}\,\hat{a_B}_v^\dagger)|00\rangle_{AB}|00\rangle_{v_Av_B} \\ = &\sqrt{\frac{T}{2}}\left(|01\rangle_{AB} - |10\rangle_{AB}\right)|00\rangle_{v_Av_B} \\ &+ \sqrt{\frac{1-T}{2}}|00\rangle_{AB}\left(|01\rangle_{v_Av_B} - |10\rangle_{v_Av_B}\right). \end{aligned} \tag{3.20}$$

By tracing out the auxiliary vacuum modes, we obtain

$$\rho'_{AB} = T\rho_{AB} + (1-T)|00\rangle_{AB}\langle 00|, \tag{3.21}$$

where ρ_{AB} is the corresponding density matrix for the maximally entangled state defined in Eq. (3.19). The logarithmic negativity of this state is calculated by Eq. (2.77).

3.5 Device-independent QKD protocol

To calculate the lower bound of the secure key rates, I use a device-independent QKD (DI-QKD) protocol which tests for non-locality using the CH inequality. The protocol is designed for DV entanglement in the photon-number basis. The security is analyzed against the individual attack assuming that the eavesdropper is only constrained by the no-signaling theory [21, 22]. The mathematical model for a general entangled state was introduced in section 2.7. For the state directly distributed from the satellite (ρ'_{AB} in Eq. (3.21)), we have

$$\langle CH_{direct}\rangle = T\langle CH_{direct}\rangle + (1-T)\langle CH_{vac}\rangle, \tag{3.22}$$

with $\langle CH_{direct}\rangle$ and $\langle CH_{vac}\rangle$ given in Eqs. (2.92) and (2.93). When the state is teleported ($\rho_{CB'}$ in Eq. (3.13)) with a_k, b_k and c_k defined in Eq. (3.14), we have

$$
\begin{aligned}
Q_{AB}(0,0) &= a_0, \\
Q_{AB}(s,0) &= e^{-J}(a_0 + c_{-1}J), \\
Q_{AB}(0,-s) &= e^{-J}\sum_{k=0}^{\infty} a_k \frac{J^k}{k!}, \\
Q_{AB}(s,-s) &= e^{-2J}\sum_{k=0}^{\infty} J^k \left(\frac{a_k}{k!} + \frac{Jc_{k-1}}{k!} + \frac{2Jb_k}{\sqrt{k!}\sqrt{(k+1)!}}\right), \\
Q_A(0) &= a_0 + a_1, \\
Q_B(0) &= a_0 + c_{-1}.
\end{aligned} \tag{3.23}
$$

The corresponding CH value $\langle CH_{tel}\rangle$ can be calculated by substituting the above relations into Eq. (2.89). The security key rate can be calculated by Eq. (2.94).

3.6 Simulation results

3.6.1 Logarithmic negativity of teleported DV entanglement

In this subsection, I determine the optimal gain g_{LN}^{opt} and the corresponding maximal logarithmic negativity E_{LN}^{max} achieved in different conditions. I simulate the teleportation process with different values of the squeezing parameter r, gain g and the channel transmissivities T_A, T_B. The logarithmic negativity is calculated based on Eqs. (3.10), (3.14), (3.15), (3.17) and (3.18). The results are shown in Fig. 5.1. I first vary the squeezing r while fixing the channel transmissivities at a few example values (Fig. 5.1, left column). Next, I fix the squeezing at $r = 2.395$ (so that $\cosh(2r) \approx 60$) while varying the channel transmissivities from 0 to 1 (Fig. 5.1, right column). It can be seen that when the squeezing is high, the optimal gain tends to $\sqrt{\frac{T_B}{T_A}}$ (Fig. 5.1 (c),(d)). High squeezing also leads to higher maximum logarithmic negativities. In the case where $T_A = T_B = 1$, E_{LN}^{max} approaches 1 (Fig. 5.1 (e), (f)), and the output is a perfect copy of the input, which is a maximally DV entangled state.

3.6.2 Comparison between a teleported and a directly distributed DV entangled state

In this subsection, I compare a teleported DV entangled state with a DV entangled state directly distributed from a satellite. I assume that both states are encoded in the photon-number basis and are given by $\rho_{CB''}$ (Eq. (3.13)) and ρ'_{AB} (Eq. (3.21)), respectively. The channel is assumed to be symmetric, ($T_A = T_B = T$) so that the optimal gain is unity. The total optical link loss in dB is defined by $-10\log_{10}(T^2)$.

The logarithmic negativity is calculated using Eqs. (3.17), (3.18), (2.77) and (2.78). At first, the squeezing value of the CV teleportation channel is set to a high value of $r = 2.395$, so that $\cosh(2r) = 60$. The result is plotted in red in Fig. 3.3, where we can see that the teleported DV entangled state (solid line) retains higher logarithmic negativity than the directly-distributed DV entangled state (dashed line). Note that, when the optical link loss is from 5 to 10dB, the logarithmic negativity of teleported entanglement is more than double that of directly-distributed entanglement.

Next, I perform a numerical search to find the threshold squeezing r_{th} where teleported entanglement starts to surpass directly-distributed entanglement. The average channel attenuation for the Earth-satellite channel is around 5 to 10dB for a down-link transmission [30]. At this range of loss, as can be seen from Fig. 3.3, the logarithmic negativity of directly-distributed entanglement is from 0.24 to 0.07. From Fig. 5.1 (e), specifically from the green dash-dotted line and the red dotted line, we can find that the teleported entanglement achieves the same level of logarithmic negativity at the threshold squeezing $r_{th} = 0.3$ to 0.5, which is achievable experimentally.

To calculate the keyrate, I follow the mathematical model in section 3.5, using the measurement setting of $s = 0.5$. I assume that the estimated bit error is zero and the squeezing is r=2.395. The result is plotted in black in Fig. 3.3. The solid line represents the key rate bound from the teleported entanglement, while the dashed line represents the key rate bound from the directly-distributed entanglement. At zero loss, my simulations show that when the squeezing is large ($r > 5$), the key rate bound derived from the teleported state

is approximately that of the key rate bound from the directly-distributed state. When the loss increases, the key rate bounds become zero because the CH inequality is no longer violated. For my settings, the key rate bounds are reduced below zero before the optical link loss reaches 1dB. For this low loss, the teleported entanglement produces a lower key rate bound than the directly-distributed entanglement. However, I do note that this result is a consequence of the specific QKD protocol used and the fact that entanglement and CH inequalities are not always directly related. I anticipate the key rate behavior to be different for other QKD protocols.

3.7 Conclusion

In this chapter, I have studied the effect of channel transmission loss on the creation of a CV entanglement channel. I then use the CV teleportation channel to teleport DV entanglement in the photon number basis. My result shows that the entanglement in the teleportation output is maximized by increasing the squeezing above 2.3, tuning the gain to $g_{LN}^{opt} = \sqrt{\frac{T_B}{T_A}}$ and minimizing channel transmission loss. For my experimental settings, I find that the teleported DV states can retain a significantly higher entanglement relative to the same states directly distributed from a satellite, especially for an optical link loss from 5 to 10dB. For a device-independent QKD protocol, the minimum key rate reduces to zero at around 1dB of loss, before teleported entanglement shows a significant advantage over directly-distributed entanglement. Note, DI-QKD protocols are the most secure but are known to produce low key rates.

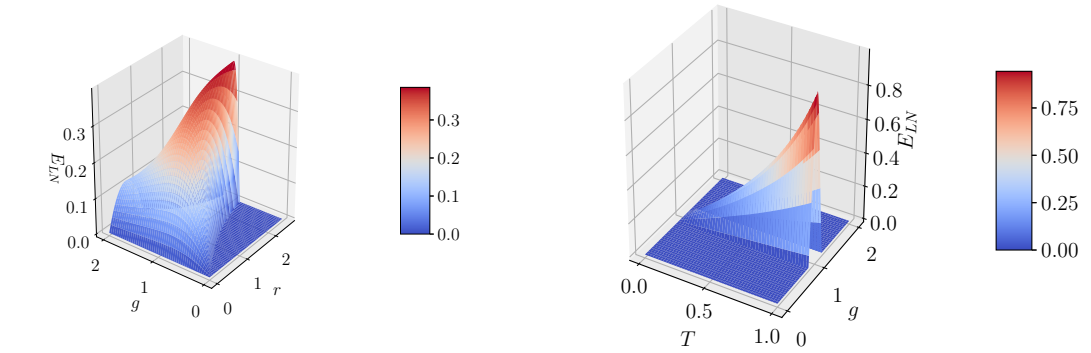

(a) E_{LN} when $T_A = T_B = 0.562$.

(b) E_{LN} when $T_A = T_B = T$.

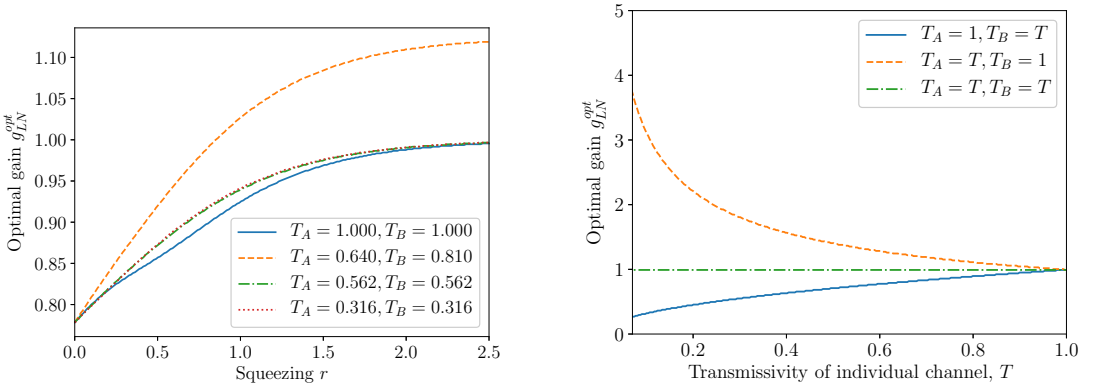

(c)

(d)

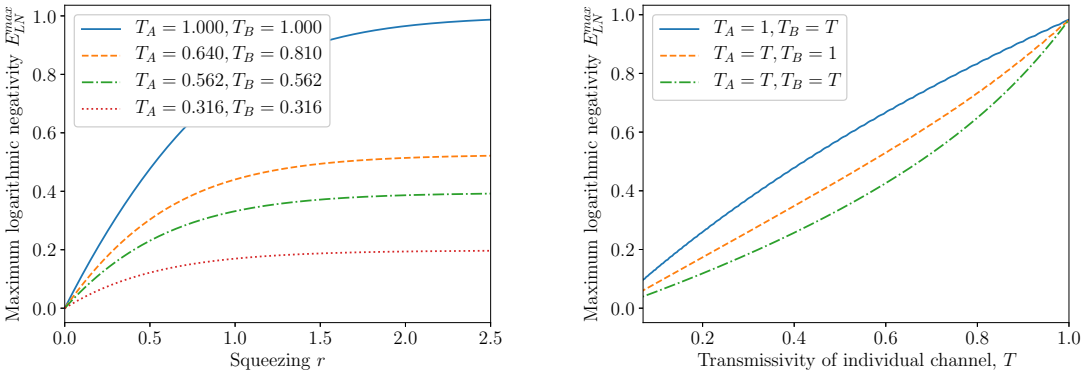

(e)

(f)

Figure 3.2: The logarithmic negativity E_{LN} of the teleportation-output is plotted versus different values of squeezing r, channel transmissivities T and teleportation gain g. In the left column (a,c,e), the squeezing ranges from 0 to 2.5 while the channel transmissivities are fixed at a few example values. It should be noted that when $T_A = T_B = 0.562$ and $T_A = T_B = 0.316$, the total channel loss is $-10\log_{10}(T_A T_B) = 5$dB and 10dB, respectively, which is the range of loss for a satellite down-link channel [30]. In the right column (b,d,f), the squeezing is fixed at $r = 2.395$ while the transmissivity T ranges from 0 to 1. The first row (a,b) shows the 3D plot of the logarithmic negativity when the gain g is varied as well. The second row (c,d) shows the optimal gain g_{LN}^{opt} that maximizes the logarithmic negativity; while the third row (e,f) shows the corresponding maximal logarithmic negativity E_{LN}. In general, we can see that E_{LN} reaches its maximum value of 1 when the squeezing is high ($r > 2.5$), when the gain is tuned to the optimal value $g_{LN}^{opt} = \sqrt{\frac{T_B}{T_A}}$, and when there is no channel loss, i.e., $T_A = T_B = 1$. (Taken from [31].)

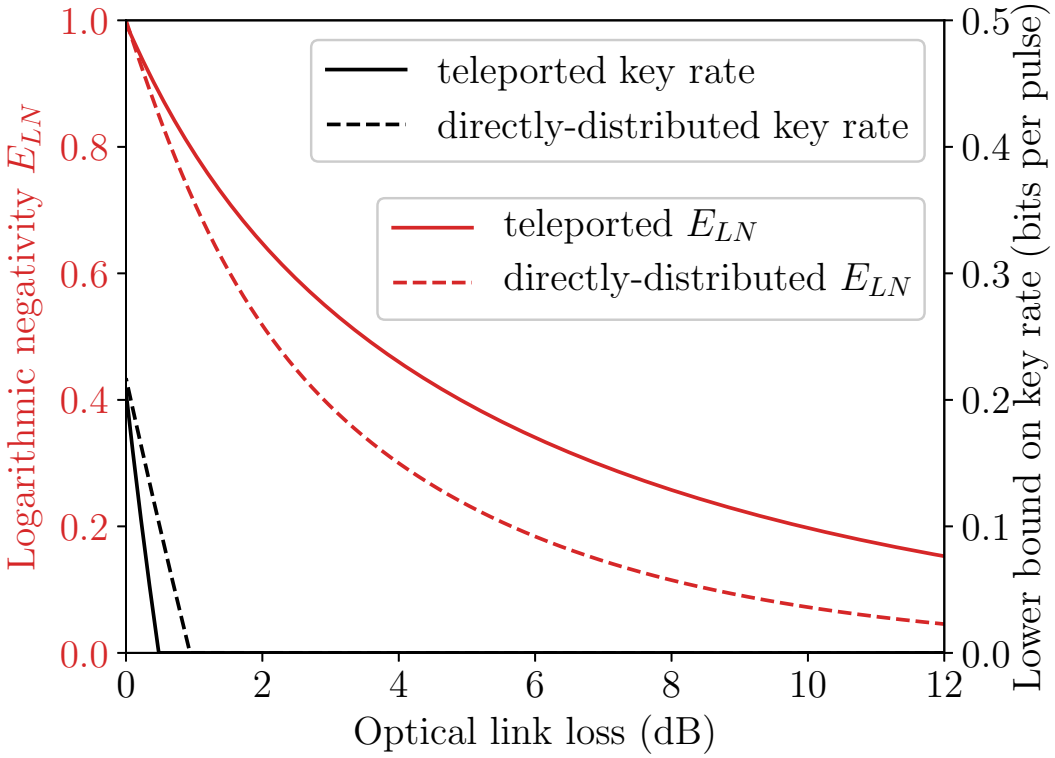

Figure 3.3: A comparison of DV entanglement distributed in two different ways: teleportation by a CV channel (solid lines) and direct down-link distribution from a satellite (dashed line). Here, the initial CV state (which formed the teleportation channel) had a squeezing value of $r = 2.395$. The logarithmic negativity is plotted in red while the resulting bound on the secure key rate is plotted in black. (Taken from [31].)

Chapter 4

Teleportation of a Schrödinger's-Cat State via Satellite-based Quantum Communications

In the previous chapter, I have presented the general mathematical framework to teleport an arbitrary state through an attenuated CV teleportation channel, with the specific example of teleporting one mode of a DV entangled state. In this chapter, I will study the case where the teleported state is a Schrödinger's cat state, whose quantum character is represented by the negativity of the Wigner function. For a lossless channel, past studies have shown that the negativity of the cat state can be preserved through teleportation. For a teleportation channel with fixed-attenuation, such as optical fibers, my result shows that the negativity of the cat state will disappear after 5dB of loss. I then go further to investigate the free-space channel between Earth and satellite. Due to atmospheric turbulence, the channel loss fluctuates following a probabilistic distribution. My result shows that the free-space channels can better preserve the fidelity of the input state as

compared to the fix-attenuation channel.

4.1 Introduction

The Schrödinger's-cat state is of fundamental interest because it represents quantum superposition between two macroscopic states. Experimentally, the cat state can be created from the macroscopic superposition of coherent states. Such a superposition is known to be useful for universal quantum computing using CV, where the quantum information is carried by the quadratures of the optical field [36]. CV protocols use homodyne (or heterodyne) detectors which are faster and more efficient (as compared to DV protocols, where the quantum information is carried in the polarization or the photon-number of single photons).

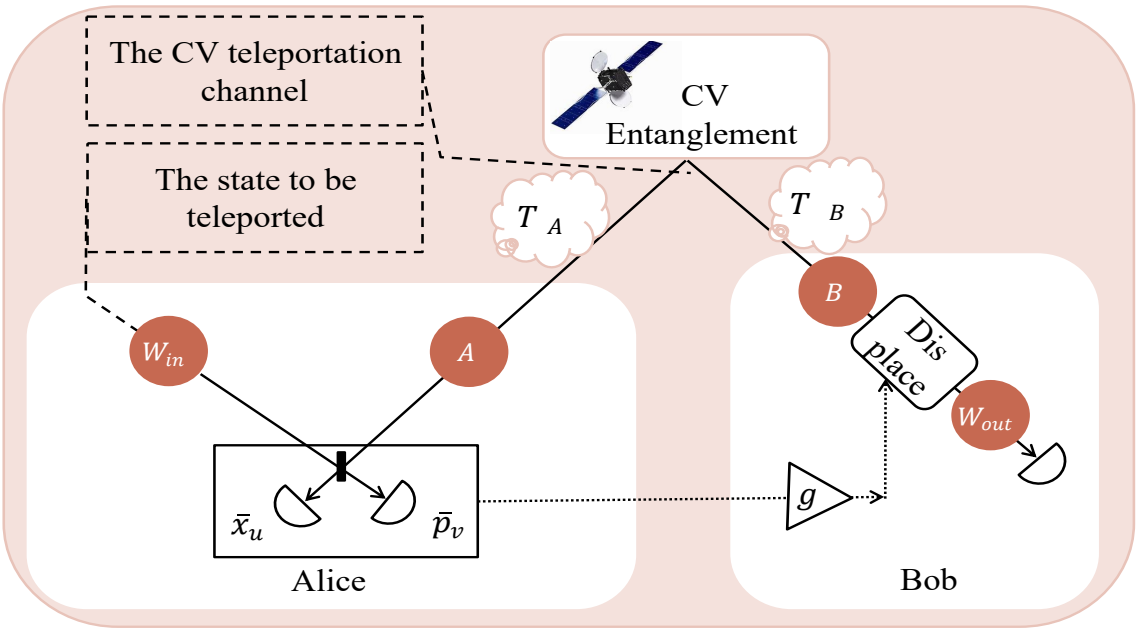

Figure 4.1: In the hybrid scheme, the CV entanglement $A - B$ is used as a teleportation channel. The channels have transmissivity T_A and T_B. The input state W_{in} is teleported from Alice to Bob, resulting in the output W_{out}. (Taken from [37].)

Among the different quantum communication protocols, teleportation is one of the most useful. In many cases, information is transferred through optical fibers, which exhibits fixed attenuation. Since the loss in optical fiber scales exponentially with distance, ter-

restrial quantum communication has been limited to a few hundred kilometer. Quantum signal cannot be further amplified due to the no-cloning theorem [25–27]. In contrast, for a satellite in low orbit (400 to 600km from Earth), the channel is only affected by atmospheric turbulence. In fact, for a down-link channel of less than 500km above the ground, the average attenuation was demonstrated to be around 30dB [38]. In this chapter, I use CV entanglement distributed from a satellite as a CV teleportation channel. I then use this channel to distribute a Schrödinger-cat state. Such a protocol has the potential to extend quantum information protocols over a global scale.

The satellite-Earth channel is a free-space fading channel, where the loss is caused by diffraction, absorption/scattering, and atmospheric turbulence [39]. The most significant loss comes from the turbulence, which could be characterized by the Rytov parameter σ_R. This parameter is a function of the atmospheric refraction index structure constant parameter C_n^2, which can be calculated from the wind velocity and the altitude. Large turbulent eddies can cause beam-wandering, while smaller eddies can induce beam broadening. The channel attenuation has a probabilistic nature and can be simulated by different mathematical models. In the beam-wandering model, the beam profile is modeled by a circular Gaussian shape. The turbulence causes the beam center to fluctuate around the center of the receiver aperture, resulting in a misalignment which reduces the transmissivity of the beam [40]. Recently, a new fading model was introduced taking into account additional deformation and broadening effects. In this chapter, I call this model the elliptic model. In the elliptic model, the beam profile at the receiver aperture is broadened and has an elliptic shape. There is fluctuations not only in the beam center but also in the widths of the elliptic profile [41].

Past studies have shown that the quantum character of the cat state can be preserved after CV teleportation [42], however, the channel transmission loss has not been taken into consideration. Our main contributions in this chapter are:

- I derive a mathematical model detailing how channel attenuation affects the quality of the CV teleportation channel, as well as the quality of the teleportation outcome.

- For fixed attenuation I determine the loss conditions under which the cat state can be preserved.
- I adopt the free-space fading channel between the Earth and a satellite for a typical down-link channel and determine whether the teleported cat state retains higher fidelity in such channels relative to a fixed attenuation channel.

The structure of the remainder of this chapter is as follows. Section 4.2 studies the mathematical model for CV teleportation. Section 4.3 studies different models of atmospheric turbulence. Section 4.4 shows my simulation, while section 4.5 summarizes my findings and discusses future work.

4.2 Teleportation of a Schrödinger's cat through an attenuated CV teleportation channel

In this chapter, an attenuated TMSV state is used as the CV teleportation channel (see Fig. 4.1). The teleportation through an attenuated TMSV channel has been discussed in section 3.3. Let $W_{in}(\alpha)$ be the input state (Fig. 4.1) with $\alpha = x + jp$. After CV teleportation with gain g, the output Wigner function becomes a Gaussian convolution of the input, followed by a rescaling of $\alpha_{out} \to \alpha_{out}/g$ in phase space.

$$\begin{aligned} W_{out}(\alpha_{out}) &= \frac{1}{g^2}\left[W_{in} * G_{\sigma_{tel}}\right](\frac{\alpha_{out}}{g}) \\ &= \frac{1}{g^2}\iint dxdpW_{in}(\alpha)G_{\sigma_{tel}}\left(\frac{\zeta_{out}}{g} - \zeta\right), \end{aligned} \tag{4.1}$$

where the Gaussian function with variance σ_{tel} is given by Eqs. (2.67) and (2.68). When $T_A = T_B = 1$, we have [34]

$$\sigma_{tel} = \frac{e^{2r}(1-g)^2 + e^{-2r}(1+g)^2}{4g^2}. \tag{4.2}$$

When we further set $g = 1$, the variance is simplified to $\sigma_{tel} = e^{-2r}$, so $W_{out}(\alpha_{out}) = W_{in} * G_{e^{-2r}}(\alpha_{out})$ [3, 32, 33].

In this section, I will study the specific case where the input is the odd Schrödinger's-cat state $|cat_+\rangle$ with the normalization constant N_+ given in Eqs. (2.4) and (2.5). The Wigner function of the cat state ($W_c(\alpha)$) is given by Eq. (2.56). When $W_c(\alpha)$ is used as the input state $W_{in}(\alpha)$, the output of the CV teleportation is calculated by Eq. (3.9). When the CV teleportation channels has transmissivities $T_A = T_B = T$ and the optimal gain is unity, the Gaussian variance σ_{tel} in Eq. (3.10) becomes

$$\sigma_{tel} = T\mathrm{e}^{-2r} + (1 - T). \tag{4.3}$$

When taking into account the detector amplitude-efficiency η, the Gaussian variance is modified to ${\sigma_{tel}}' = \sigma_{tel} + \frac{1-\eta^2}{\eta^2}$.

In order to quantify the quality of the output state as compared to input state, I use the entanglement fidelity [43]. For the Schrödinger's-cat state, the fidelity is given in [33]

$$F = \frac{1}{1 + {\sigma_{tel}}'} - \frac{1 + \mathrm{e}^{-4|\alpha_0|^2} - \exp\frac{-4{\sigma_{tel}}'|\alpha_0|^2}{1+{\sigma_{tel}}'} - \exp\frac{-4|\alpha_0|^2}{1+{\sigma_{tel}}'}}{2(1 + {\sigma_{tel}}')(1 + \mathrm{e}^{-2|\alpha_0|^2}\cos\phi)^2}. \tag{4.4}$$

4.3 Earth-satellite Channel

In this chapter, I will discuss the atmospheric turbulence above the Earth surface, and how it affects the transmissivity of the Earth-satellite channel. The effects of the turbulence can be described by two mathematical models: the beam-wandering model studies the beam displacement from the receiver's aperture, while the elliptic model studies the broadening and distortion of the beam profile.

4.3.1 Atmospheric turbulence

The level of atmospheric turbulence is characterized by the Rytov parameter [41]

$$\sigma_R^2 = 1.23 C_n^2 k^{7/6} L^{11/6}, \tag{4.5}$$

where k is the wave number of the light mode and L is the altitude of the satellite. The refraction index structure constant parameter C_n^2 can be calculated from the altitude h and wind velocity v [44]

$$\begin{aligned} C_n^2(h) &= 0.00594(v/27)^2(h\times 10^{-5})^{10}e^{-h/1000} \\ &\quad +2.7\times 10^{-16}e^{-h/1500}+Ae^{-h/100}, \end{aligned} \tag{4.6}$$

where $A = C_n^2(h=0)$ is the refraction index constant structure parameter at ground level, in units of $\mathrm{m}^{-2/3}$. The mean value of A according to WRF model is $9.6\text{x}10^{-14}\mathrm{m}^{-2/3}$.

4.3.2 Beam-wandering model

Beam wandering causes the beam center to be displaced from the aperture center. On the aperture plane, the position of the beam centroid relative to the aperture center can be modeled by two random variables (x, y) following two independent Gaussian probability distributions with variance σ^2

$$p(x,y) = p(x)p(y) = \frac{1}{2\pi\sigma^2}\exp\left(-\frac{x^2+y^2}{2\sigma^2}\right). \tag{4.7}$$

Thus, the displacement $d = \sqrt{(x^2+y^2)}$ follows the Rice distribution:

$$p(d) = \frac{d}{\sigma^2}\exp\left(-\frac{d^2}{2\sigma^2}\right). \tag{4.8}$$

The Rytov parameter σ_R^2 is related to the beam-wandering variance σ^2 by [41]

$$\sigma^2 = 0.33W_0^2\sigma_R^2\Omega^{-7/6}, \tag{4.9}$$

where

$$\Omega = \frac{\pi W_0^2}{L\lambda}, \tag{4.10}$$

and W_0 is the beam width at the transmitter plane. Let W be the beam width at the receiver plane, let a be the aperture radius at the receiver, we define the ratios $d_a = d_0/a$

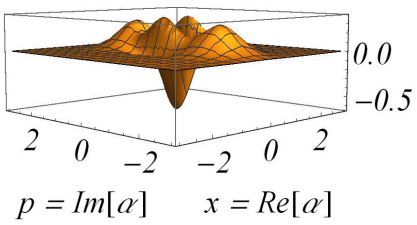

(a) Input cat state.

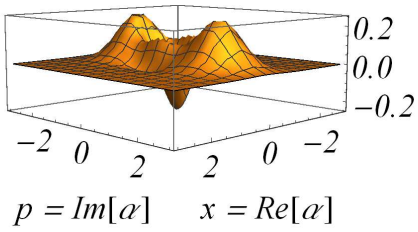

(b) Teleported cat state, no loss, $\eta^2 = 1$.

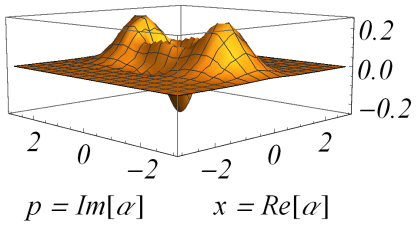

(c) Teleported cat state, no loss, $\eta^2 = 0.99$.

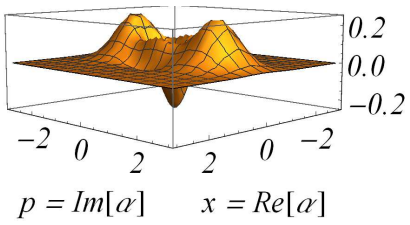

(d) Teleported cat state, 5dB loss, $\eta^2 = 1$.

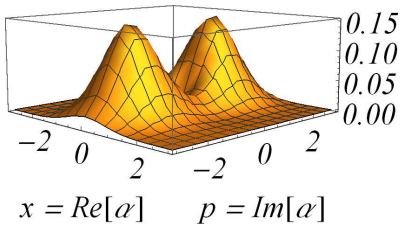

(e) Teleported cat state, 5dB loss, $\eta^2 = 0.99$.

Figure 4.2: (a) The Wigner function of a Schrödinger cat state, with $\alpha_0 = 1.5$ and $\phi = \pi$. (b), (c), (d), (e) The Wigner function of the cat state after CV teleportation (with r=1.15) is plotted for different values of channel loss and detector amplitude-efficiency (η). (Taken from [37].)

and $W_a = W/a$. The transmittance of the beam is found by integration to find the fraction of energy passing through the aperture. Let t be the transmission coefficient, the channel transmissivity $T = t^2$ can be approximated by

$$T = T_0 \exp\left[-\left(\frac{d_a}{R_a}\right)^{\gamma}\right], \tag{4.11}$$

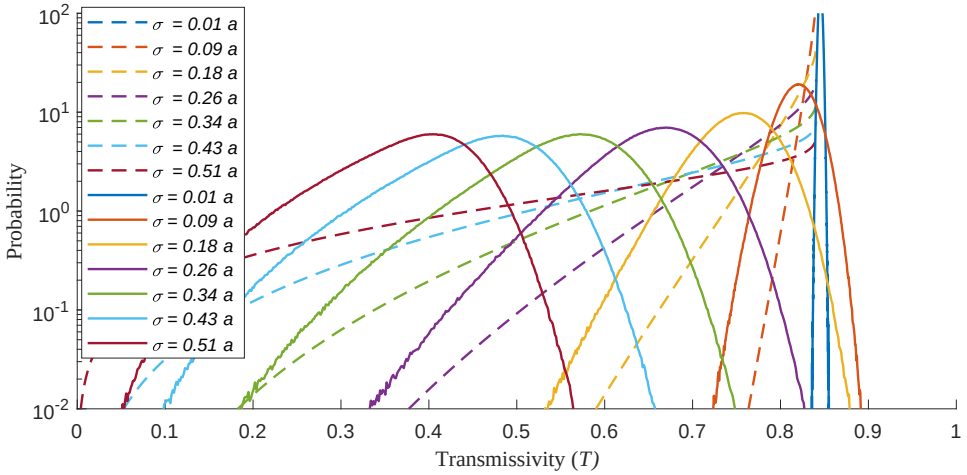

Figure 4.3: For a free-space fading channel, the distribution of channel transmissivity T is plotted with different ratios of the beam-wandering standard deviation (σ) to the aperture radius (a). The dashed lines represent the distributions from the beam-wandering model, while the solid lines represent the distributions from the elliptic model. (Taken from [37].)

where the parameters are defined as

$$T_0 = 1 - \exp\left(-\frac{2}{W_a^2}\right), \tag{4.12}$$

$$\lambda = \frac{8}{W_a^2} \times \frac{\exp\left(-\frac{4}{W_a^2}\right) I_1\left(\frac{4}{W_a^2}\right)}{1 - \left(-\frac{4}{W_a^2}\right) I_0\left(\frac{4}{W_a^2}\right)} \times \frac{1}{\ln\left[\frac{2t_0^2}{1-\left(-\frac{4}{W_a^2}\right) I_0\left(\frac{4}{W_a^2}\right)}\right]}, \tag{4.13}$$

$$R_a = \left[\ln\left(\frac{2t_0^2}{1 - \exp\left(-\frac{4}{W_a^2}\right) I_0\left(\frac{4}{W_a^2}\right)}\right)\right]^{-\frac{1}{\lambda}}, \tag{4.14}$$

where $I_0(x)$ and $I_1(x)$ are the modified Bessel functions. By plugging the probability distribution (Eq. (4.8)) into the transmissivity (Eq. 4.11)), we can derive the probability distribution of the transmission coefficient t

$$p(t) = \frac{2R_a^2}{\sigma_a^2 \lambda t}\left(2\ln\frac{t_0}{t}\right)^{\left(\frac{2}{\lambda}-1\right)} \exp\left[-\frac{R_a^2}{2\sigma_a^2}\left(2\ln\frac{t_0}{t}\right)^{\frac{2}{\lambda}}\right], \tag{4.15}$$

where $\sigma_a = \sigma/a$. Essentially, the distribution of the transmission coefficient t does not depend on the absolute value of the aperture radius a, but only depends on the ratios of W and σ to a.

4.3.3 Elliptic model

The elliptic model takes into account not only the beam-wandering effect, but also beam-broadening, and the non-circular beam distortions caused by turbulence in the Earth's atmosphere [45] [41]. Let x and y be the deviation (on the x- and y-axis, respectively) of the beam centroid from the aperture center, a be the aperture radius of the detector, and ϕ be the beam rotation angle, $\phi_0 = \tan^{-1}\frac{y}{x}$. The effective spot radius of an equivalent Gaussian beam is modelled as

$$\begin{aligned} W_{\text{eff}}^2(\phi) = \; & 4a^2 \left\{ \mathcal{W}\left(\tfrac{4a^2}{W_1 W_2} e^{(a^2/W_1^2)\left[1+2\cos^2(\phi)\right]} \right.\right. \\ & \left.\left. \times \; e^{(a^2/W_2^2)\left[1+2\sin^2(\phi)\right]} \right) \right\}^{-1} , \end{aligned} \tag{4.16}$$

where $\mathcal{W}(\cdot)$ is the Lambert W function. The maximal transmissivity at $x = y = 0$ (i.e. no deviation) is

$$\begin{aligned} T_{E_0} = \; & 1 - I_0\left(a^2\left[\tfrac{1}{W_1^2} - \tfrac{1}{W_2^2}\right]\right) e^{-a^2\left(1/W_1^2 + 1/W_2^2\right)} \\ & -2\left[1 - e^{-(a^2/2[1/W_1 - 1/W_2]^2)}\right] \\ & \times \exp\left\{ - \left[\frac{\frac{(W_1+W_2)^2}{\left|W_1^2 - W_2^2\right|}}{R\left(\frac{1}{W_1} - \frac{1}{W_2}\right)} \right]^{\lambda\left(\frac{1}{W_1} - \frac{1}{W_2}\right)} \right\} \end{aligned} , \tag{4.17}$$

where $R(W)$ and $\lambda(W)$ are the scaling and shaping functions

$$R(W) = \left[\ln\left(2\frac{1 - \exp\left[-\frac{1}{2}a^2W^2\right]}{1 - \exp\left[-a^2W^2\right] I_0(a^2W^2)} \right) \right]^{-\lambda^{-1}} , \tag{4.18}$$

$$\begin{aligned} \lambda(W) = \; & 2a^2W^2 \tfrac{\exp\left[-a^2W^2\right] I_1(a^2W^2)}{1 - \exp[-a^2W^2] I_0(a^2W^2)} \\ & \times \left(2\tfrac{1 - \exp\left[-\frac{1}{2}a^2W^2\right]}{1 - \exp[-a^2W^2] I_0(a^2W^2)} \right), \end{aligned} \tag{4.19}$$

respectively. Here W_1 and W_2 are the semi-major and semi-minor axis lengths of the ellipse, respectively, and $I_i(\cdot)$ is the modified Bessel function of i-th order. The channel transmissivity $T_E = t_E^2$ is given by

$$T_E = T_{E_0} \exp\left\{ - \left[\frac{\sqrt{x^2 + y^2}/a}{R(\frac{2}{W_{eff}(\phi - \phi_0)})} \right]^{\lambda\left(2/W_{eff}(\phi - \phi_0)\right)} \right\}. \tag{4.20}$$

When considering isotropic turbulence, the rotation angle ϕ is evenly distributed. The statistical properties of $\{x, y, \theta_1, \theta_2\}$ are determined by W_0, σ_R^2, the wavelength of the beam, and the propagation distance. For more details, see supplementary materials in reference [41].

4.4 Simulation and results

4.4.1 Fixed attenuation channel

In this subsection, I perform the teleportation of a Schrödinger's-cat state following Eqs. (3.9), (2.56) and (4.3). The channels are assumed to be symmetric with fixed attenuation $T_A = T_B = T$. The fixed parameters are the squeezing parameter $r = 1.15$, $\phi = \pi$ and $\alpha_0 = 1.5$. The detector amplitude-efficiency η and the channel transmissivity T are varied. Fig. 4.2 shows the Schrödinger cat state before and after teleportation. The quantum character of the state is manifested in the negative value at the center of the Wigner function. My results show that when the detector efficiency is taken into account ($\eta^2 = 0.99$), the quantum character of the cat state is lost after 5dB of fixed attenuation ($T_A = T_B = 0.562$).

4.4.2 Fading channel

In this subsection, I assume a realistic scenario where the satellite is 500km high, the beam waist at the transmitter is $W_0 = 12$cm, and the wavelength is 780nm. In this setting, the beam width at the receiver is around $W =$1m. The receiver is designed to have an aperture $a = W = 1$m. The variance of the beam center (σ^2) is the key parameter that influences the transmissivity of the channel.

In Fig. 4.3, the probability density $p(T)$ is plotted against T for different values of σ, where higher σ represents stronger atmospheric disturbance. The dashed lines show the probability densities generated by the beam-wandering model, while the solid lines show

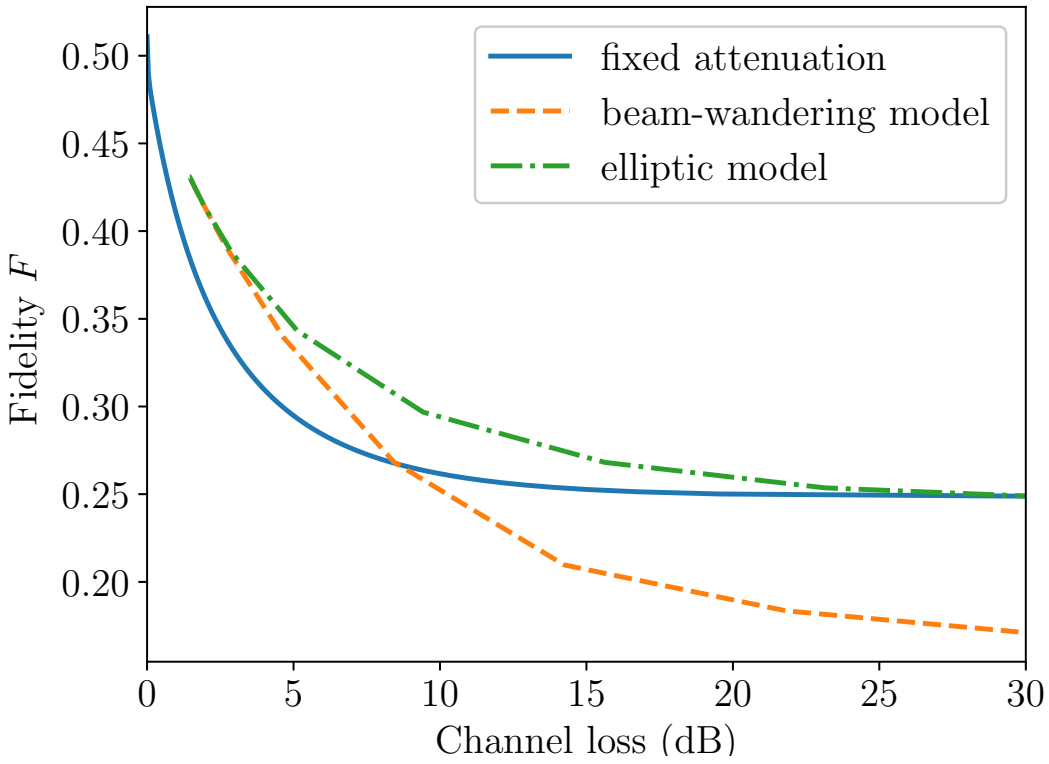

Figure 4.4: The fidelity (F) of the Schrödinger's-cat state is plotted for different teleportation channels. The blue line represents the teleportation fidelity of a fixed attenuation channel (plotted against the fixed channel loss). The other two lines represent a free-space fading channel with atmospheric turbulence (plotted against the mean channel loss). The attenuation of the free-space channel is generated by different models: the beam-wandering model (in orange dashed line) and the elliptic model (in green dot-dashed line). (There is a cut-off loss that results from the cut-off transmissivity defined in Eqs. (4.12) and (4.17)). (Taken from [37].)

the probability densities generated by the elliptic model. In addition, my calculation shows that, in the beam-wandering model, the mean loss of 50% (3dB) is reached when $\sigma = 0.7a$, where a is the aperture radius. On the other hand, for the elliptical model, the mean loss of 50% (3dB) is reached earlier, when $\sigma = 0.4a$.

4.4.3 Fidelity

The fidelity of the Schrödinger's-cat state after teleportation is calculated based on Eq. (4.4) and is plotted in Fig. 4.4. The different lines represent different attenuation models for the CV teleportation channel. The mean loss (in dB) is calculated by $-10\log_{10}(T_A T_B)$

where T_A and T_B are the channel transmissivities. The fixed parameters are $r = 1.15$, $\alpha_0 = 1.5$, $\phi = \pi$ and $\eta^2 = 0.99$.

The solid blue line in Fig. 4.4 represents a fixed attenuation channel. The dashed orange line and the dash-dotted green line represents free-space channels with atmospheric turbulence described by the beam-wandering and the elliptic model, respectively. T_A and T_B are generated by the simulation in subsection 4.4.2, while the teleportation gain is set as $g = \sqrt{T_B/T_A}$. The output of the teleportation is calculated and compared to the input state. Our results show that when the mean loss of the fading channel is less than 30dB, which is the regime considered applicable for a satellite down-link channel from LEO, the fidelity of the cat state is higher than that for a cat-state that has passed through fixed attenuation channel of loss equal to the corresponding mean fading loss.

Furthermore, due to the different distributions of T for the elliptical model and the beam-wandering model (see Fig. 4.3), these models possess different probability distributions for the variance σ_{tel} used in Eq. (3.9). This has the consequence that for a given mean loss the elliptical model leads to higher fidelities. I have also carried out additional simulations for a wide range of parameter settings (r from 0.5 to 3, $|\alpha_0|^2$ from 0.1 to 25, and ϕ from 0 to π) and find the main conclusions drawn here remain intact.

4.5 Conclusion

In this chapter, I studied the effect of channel transmission loss on CV entanglement. Specifically, I used a lossy CV teleportation channel to teleport a Schrödinger's-cat state. My results showed that when the channel has fixed attenuation (such as in an optical fiber), the quantum character of the cat state is lost after 5dB. I then investigated the scenario of an Earth-satellite channel with transmission loss induced by atmospheric turbulence. The attenuation in this realistic channel follows a probabilistic distribution which can be modeled by either the beam-wandering model or the elliptic model. My results showed that for a down-link channel of less than 500km of length, i.e, less than 30dB of average

loss, the teleported state attains higher fidelity than in a fixed attenuation channel. In reality, the beam profile after atmospheric turbulence is a hybrid of the beam-wandering and the elliptic models. While most past studies are based on the beam-wandering model, experimentalists should beware that the actual fidelity should be higher according to the elliptical model.

Chapter 5

Satellite-based Distribution of Hybrid Entanglement

Previous chapters have studied the attenuated CV teleportation channel where the input is a DV entangled state or a Schrödinger 's cat state. In this chapter, I study for the first time the teleportation of a hybrid entangled state through such a lossy teleportation channel. Next, I will determine the conditions where teleportation can retain a higher level of entanglement as compared to direct distribution from the satellite. In particular, for the typical loss level of the satellite-to-Earth channel, it is always better to teleport the DV mode of the hybrid entangled state instead of the CV mode.

5.1 Introduction

The Schrödinger-cat state is of fundamental importance because it represents the superposition of two macroscopic quantum states. In the optical domain, the cat state can take the form of a superposition of two coherent states of opposite phase [46]. Such a cat state finds applications in many areas including universal quantum computing via CV, where the quantum information is encoded in the quadratures of the optical field [36, 47–49]. CV

protocols can in many instances be more efficient relative to DV versions of the same protocols, where the quantum information is encoded in the DV properties of single photons such as polarization or photon-number [8, 16, 50].

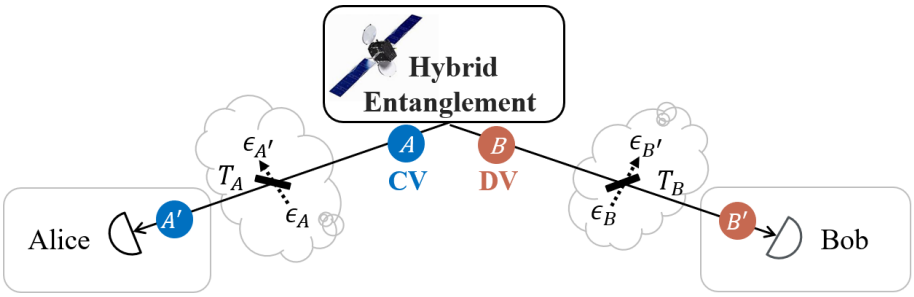

(a) Direct distribution.

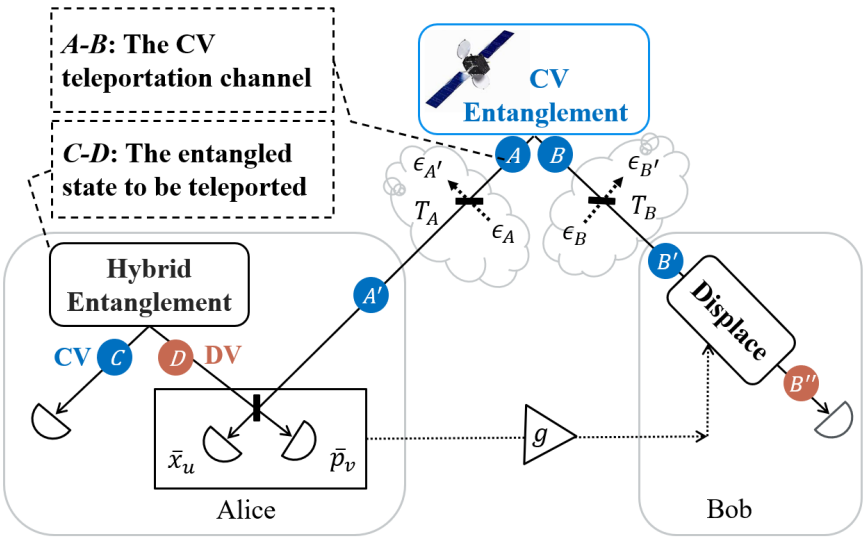

(b) Teleportation.

Figure 5.1: (a) The hybrid entangled state $A-B$ is beamed directly from the satellite down to Earth. (b) The CV entangled state (TMSV state) $A-B$ is generated on board the satellite and get attenuated after traveling through atmospheric turbulence. The resulting state $A'-B'$ is used as a TMSV teleportation channel. The hybrid entangled state $C-D$ is comprised of the CV mode C and the DV mode D. Mode D (or C) is teleported through the teleportation channel, with teleportation gain g, to create the final mode B'' entangled to C (or D). $\bar{x}_u$ and $\bar{p}_v$ stand for the Bell state measurement outputs. In both plots, ϵ_A and ϵ_B represent the vacuum contributions, while T_A and T_B represent the channel transmissivities. (Taken from [51].)

Hybrid entanglement between quantum states can be considered as the entanglement between two physically separated modes, one of which is encoded in DV information while the other is encoded in CV information. An example of such a hybrid state would be entanglement between the CV Schrödinger-cat states and the DV photon-number states.

Such a hybrid entangled state has been demonstrated to have applications in quantum control, specifically for the remote preparation of a CV qubit using a local DV mode [8,9,52,53]. In quantum communications, hybrid entangled states can lead to the violation of the steering inequality [54], thus generating a positive key rate for the one-sided device-independent QKD protocol [55]. Impressively, the hybrid entangled state can be used to distribute secret keys over 1000km of optical fibre via the coherent-state-based twin-field QKD protocol [56–58].

In this chapter, I will take the DV component of the hybrid state to be in the number basis. However, I briefly mention how a DV component encoded in polarization may also be considered within my framework. For polarization-based entanglement, the teleportation through a CV teleportation channel was proposed but not yet realized experimentally [4, 59]. On the other hand, the teleportation of a photon-number state through a CV teleportation channel can be easier implemented and was already demonstrated in [16,60]. In addition, for hybrid entangled states where the DV mode is encoded in the polarization basis, each polarization input state can be broken down to two separate photon-number states in two polarization modes $|H\rangle_{in} = |1\rangle_{H,in}|0\rangle_{V,in}$ and $|V\rangle_{in} = |0\rangle_{H,in}|1\rangle_{V,in}$, with H and V denoting the horizontal and vertical polarizations. The two polarization modes can be consecutively teleported through the same CV teleportation channel. If the two teleportation operations are carried out within a short time-period, I can assume that the CV teleportation channel stays the same, and that the two operations are independent processes. The overall fidelity is thus a product of each operation's fidelity [61, 62].

Hybrid entanglement may become particularly important for long-distance communication via satellites, especially as a mechanism to interconnect (via teleportation and entanglement swapping) terrestrial devices operating within heterogeneous (mixed DV and CV) networks. Connecting such mixed-technology devices through traditional fiber links has its limitations since the loss in optical fiber scales exponentially with distance.

In contrast, for a satellite in LEO, which is about 500km above the ground, the Micius experiment has shown that the down-link (satellite to ground) channel is largely affected by atmospheric turbulence and diffraction [38]. In future systems, this level of loss will

likely be further mitigated by large receiving telescopes and/or adaptive optical tracking techniques [63, 64]. It is, therefore, of great interest to explore the use of entanglement distribution via satellites as a means to interconnect terrestrial devices running on mixed technologies.

Previous work has studied the scenario where both the state to be teleported and the teleportation channel are hybrid entangled states [9, 65–67]. However, the generation of a hybrid-entangled teleportation resource channel is experimentally challenging - especially when the source is placed on board a satellite as in Fig. 5.1a. On the other hand, the generation of CV entanglement in the form of a TMSV state is relatively easy to achieve and potentially available as a satellite-based technology [38]. In this chapter, I study, for the first time, the use of a TMSV channel (as shown in Fig. 5.1b) to teleport a hybrid entangled state.

The use of the attenuated TMSV channel for teleportation (henceforth simply referred to as the teleportation) was previously studied using the Wigner function formalism [33], the P-function formalism [68], and the Fock basis formalism [61]. However, such mathematical models were limited to the teleportation of common single-mode states, such as the vacuum state, the single-photon state [61], the coherent state [68], or the Schrödinger's cat state [33]. The Wigner function formalism was then extended to describe the teleportation of one mode in a *pure* DV entangled state, which takes into consideration the cross-diagonal matrices of zero and single photon numbers, $|0\rangle\langle 1|$ and $|1\rangle\langle 0|$ [4, 31]. Different from [4, 31, 33, 61, 68], in this chapter, I describe the teleportation of either the DV or CV mode of *hybrid* entanglement. Since the DV mode is only comprised of *zero* and *single* photon numbers, the DV-mode teleportation can be derived by extending the Wigner-function formalism in [4, 31]. The CV mode, however, is comprised of cross-diagonal matrices of *multi*-photon numbers, where the teleportation is too complex to be described by the previous formalisms. As a solution, I use the characteristic function formalism to model the CV-mode teleportation, identifying a new simplification in this formalism that allows for analytic determination of the teleportation fidelity of a hybrid state.

Hybrid entanglement distribution will be important for the design of future heterogeneous

quantum networks. My two main novel contributions to this end, relative to the existing literature, are:

- I determine the teleportation fidelity of a hybrid state when either the DV or CV mode is passed through a lossy TMSV channel.
- I calculate the fidelity of a hybrid entangled state following a direct distribution of each mode through a differential lossy channel; using this calculation to then quantify the difference in performance between the direct and teleported distribution schemes as a function of loss in the satellite-to-ground channel.

The structure of the remainder of this chapter is as follows. Section 5.2 introduces hybrid entanglement. Section 5.3 studies the direct distribution of hybrid entanglement, with transmission loss in both the DV and CV mode. Section 5.4 studies the teleportation of either mode of the hybrid entanglement via a lossy TMSV channel. Section 5.5 compares the results between CV/DV-mode teleportation and direct distribution, highlighting the different advantages of both schemes. Section 5.6 summarizes my findings.

5.2 Hybrid entanglement

Consider the hybrid entanglement between cat states as introduced in Eq. (2.21)

$$|\psi\rangle_h = \frac{|cat_-\rangle_C|0\rangle_D + |cat_+\rangle_C|1\rangle_D}{\sqrt{2}}, \tag{5.1}$$

where for clarity, I have specified the spatial modes as C and D following the setup in Fig. 5.1b. $|0\rangle$ and $|1\rangle$ are the vacuum state and the single photon state in the photon-number basis, while the Schrödinger cat states are given by Eq. (2.4), with $N_\pm$ being the normalization constant given by Eq. (2.5). The corresponding density operator is given by

$$\begin{aligned}\rho_h =& \frac{1}{2}\left(|cat_-\rangle_C\langle cat_-| \otimes |0\rangle_D\langle 0| + |cat_+\rangle_C\langle cat_+| \otimes |1\rangle_D\langle 1|\right.\\ &\left. + |cat_-\rangle_C\langle cat_+| \otimes |0\rangle_D\langle 1| + |cat_+\rangle_C\langle cat_-| \otimes |1\rangle_D\langle 0|\right).\end{aligned} \tag{5.2}$$

Due to the mathematical complexity of the hybrid entangled state in Eq. (5.1), especially when describing the teleportation of the CV mode in section 5.4.2, we will find it useful to introduce approximations to such a hybrid entangled state in the cases of large and small cat states. The mathematical approximations we utilize will have high fidelity with Eq. (5.1) and will allow for improved analytical insight. Deviation from results produced using Eq. (5.1) directly will be inconsequential [10, 69, 70]. My main interest will be large cat states, as they tend to be of wider interest in a range of quantum information protocols, such as information processing [71]. However, I will still investigate the small cat-state limit, mainly because the results in this regime provide firm upper bounds on the teleportation fidelities as the cat states approach the so-called 'kitten' states.

Large cat states ($|\alpha_0| > 1$): In order to give an approximation for large cat states, we first need to rearrange the terms in Eq. (5.1) by substituting

$$|0\rangle = (|+\rangle + |-\rangle)/\sqrt{2},\ |1\rangle = (|+\rangle - |-\rangle)/\sqrt{2}, \tag{5.3}$$

giving

$$|\psi\rangle_h = \frac{1}{\sqrt{2}}\left(\frac{|cat_-\rangle_C + |cat_+\rangle_C}{\sqrt{2}}|+\rangle_D + \frac{|cat_-\rangle_C - |cat_+\rangle_C}{\sqrt{2}}|-\rangle_D\right). \tag{5.4}$$

When $|\alpha_0| > 1$, the states in mode C can be approximated by coherent states, and the hybrid entangled state becomes [10, 69]

$$|\psi\rangle_h^{(large)} \approx \frac{|\alpha_0\rangle_C|+\rangle_D - |-\alpha_0\rangle_C|-\rangle_D}{\sqrt{2}}\ . \tag{5.5}$$

The corresponding density matrix is

$$\begin{aligned}\rho_h^{(large)} \approx \frac{1}{2}\,(&|\ \alpha_0\rangle_C\langle\ \alpha_0| \otimes |+\rangle_D\langle+| + |-\alpha_0\rangle_C\langle-\alpha_0| \otimes |-\rangle_D\langle-| \\ &- |\ \alpha_0\rangle_C\langle-\alpha_0| \otimes |+\rangle_D\langle-| - |-\alpha_0\rangle_C\langle\ \alpha_0| \otimes |-\rangle_D\langle+|)\,.\end{aligned} \tag{5.6}$$

Eqs. (5.5) and (5.6) will be useful for the calculation of the fidelity of CV-mode teleportation later in section 5.4.2.

Small cat states ($|\alpha_0| < 0.5$): We can approximate small cat states with the SMSV state and the Single-Photon Subtracted Squeezed Vacuum (1PS) state [10, 70],

$$|cat_+\rangle \approx |SMSV\rangle = S(\zeta)|0\rangle, \tag{5.7}$$

$$|cat_-\rangle \approx |1PS\rangle = \frac{\hat{a}S(\zeta)|0\rangle}{\sinh\zeta} = S(\zeta)|1\rangle, \tag{5.8}$$

where $S(\zeta)$ is the single-mode squeezing operator, and $\zeta = se^{j\theta}$ with s being the single-mode squeezing parameter. For an arbitrary value of α_0 in Eq. (2.4), the fidelity between $|cat_-\rangle$ and $|1PS\rangle$ becomes maximized when α_0 is real and [70]

$$s = \frac{\sqrt{9 + 4\alpha_0^4} - 3}{2\alpha_0^2}. \tag{5.9}$$

Under these conditions, the fidelity between the SMSV (or 1PS) state and $|cat_+\rangle$ (or $|cat_-\rangle$) increases as α_0 decreases, and the fidelity approaches unity as α_0 approaches 0.5 [70]. For simplicity, I will henceforth set $\theta = 0$ and write the single-mode squeezing operator as $S(s)$. The original hybrid entangled state in Eq. (5.1) can therefore be approximated as [10]

$$|\psi\rangle_h^{(small)} \approx \frac{S_C(s)|1\rangle_C \otimes |0\rangle_D + S_C(s)|0\rangle_C \otimes |1\rangle_D}{\sqrt{2}}. \tag{5.10}$$

The corresponding density matrix is given by

$$\begin{aligned}\rho_h^{(small)} \approx \frac{1}{2}\Big[&S(s)|1\rangle_C\langle 1|S(s)^\dagger \otimes |0\rangle_D\langle 0| + S(s)|0\rangle_C\langle 0|S(s)^\dagger \otimes |1\rangle_D\langle 1| \\ &+ S(s)|1\rangle_C\langle 0|S(s)^\dagger \otimes |0\rangle_D\langle 1| + S(s)|0\rangle_C\langle 1|S(s)^\dagger \otimes |1\rangle_D\langle 0|\Big].\end{aligned} \tag{5.11}$$

From now on, I will assume that α_0 is real in all my calculations. For simplicity, I will also replace the approximation signs following $\rho_h^{(large)}$ and $\rho_h^{(small)}$ with equalities. Henceforth, whenever I mention large (small) cat states, or large (small) α_0, I am referring to $\alpha_0 > 1$ ($\alpha_0 < 0.5$).

Intermediate cat states ($0.5 \leq \alpha_0 \leq 1$): In this case, we use the exact form of the hybrid entangled state in Eq. (5.1) to carry out my calculations. These lead to relations that are perhaps less illuminating as the approximate solutions above, and as such relegate this exposition to appendix A.1. We shall see how the results from this exact solution match the approximate solutions in the relevant range.

Hybrid entanglement with large cat states can be deterministically generated by a weak and dispersive light-matter interaction [5], or by a cross-Kerr nonlinear interaction between a coherent state and a photon-number qubit state [6, 7]. However, due to experimental challenges in nonlinear optics, hybrid entanglement with small cat states can be more easily produced by using linear optics and a probabilistic heralded scheme [8–11]. The latter setup takes a small cat state ($|cat_+\rangle$) as an input, and produces hybrid entanglement between small cat states and qubit states. The advantage of the heralded scheme is that the loss in the heralding channel only affects the success rate but not the fidelity of the final entanglement. Such a scheme is particularly beneficial for long-distance communication [10]. In addition, the heralded setup in [9] has the potential to be extended for cat states with higher amplitudes.

5.3 Direct distribution of a hybrid entangled state through lossy channels

The hybrid entangled state is given in Eq. (5.2), where the cat states have amplitude α_0. I refer to the modes as given in Fig. 5.1a. That is, I denote the two modes of the entanglement as A and B, where A is the CV mode and B is the DV mode. For each mode, the channel attenuation can be modeled by a beam splitter with corresponding transmissivities T_A and T_B. The photonic loss in *either* the DV or CV mode has been studied in previous papers [56, 58, 72, 73]. However, when the loss is present in *both* the DV and CV mode, the resulting density matrix becomes complex and has not been hitherto determined. In this section, I calculate this density matrix and then determine the resulting fidelity of the hybrid state after direct distribution from the satellite.

At the first beam splitter, the CV mode A is mixed with the auxiliary vacuum mode ϵ_A to give the output modes A' and $\epsilon_{A'}$. For a general bi-coherent input state $|\alpha\rangle_A|\alpha_\epsilon\rangle_{\epsilon_A}$, the beam splitter transformation gives

$$|\alpha\rangle_A|\alpha_\epsilon\rangle_{\epsilon_A} \to |\sqrt{T_A}\alpha - \sqrt{1-T_A}\alpha_\epsilon\rangle_{A'}|\sqrt{T_A}\alpha_\epsilon + \sqrt{1-T_A}\alpha\rangle_{\epsilon_{A'}}. \tag{5.12}$$

At the second beam splitter, the DV mode B is mixed with the auxiliary vacuum mode ϵ_B, giving the output modes B' and $\epsilon_{B'}$. Let the creation operators of the four modes be $\hat{a}_B^\dagger$, $\hat{a}_{\epsilon_B}^\dagger$,$\hat{a}_{B'}^\dagger$ and $\hat{a}_{\epsilon_{B'}}^\dagger$, the beam splitter transformation can then be written as

$$\hat{a}_B^\dagger \to \sqrt{T_B}\,\hat{a}_{B'}^\dagger + \sqrt{1-T_B}\,\hat{a}_{\epsilon_{B'}}^\dagger, \tag{5.13}$$

$$\hat{a}_{\epsilon_B}^\dagger \to \sqrt{T_B}\,\hat{a}_{\epsilon_{B'}}^\dagger - \sqrt{1-T_B}\,\hat{a}_{B'}^\dagger. \tag{5.14}$$

After applying the beam splitter transformations, the density matrix of the hybrid entangled state (Eq. (5.2)) becomes $\rho_{A'\epsilon_{A'}B'\epsilon_{B'}}$. The transmitted state can be found by tracing out the auxiliary output modes $\epsilon_{A'}$ and $\epsilon_{B'}$. Mode $\epsilon_{B'}$ can be easily traced out, since it is a DV mode. The CV mode $\epsilon_{A'}$ can be traced out by applying the integration

$$\int \frac{d^2\beta}{\pi} \langle\beta|\rho_{A'\epsilon_{A'}B'\epsilon_{B'}}|\beta\rangle_{\epsilon_{A'}}, \tag{5.15}$$

where β is a generic complex number. This integration can be calculated by applying the following well-known identities for a general coherent state $|\alpha\rangle_{\epsilon_{A'}}$

$$\begin{aligned}
&\int \frac{d^2\beta}{\pi} \langle\beta| \pm \alpha\rangle_{\epsilon_{A'}} \langle\pm\alpha|\beta\rangle_{\epsilon_{A'}} = 1, \\
&\int \frac{d^2\beta}{\pi} \langle\beta| \pm \alpha\rangle_{\epsilon_{A'}} \langle\mp\alpha|\beta\rangle_{\epsilon_{A'}} = \exp\left(-2|\alpha|^2\right).
\end{aligned} \tag{5.16}$$

After tracing out the auxiliary modes (where the details can be found in appendix A.2), we find the directly-distributed state

$$\begin{aligned}
\rho_{A'B'} = \mathrm{Tr}_{\epsilon_{A'}\epsilon_{B'}}(\rho_{A'\epsilon_{A'}B'\epsilon_{B'}}) = \\
\frac{1}{2}\Big\{ |\sqrt{T_A}\alpha_0\rangle_A\langle\sqrt{T_A}\alpha_0| \otimes [(a_1+a_2)|0\rangle_B\langle 0| + a_3|1\rangle_B\langle 1| + a_4|0\rangle_B\langle 1| + a_4|1\rangle_B\langle 0|] \\
+ |-\sqrt{T_A}\alpha_0\rangle_A\langle-\sqrt{T_A}\alpha_0| \otimes [(a_1+a_2)|0\rangle_B\langle 0| + a_3|1\rangle_B\langle 1| - a_4|0\rangle_B\langle 1| - a_4|1\rangle_B\langle 0|] \\
+e^{-2(1-T_A)\alpha_0^2} |\sqrt{T_A}\alpha_0\rangle_A\langle-\sqrt{T_A}\alpha_0| \otimes [(a_1-a_2)|0\rangle_B\langle 0| + a_3|1\rangle_B\langle 1| + a_4|0\rangle_B\langle 1| - a_4|1\rangle_B\langle 0|] \\
+e^{-2(1-T_A)\alpha_0^2} |-\sqrt{T_A}\alpha_0\rangle_A\langle\sqrt{T_A}\alpha_0| \otimes [(a_1-a_2)|0\rangle_B\langle 0| + a_3|1\rangle_B\langle 1| - a_4|0\rangle_B\langle 1| + a_4|1\rangle_B\langle 0|] \Big\},
\end{aligned} \tag{5.17}$$

where

$$a_1 = \frac{1-T_B}{N_+^2},\ a_2 = \frac{1}{N_-^2},\ a_3 = \frac{T_B}{N_+^2},\ a_4 = \frac{\sqrt{T_B}}{N_+N_-}, \tag{5.18}$$

with $N_\pm$ defined in Eq. (2.5).

After calculating the directly-distributed state, I will compare it to the original hybrid entangled state - using fidelity as the key performance metric. However, since in some applications the logarithmic negativity of the entangled state is useful, that metric will also be discussed. The mathematical formulas to calculate the logarithmic negativity and fidelity were introduced by Eqs. (2.77) and (2.80), respectively.

5.4 Teleportation through a TMSV channel

The CV teleportation through a noiseless TMSV channel has been introduced in section 2.5.2 using both the photon-number basis and the Wigner function-formalism. In this section, I detail the teleportation through an attenuated TMSV teleportation channel (Fig. 5.1b), where the input mode is either the DV or the CV mode of the hybrid entangled state. The CV entangled state $A-B$ is created on the satellite, then transmitted down to Alice and Bob, with channel transmissivities T_A and T_B, respectively, resulting in the attenuated TMSV channel $A'-B'$. When the input mode is the DV mode (mode D) of the hybrid entangled pair $C-D$, the CV teleportation channel teleports D to B'', resulting in the entanglement between C and B''. Otherwise, when the input mode is the CV mode, C is teleported to B'', resulting in the entanglement between D and B''.

When the teleportation involves lossy channels, non-unity teleportation gain, and hybrid input states, the mathematics become more complex, and I have to use another formalism such as the Wigner function or the characteristic formalism. In the following two subsections, I will present the mathematical models that describe the teleportation of either the DV or CV mode of a hybrid entangled state through an attenuated TMSV channel.[(1)]

[(1)]The models developed in this chapter have been verified by teleporting a simple vacuum state through a symmetric channel, which produces the same fidelity as the analytical results in [68] and [61].

5.4.1 Teleporting the DV mode of hybrid entanglement

In order to describe the teleportation of the DV mode of the hybrid entanglement through the CV teleportation channel, I will use the Wigner function representation. I first study a general input state with the Wigner function $W_{in}(\alpha)$, where $\alpha = x + jp$ with non-zero real values x and p. Let $G_{\sigma_{tel}}(\alpha)$ denote a Gaussian function introduced in Eq. (2.67), with x and p denoting two uncorrelated random variables with equal variance σ_{tel}. The teleported Wigner function after a attenuated TMSV channel is given by Eq. (3.9) with the Gaussian variance σ_{tel} given by Eq. (3.10), where g is the teleportation gain. For fixed values of T_A and T_B, the calculation of the logarithmic negativity has shown that the optimal gain g increases with r, and reaches its maximal value at $r \simeq 2.5$ [31]. From now on, for simplicity, whenever I mention the 'optimal gain', I am referring to the optimal gain when the initial squeezing satisfies $r > 2.5$. When $T_A = T_B = 1$, the optimal gain is approximately $g \approx 1$, and I have $\sigma_{tel} = \exp(-2r)$ [33]. When the channels are asymmetric, i.e., $T_A \neq T_B$, the teleportation (in terms of logarithmic negativity and fidelity) is optimized when $g \approx \sqrt{\frac{T_B}{T_A}}$ [31]. Note that tuning the gain further does not improve the fidelity much, thus, from now on, I will simply replace the approximation signs by the equal signs.

When the input mode is the DV mode (D) of a hybrid entangled pair $C-D$, the subspace of C stays the same, while the subspace of D is transformed. Mode D can be decomposed to different terms $|m\rangle_D\langle n|$ ($m, n \in \{0, 1\}$), with Wigner functions $W^{|m\rangle_D\langle n|}(\alpha_D)$. The teleportation of each term is described by Eqs. (2.67), (3.9), (3.10) and (3.12). The teleportation transformation has been previously calculated for the case where mode D is part of a Bell state [4,31]. When mode D is part of hybrid entanglement, we recognize that the initial hybrid entanglement ($|\psi\rangle_h$ in Eq. (5.2)) has a form that is similar to a Bell state, where $|cat_-\rangle_C$ corresponds to $|1\rangle_C$, and $|cat_+\rangle_C$ corresponds to $|0\rangle_C$. By transforming the subspace of mode D similar to that described in [4, 31], and then converting the Wigner

formalism to the density-matrix formalism, we find the DV-mode teleported state

$$\begin{aligned}\rho_{tel} &= \sum_{k=-1}^{\infty} \rho_k, \text{ where} \\ \hat{\rho}_k &= a_k|cat_+\rangle_C\langle cat_+| \otimes |k\rangle_{B''}\langle k| + b_k|cat_-\rangle_C\langle cat_+| \otimes |k\rangle_{B''}\langle k+1| \\ &\quad + b_k|cat_+\rangle_C\langle cat_-| \otimes |k+1\rangle_{B''}\langle k| + c_k|cat_-\rangle_C\langle cat_-| \otimes |k+1\rangle_{B''}\langle k+1|, \end{aligned} \tag{5.19}$$

where a_k, b_k and c_k are defined by Eqs. (3.14), (3.15) and (3.16).

In the density matrix representation, the teleported state ρ_{tel} can be compared to the perfect hybrid entangled state ρ_h by using the measures of fidelity (Eq. (2.80)) and logarithmic negativity (Eq. (2.76)). The simulation results are shown in section 5.5.

5.4.2 Teleporting the CV mode of hybrid entanglement

In this section, I will discuss how to teleport the CV mode C of the hybrid entangled state $D-C$ through the TMSV channel to obtain the final entangled state $D-B''$. (Note that, in this section, I swap the order of modes C and D in Fig. 5.1b). Due to mathematical complexity, I will rewrite all required states in the characteristic-function formalism and approximate the hybrid entangled state $(D-C)$ for the limits of large and small cat states in section 5.2.

The characteristic function has been introduced in section 2.4.1. In the following, I will describe the characteristic function of the attenuated TMSV channel and the input hybrid entangled state.

Characteristic function of an attenuated TMSV state

Let us model the two down-link channels by two beam splitters with transmissivities T_A and T_B, respectively. At the beam splitters, modes A and B are mixed with the auxiliary vacuum modes ϵ_A and ϵ_B, respectively, giving the output modes $\{A', \epsilon_{A'}\}$, and $\{B', \epsilon_{B'}\}$, respectively. Let $t_l = \sqrt{T_l}, r_l = \sqrt{1-T_l}$ with $l \in \{A, B\}$, the beam splitter transformation

can be given by

$$\beta_{l'} = t_l\beta_l - r_l\beta_{\epsilon_l}, \quad \beta_{\epsilon_{l'}} = r_l\beta_l + t_l\beta_{\epsilon_l}. \tag{5.20}$$

The four-mode characteristic equation before the beam splitter is given by multiplying the characteristic functions of the TMSV state with the vacuum states

$$\chi_{TMSV}(\beta_A, \beta_B)\chi_{vac}(\beta_{\epsilon_A})\chi_{vac}(\beta_{\epsilon_B}). \tag{5.21}$$

The beam splitter transformation can be performed by substituting $\beta_l = t_l\beta_{l'} + r_l\beta_{\epsilon_{l'}}$ and $\beta_{\epsilon_l} = -r_l\beta_{l'} + t_l\beta_{\epsilon_{l'}}$ into the above equation. It has been shown that the tracing out of the vacuum modes is equivalent to setting $\beta_{\epsilon_{l'}} = 0$ [74]. The resulting attenuated TMSV state is given by

$$\chi_{TMSV}^{(T_A,T_B)}(\beta_{A'}, \beta_{B'}) = \chi_{TMSV}(\sqrt{T_A}\beta_{A'}, \sqrt{T_B}\beta_{B'})\chi_{vac}(-\sqrt{1-T_A}\beta'_A)\chi_{vac}(-\sqrt{1-T_B}\beta'_B). \tag{5.22}$$

Characteristic function of a hybrid entangled state

The exact density matrix of the hybrid entangled state is given by Eq. (5.2), in which the cat state $|cat_\pm\rangle$ has the characteristic function given by Eq. (2.44). Due to the mathematical complexity, especially when calculating the matrix $|cat_\pm\rangle\langle cat_\mp|$ in Eq. (5.2), I will approximate the hybrid entangled state for the cases of large α_0 (Eq. (5.6)) and small α_0 (Eq. (5.11)). For hybrid states with intermediate sizes, an exact calculation can be found in appendix A.1.

When the cat state is large: The hybrid entangled state can be approximated by $\rho_h^{(large)}$ in Eq. (5.6). Given the definition of the characteristic function (Eq. (2.37)), and the form of the density matrix of the approximate hybrid state (in Eq. (5.6)), we will find it useful to introduce a new function for a general matrix M

$$X_M(\beta) = \mathrm{Tr}\left[MD(\beta)\right]. \tag{5.23}$$

From the linearity of the trace function, the above function is also linear with respect to the matrix M [2]. For a tensor product of the form $M = M_1 \otimes M_2$, we have

$$X_M(\beta_1, \beta_2) = \mathrm{Tr}\left[M_1 \otimes M_2 \; D_1(\beta_1) \otimes D_2(\beta_2)\right] = X_{M_1}(\beta_1) X_{M_2}(\beta_2), \tag{5.24}$$

where the last equality makes use of the tensor product property of the trace function. From the linearity and tensor product property above, the characteristic function of $\rho_h^{(large)}$ can thus be found by applying Eq. (5.24) to a modified Eq. (5.6) where the order of modes C and D is swapped (see discussion start of section 5.4.2), giving

$$\begin{aligned}\chi_h^{(large)}(\beta_D, \beta_C) =& \frac{1}{2}\Big[X_{|+\rangle\langle+|}(\beta_D) X_{|\alpha_0\rangle\langle\alpha_0|}(\beta_C) + X_{|-\rangle\langle-|}(\beta_D) X_{|-\alpha_0\rangle\langle-\alpha_0|}(\beta_C) \\ & - X_{|+\rangle\langle-|}(\beta_D) X_{|\alpha_0\rangle\langle-\alpha_0|}(\beta_C) - X_{|-\rangle\langle+|}(\beta_D) X_{|-\alpha_0\rangle\langle\alpha_0|}(\beta_C)\Big]. \end{aligned} \tag{5.25}$$

In the following, we will explicitly calculate the individual terms in the above equation.

From the change of basis in Eq. (5.3), we can show

$$\begin{aligned} X_{|+\rangle\langle+|}(\beta) &= \frac{1}{2}\left[X_{|0\rangle\langle0|}(\beta) + X_{|1\rangle\langle1|}(\beta) + X_{|0\rangle\langle1|}(\beta) + X_{|1\rangle\langle0|}(\beta)\right], \\ X_{|-\rangle\langle-|}(\beta) &= \frac{1}{2}\left[X_{|0\rangle\langle0|}(\beta) + X_{|1\rangle\langle1|}(\beta) - X_{|0\rangle\langle1|}(\beta) - X_{|1\rangle\langle0|}(\beta)\right], \\ X_{|+\rangle\langle-|}(\beta) &= \frac{1}{2}\left[X_{|0\rangle\langle0|}(\beta) - X_{|1\rangle\langle1|}(\beta) - X_{|0\rangle\langle1|}(\beta) + X_{|1\rangle\langle0|}(\beta)\right], \\ X_{|-\rangle\langle+|}(\beta) &= \frac{1}{2}\left[X_{|0\rangle\langle0|}(\beta) - X_{|1\rangle\langle1|}(\beta) + X_{|0\rangle\langle1|}(\beta) - X_{|1\rangle\langle0|}(\beta)\right], \end{aligned} \tag{5.26}$$

where

$$\begin{aligned} X_{|0\rangle\langle0|}(\beta) &= \langle0|D(\beta)|0\rangle = e^{-|\beta|^2/2}, \\ X_{|1\rangle\langle1|}(\beta) &= \langle1|D(\beta)|1\rangle = e^{-|\beta|^2/2}(1-|\beta|^2), \\ X_{|0\rangle\langle1|}(\beta) &= \langle1|D(\beta)|0\rangle = \beta e^{-|\beta|^2/2}, \\ X_{|1\rangle\langle0|}(\beta) &= \langle0|D(\beta)|1\rangle = \left[\langle0|D^\dagger(-\beta)\right]|1\rangle = -\beta^* e^{-|\beta|^2/2}. \end{aligned} \tag{5.27}$$

In Eq. (5.27) we have used the appropriate relation for the displaced number states [75–77]. For the terms $|\pm\alpha\rangle\langle\pm\alpha|$ and $|\pm\alpha\rangle\langle\mp\alpha|$ in Eq. (5.6), we have [2]

$$\begin{aligned} X_{|\pm\alpha_0\rangle\langle\pm\alpha_0|}(\beta) &= e^{-\frac{|\beta|^2}{2}} e^{\pm j 2\mathrm{Im}[\beta\alpha_0^*]}, \\ X_{|\pm\alpha_0\rangle\langle\mp\alpha_0|}(\beta) &= e^{-\frac{|\beta\pm2\alpha_0|^2}{2}}. \end{aligned} \tag{5.28}$$

By substituting Eqs. (5.26), (5.27) and (5.28) into Eq. (5.25), we can find the characteristic function of the hybrid entangled state with large α_0.

When the cat state is small: The hybrid entangled state can be approximated by $\rho_h^{(small)}$. By applying Eqs. (2.37) and (5.24) to Eq. (5.11), the characteristic function of $\rho_h^{(small)}$ is given by

$$\chi_h^{(small)}(\beta_D,\beta_C) = \frac{1}{2}\Big[X_{|0\rangle\langle 0|}(\beta_D)X_{S(s)|1\rangle\langle 1|S(s)^\dagger}(\beta_C) + X_{|1\rangle\langle 1|}(\beta_D)X_{S(s)|0\rangle\langle 0|S(s)^\dagger}(\beta_C) + X_{|0\rangle\langle 1|}(\beta_D)X_{S(s)|1\rangle\langle 0|S(s)^\dagger}(\beta_C) + X_{|1\rangle\langle 0|}(\beta_D)X_{S(s)|0\rangle\langle 1|S(s)^\dagger}(\beta_C)\Big]. \tag{5.29}$$

For the matrix $S(s)|m\rangle\langle n|S(s)^\dagger$ with $m,n\in\{0,1\}$ and s defined in Eq. (5.9), $X_{S(s)|m\rangle\langle n|S(s)^\dagger}(\beta)$ can be found by applying the relation

$$S^\dagger(s)D(\beta)S(s) = D(\tilde{\beta}), \quad \text{with} \quad \tilde{\beta} = \beta\cosh s - \beta^*\sinh s. \tag{5.30}$$

As a result, $X_{S(s)|0\rangle\langle 0|S(s)^\dagger}(\beta)$ and $X_{S(s)|1\rangle\langle 1|S(s)^\dagger}(\beta)$ can be found by substituting $\tilde{\beta}$ for β in Eq. (5.27), giving [13, 14]

$$X_{S(s)|0\rangle\langle 0|S(s)^\dagger}(\beta) = X_{|0\rangle\langle 0|}(\tilde{\beta}), \tag{5.31}$$

$$X_{S(s)|1\rangle\langle 1|S(s)^\dagger}(\beta) = X_{|1\rangle\langle 1|}(\tilde{\beta}). \tag{5.32}$$

Our calculation shows that $X_{S(s)|0\rangle\langle 1|S(s)^\dagger}(\beta)$ and $X_{S(s)|1\rangle\langle 0|S(s)^\dagger}(\beta)$ can also be found by the same substitution

$$X_{S(s)|0\rangle\langle 1|S(s)^\dagger}(\beta) = X_{|0\rangle\langle 1|}(\tilde{\beta}), \tag{5.33}$$

$$X_{S(s)|1\rangle\langle 0|S(s)^\dagger}(\beta) = X_{|1\rangle\langle 0|}(\tilde{\beta}). \tag{5.34}$$

(Note that, when $s=0$, $\tilde{\beta}$ becomes β, we have $X_{S(0)|m\rangle\langle n|S(0)^\dagger}(\beta) = X_{|m\rangle\langle n|}(\beta)$). We can now write

$$\chi_h^{(small)}(\beta_D,\beta_C) = \frac{1}{2}\Big[X_{|0\rangle\langle 0|}(\beta_D)X_{|1\rangle\langle 1|}(\tilde{\beta}_C) + X_{|1\rangle\langle 1|}(\beta_D)X_{|0\rangle\langle 0|}(\tilde{\beta}_C) + X_{|0\rangle\langle 1|}(\beta_D)X_{|1\rangle\langle 0|}(\tilde{\beta}_C) + X_{|1\rangle\langle 0|}(\beta_D)X_{|0\rangle\langle 1|}(\tilde{\beta}_C)\Big]. \tag{5.35}$$

By substituting Eq. (5.27) into the above equation, we can find the characteristic function of a hybrid entangled state with small α_0.

5.4.3 Calculate the fidelity

The fidelity between two general states was introduced in section 2.6.2. For two arbitrary two-mode states, for example, the original hybrid entangled state $\chi_h(\beta_D, \beta_C)$ and the CV-mode teleported state $\chi_{tel}(\beta_D, \beta_{B''})$, the fidelity is given by

$$F = \iint d^2\beta_D d^2\beta_{B''} \frac{1}{\pi^2} \chi_h(\beta_D, \beta_{B''}) \chi_{tel}(-\beta_D, -\beta_{B''}). \tag{5.36}$$

In order to verify my calculations, we check that the fidelity of a state with itself is always unity. For example, in the limit where the TMSV channel has no loss and has infinite squeezing, $\chi_{tel}(\beta_D, \beta_{B''})$ becomes identical to $\chi_h(\beta_D, \beta_{B''})$. For the case of large α_0, $\chi_h^{(large)}(\beta_D, \beta_{B''})$ is given by Eq. (5.25). The multiplication

$$\chi_h^{(large)}(\beta_D, \beta_{B''}) \chi_h^{(large)}(-\beta_D, -\beta_{B''}) \tag{5.37}$$

creates a summation of sixteen different terms. The summation can be simplified by exploiting the symmetry of the DV mode, which gives

$$\begin{aligned}
&\int d^2\beta_D \frac{1}{\pi} X_{|+\rangle\langle+|}(\beta_D) X_{|+\rangle\langle+|}(-\beta_D) = \int d^2\beta_D \frac{1}{\pi} |X_{|+\rangle\langle+|}(\beta_D)|^2 = 1, \\
&\int d^2\beta_D \frac{1}{\pi} X_{|+\rangle\langle-|}(\beta_D) X_{|-\rangle\langle+|}(-\beta_D) = 1, \\
&\int d^2\beta_D \frac{1}{\pi} X_{|-\rangle\langle-|}(\beta_D) X_{|-\rangle\langle-|}(-\beta_D) = \int d^2\beta_D \frac{1}{\pi} |X_{|-\rangle\langle-|}(\beta_D)|^2 = 1, \\
&\int d^2\beta_D \frac{1}{\pi} X_{|-\rangle\langle+|}(\beta_D) X_{|+\rangle\langle-|}(-\beta_D) = 1,
\end{aligned} \tag{5.38}$$

while the other twelve integrations give zero, for example,

$$\begin{aligned}
&\int d^2\beta_D \frac{1}{\pi} X_{|+\rangle\langle+|}(\beta_D) X_{|-\rangle\langle-|}(-\beta_D) = 0, \\
&\int d^2\beta_D \frac{1}{\pi} X_{|+\rangle\langle+|}(\beta_D) X_{|+\rangle\langle-|}(-\beta_D) = 0, \\
&\dots
\end{aligned} \tag{5.39}$$

The fidelity of a large hybrid entangled state with itself is therefore given by the four non-zero terms

$$\begin{aligned}F_{self}^{(large)} = \frac{1}{4}\Bigg[&\int d^2\beta_D \frac{1}{\pi}|X_{|+\rangle\langle+|}(\beta_D)|^2 \times \int d^2\beta_{B''}\frac{1}{\pi}|X_{|\alpha_0\rangle\langle\alpha_0|}(\beta_{B''})|^2 \\ &+ \int d^2\beta_D \frac{1}{\pi}|X_{|-\rangle\langle-|}(\beta_D)|^2 \times \int d^2\beta_{B''}\frac{1}{\pi}|X_{|-\alpha_0\rangle\langle-\alpha_0|}(\beta_{B''})|^2 \\ &+ \int d^2\beta_D \frac{1}{\pi}X_{|+\rangle\langle-|}(\beta_D)X_{|-\rangle\langle+|}(-\beta_D) \\ &\quad \times \int d^2\beta_{B''}\frac{1}{\pi}X_{|\alpha_0\rangle\langle-\alpha_0|}(\beta_{B''})X_{|-\alpha_0\rangle\langle\alpha_0|}(-\beta_{B''}) \\ &+ \int d^2\beta_D \frac{1}{\pi}X_{|-\rangle\langle+|}(\beta_D)X_{|+\rangle\langle-|}(-\beta_D) \\ &\quad \times \int d^2\beta_{B''}\frac{1}{\pi}X_{|-\alpha_0\rangle\langle\alpha_0|}(\beta_{B''})X_{|\alpha_0\rangle\langle-\alpha_0|}(-\beta_{B''})\Bigg]. \end{aligned} \tag{5.40}$$

All the integrals above are equal to unity, giving $F_{self}^{(large)} = 1$. Similarly, for the case of small α_0, $\chi_h^{(small)}(\beta_D, \beta_{B''})$ is given by Eq. (5.35). The DV mode in the $\{|0\rangle, |1\rangle\}$ basis also exhibits a symmetry similar to that in Eqs. (5.38) and (5.39). From such a symmetry, the fidelity of the state to itself can be simplified from sixteen terms to only four non-zero terms

$$\begin{aligned}F_{self}^{(small)} = \frac{1}{4}\Bigg[&\int d^2\beta_D \frac{1}{\pi}|X_{|0\rangle\langle0|}(\beta_D)|^2 \times \int d^2\beta_{B''}\frac{1}{\pi}|X_{|1\rangle\langle1|}(\tilde{\beta}_{B''})|^2 \\ &+ \int d^2\beta_D \frac{1}{\pi}|X_{|1\rangle\langle1|}(\beta_D)|^2 \times \int d^2\beta_{B''}\frac{1}{\pi}|X_{|0\rangle\langle0|}(\tilde{\beta}_{B''})|^2 \\ &+ \int d^2\beta_D \frac{1}{\pi}X_{|0\rangle\langle1|}(\beta_D)X_{|1\rangle\langle0|}(-\beta_D) \times \int d^2\beta_{B''}\frac{1}{\pi}X_{|1\rangle\langle0|}(\tilde{\beta}_{B''})X_{|0\rangle\langle1|}(-\tilde{\beta}_{B''}) \\ &+ \int d^2\beta_D \frac{1}{\pi}X_{|1\rangle\langle0|}(\beta_D)X_{|0\rangle\langle1|}(-\beta_D) \times \int d^2\beta_{B''}\frac{1}{\pi}X_{|0\rangle\langle1|}(\tilde{\beta}_{B''})X_{|1\rangle\langle0|}(-\tilde{\beta}_{B''})\Bigg]. \end{aligned} \tag{5.41}$$

All the integrals above are equal to unity, again giving $F_{self}^{(small)} = 1$.

When the CV mode of the hybrid entangled state is teleported, mode C will be teleported to mode B''. Assuming a teleportation gain of $g = 1$,[(2)] the teleportation output is given by [13, 15]

$$\chi_{tel}(\beta_D, \beta_{B''}) = \chi_h(\beta_D, \beta_{B''})\chi_{TMSV}^{(T_A,T_B)}(\beta_{B''}^*, \beta_{B''}), \tag{5.42}$$

[(2)] $g = 1$ was found to be the optimal gain for symmetric channels with regard to the logarithmic negativity [4, 31].

where the channel is given by the attenuated TMSV state[3] $\chi_{TMSV}^{(T_A,T_B)}(\beta_{B''}^*, \beta_{B''})$ in Eq. (5.22). The fidelity of a hybrid entangled state after teleportation can be calculated by applying Eq. (5.36) [13–15]

$$F_{tel} = \iint d^2\beta_D d^2\beta_{B''} \frac{1}{\pi^2} \chi_h(\beta_D, \beta_{B''}) \chi_h(-\beta_D, -\beta_{B''}) \chi_{TMSV}^{(T_A,T_B)}(-\beta_{B''}^*, -\beta_{B''}), \tag{5.43}$$

where, by applying Eqs. (2.38), (2.42), and (5.22), we have

$$\chi_{TMSV}^{(T_A,T_B)}(-\beta_{B''}^*, -\beta_{B''}) = \exp\left[-\sigma_{tel}|\beta_{B''}|^2\right], \tag{5.44}$$

with σ_{tel} defined in Eq. (3.10). When there is no loss ($T_A = T_B = 1$), we have $\sigma_{tel} = e^{-2r}$, [14] where r is again the initial squeezing. When the two channels are symmetric ($T_A = T_B = T$), we have $\sigma_{tel} = Te^{-2r} + (1 - T)$ as in Eq. (4.3). In order to calculate the fidelity, we perform a summation of integrations similar to that in Eqs. (5.40) and (5.41). In the following, I will calculate the fidelity for the cases when α_0 is large or small, respectively. For hybrid states with intermediate sizes, the detailed calculations can be found in appendix A.1.

Large cat state: When calculating the fidelity of the large hybrid state after teleportation, similar to Eqs. (5.38), (5.39), and (5.40), we obtain sixteen terms, which can be

[3]More generally, see [78] for how teleportation can operate under any types of CV teleportation channel.

simplified to four non-zero terms by applying the DV-mode symmetry, giving

$$\begin{aligned}
F_{tel}^{(large)} = \frac{1}{4}\Bigg[& \int d^2\beta_D \frac{1}{\pi}|X_{|+\rangle\langle+|}(\beta_D)|^2 \times \int d^2\beta_{B''}\frac{1}{\pi}|X_{|\alpha_0\rangle\langle\alpha_0|}(\beta_{B''})|^2 \chi_{TMSV}^{(T_A,T_B)}(-\beta_{B''}^*,-\beta_{B''}) \\
& + \int d^2\beta_D \frac{1}{\pi}|X_{|-\rangle\langle-|}(\beta_D)|^2 \times \int d^2\beta_{B''}\frac{1}{\pi}|X_{|-\alpha_0\rangle\langle-\alpha_0|}(\beta_{B''})|^2 \chi_{TMSV}^{(T_A,T_B)}(-\beta_{B''}^*,-\beta_{B''}) \\
& + \int d^2\beta_D \frac{1}{\pi}X_{|+\rangle\langle-|}(\beta_D)X_{|-\rangle\langle+|}(-\beta_D) \\
& \quad \times \int d^2\beta_{B''}\frac{1}{\pi}X_{|\alpha_0\rangle\langle-\alpha_0|}(\beta_{B''})X_{|-\alpha_0\rangle\langle\alpha_0|}(-\beta_{B''})\chi_{TMSV}^{(T_A,T_B)}(-\beta_{B''}^*,-\beta_{B''}) \\
& + \int d^2\beta_D \frac{1}{\pi}X_{|-\rangle\langle+|}(\beta_D)X_{|+\rangle\langle-|}(-\beta_D) \\
& \quad \times \int d^2\beta_{B''}\frac{1}{\pi}X_{|-\alpha_0\rangle\langle\alpha_0|}(\beta_{B''})X_{|\alpha_0\rangle\langle-\alpha_0|}(-\beta_{B''})\ \chi_{TMSV}^{(T_A,T_B)}(-\beta_{B''}^*,-\beta_{B''})\Bigg].
\end{aligned} \tag{5.45}$$

The integrations over mode D are still equal to unity. For the integrations over mode B'', after applying Eq. (5.44), we define the following four terms and calculate them using Mathematica

$$\begin{aligned}
f_{\pm\pm\alpha_0} &= \int d^2\beta_{B''}\frac{1}{\pi}|X_{|\pm\alpha_0\rangle\langle\pm\alpha_0|}(\beta_{B''})|^2 e^{-\sigma_{tel}|\beta_{B''}|^2} \\
&= \int d^2\beta_{B''}\frac{1}{\pi}e^{-|\beta|^2}e^{-\sigma_{tel}|\beta_{B''}|^2} \\
&= \frac{1}{1+\sigma_{tel}},
\end{aligned} \tag{5.46}$$

$$\begin{aligned}
f_{\pm\mp\alpha_0} &= \int d^2\beta_{B''}\frac{1}{\pi}X_{|\pm\alpha_0\rangle\langle\mp\alpha_0|}(\beta_{B''})X_{|\mp\alpha_0\rangle\langle\pm\alpha_0|}(-\beta_{B''})e^{-\sigma_{tel}|\beta_{B''}|^2} \\
&= \int d^2\beta_{B''}\frac{1}{\pi}e^{-|\beta_{B''}\pm 2\alpha_0|^2}e^{-\sigma_{tel}|\beta_{B''}|^2} \\
&= \frac{1}{1+\sigma_{tel}}\exp\left(-\frac{4\alpha_0^2\sigma_{tel}}{1+\sigma_{tel}}\right).
\end{aligned} \tag{5.47}$$

So the fidelity after teleportation is

$$F_{tel}^{(large)} = \frac{1}{4}(f_{++\alpha_0}+f_{--\alpha_0}+f_{+-\alpha_0}+f_{-+\alpha_0}) = \frac{1}{2(1+\sigma_{tel})}\left[1+\exp\left(-\frac{4\alpha_0^2\sigma_{tel}}{1+\sigma_{tel}}\right)\right]. \tag{5.48}$$

Small cat state: When calculating the fidelity of the small hybrid state after CV-mode teleportation, we arrive at sixteen different terms. Similar to Eq. (5.41), by applying the

DV-mode symmetry, twelve of these terms become zero, leaving the following four terms

$$
\begin{aligned}
F_{tel}^{(small)} = \frac{1}{4}\Big[& \int d^2\beta_D \frac{1}{\pi}|X_{|0\rangle\langle 0|}(\beta_D)|^2 \times \int d^2\beta_{B''}\frac{1}{\pi}|X_{|1\rangle\langle 1|}(\tilde{\beta}_{B''})|^2 \chi_{TMSV}^{(T_A,T_B)}(-\beta_{B''}^*,-\beta_{B''}) \\
& + \int d^2\beta_D \frac{1}{\pi}|X_{|1\rangle\langle 1|}(\beta_D)|^2 \times \int d^2\beta_{B''}\frac{1}{\pi}|X_{|0\rangle\langle 0|}(\tilde{\beta}_{B''})|^2 \chi_{TMSV}^{(T_A,T_B)}(-\beta_{B''}^*,-\beta_{B''}) \\
& + \int d^2\beta_D \frac{1}{\pi}X_{|0\rangle\langle 1|}(\beta_D)X_{|1\rangle\langle 0|}(-\beta_D) \\
& \quad \times \int d^2\beta_{B''}\frac{1}{\pi}X_{|1\rangle\langle 0|}(\tilde{\beta}_{B''})X_{|0\rangle\langle 1|}(-\tilde{\beta}_{B''})\chi_{TMSV}^{(T_A,T_B)}(-\beta_{B''}^*,-\beta_{B''}) \\
& + \int d^2\beta_D \frac{1}{\pi}X_{|1\rangle\langle 0|}(\beta_D)X_{|0\rangle\langle 1|}(-\beta_D) \\
& \quad \times \int d^2\beta_{B''}\frac{1}{\pi}X_{|0\rangle\langle 1|}(\tilde{\beta}_{B''})X_{|1\rangle\langle 0|}(-\tilde{\beta}_{B''})\ \chi_{TMSV}^{(T_A,T_B)}(-\beta_{B''}^*,-\beta_{B''})\Big]. \quad (5.49)
\end{aligned}
$$

The integrations over mode D still give unity, for the integrations over mode B'', we apply Eq. (5.44) and define

$$
\begin{aligned}
f_{00} &= \int d^2\beta_{B''}\frac{1}{\pi}|X_{|0\rangle\langle 0|}(\tilde{\beta}_{B''})|^2 e^{-\sigma_{tel}|\beta_{B''}|^2} \\
&= \frac{1}{\sqrt{\tau}}, \\
f_{11} &= \int d^2\beta_{B''}\frac{1}{\pi}|X_{|1\rangle\langle 1|}(\tilde{\beta}_{B''})|^2 e^{-\sigma_{tel}|\beta_{B''}|^2} \\
&= \frac{2+{\sigma_{tel}}^2+2{\sigma_{tel}}^4+4\sigma_{tel}(1+{\sigma_{tel}}^2)\cosh(2s)+3{\sigma_{tel}}^2\cosh(4s)}{2\sqrt{e^{-2s}+\sigma_{tel}}(e^{2s}+\sigma_{tel})^{5/2}(e^{-2s}+\sigma_{tel})^2}, \\
f_{10} &= \int d^2\beta_{B''}\frac{1}{\pi}X_{|1\rangle\langle 0|}(\tilde{\beta}_{B''})X_{|0\rangle\langle 1|}(\tilde{\beta}_{B''})e^{-\sigma_{tel}|\beta_{B''}|^2} \\
&= \frac{1+\sigma_{tel}\cosh(2s)}{\tau^{3/2}}, \\
f_{01} &= \int d^2\beta_{B''}\frac{1}{\pi}X_{|0\rangle\langle 1|}(\tilde{\beta}_{B''})X_{|1\rangle\langle 0|}(-\tilde{\beta}_{B''})e^{-\sigma_{tel}|\beta_{B''}|^2} \\
&= f_{10}, \quad (5.50)
\end{aligned}
$$

where $\tau = 1+{\sigma_{tel}}^2+2\sigma_{tel}\cosh(2s)$, with s being the single-mode squeezing parameter in Eq. (5.9). The final fidelity of hybrid entanglement after teleportation is given by

$$
F_{tel}^{(small)} = \frac{1}{4}\left(f_{00}+f_{11}+f_{10}+f_{01}\right), \quad (5.51)
$$

which tends to unity as the channel loss approaches zero ($T_A = T_B \to 1$). The detailed simulation results are presented in the next section.

5.5 Results

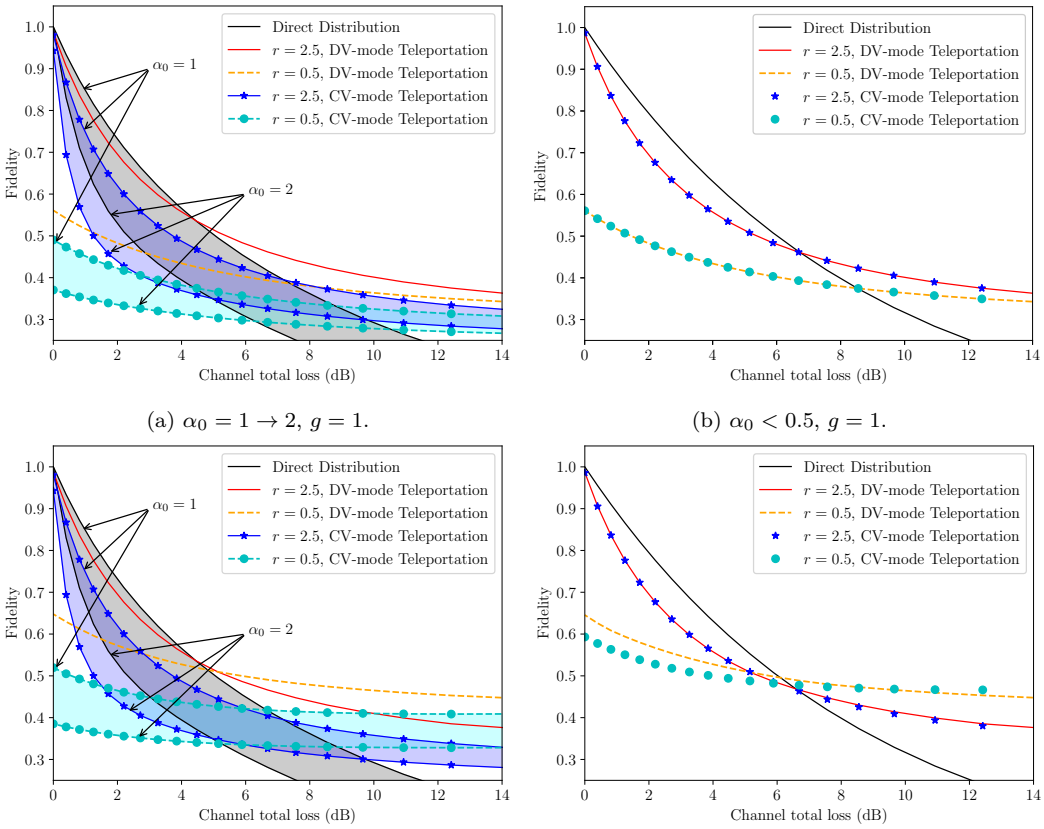

(a) $\alpha_0 = 1 \to 2$, $g = 1$.

(b) $\alpha_0 < 0.5$, $g = 1$.

(c) $\alpha_0 = 1 \to 2$, g is optimized.

(d) $\alpha_0 < 0.5$, g is optimized.

Figure 5.2: The fidelity is plotted for direct distribution (black), or teleportation of the the DV/CV mode (red-orange/blue-navy). The channels are assumed to be symmetric ($T_A = T_B$), while the initial two-mode squeezing parameter r is set to either 2.5 or 0.5, and the teleportation gain is set to $g = 1$. In general, the fidelity of DV-mode teleportation stays the same regardless of α_0. (a,c) For $\alpha_0 = 1 \to 2$, the fidelities of direct distribution and CV-mode teleportation vary in the shaded ranges, with the upper bound corresponding to $\alpha_0 = 1$, and the lower bound corresponding to $\alpha_0 = 2$. (b,d) For $\alpha_0 < 0.5$, the fidelities of the three schemes stay approximately unchanged, providing an upper bound for the fidelity with respect to α_0. Note that in (a,b), the teleportation gain g is unity, while in (c,d), the gain is optimized. Gain-tuning only improves the fidelity for the case of $r = 0.5$. (Taken from [51].)

In this section, I aim to compare the long-distance distribution of hybrid entanglement using two different schemes: one scheme (in Fig. 5.1a) uses the direct distribution from the satellite, with one terrestrial node receiving the DV mode and the other node the CV mode; and one scheme (in Fig. 5.1b) uses the TMSV channel created by the satellite to teleport one mode of an initially localised hybrid state from one terrestrial node to another. I compare the two schemes in terms of the fidelity and logarithmic negativity.

I simulate the hybrid entangled state in Eq. (5.2) with different real values of α_0,[4] especially in the cases of small cat states ($\alpha_0 < 0.5$) and large cat states ($\alpha_0 > 1$). For DV-mode teleportation, when calculating the summation in Eq. (5.19), we stop at a value of $k = k_{max}$. Since the averaged photon number is given by α_0^2, we see that k_{max} should be at least α_0^2 [79]. Practically, to find k_{max}, I start with a high value, then slowly reduce k_{max} while checking that $\mathrm{Tr}\left(|cat_{\pm}\rangle\langle cat_{\pm}|\right) = 1 \pm \delta$, where δ is the tolerance. In the following simulations, I use the values of $\delta = 10^{-14}$ and $k_{max} \approx 30$.

In my first simulation, I assume that the two down-link channels are symmetric, i.e., $T_A = T_B = T$. The total loss of two channels can be calculated by $-10\log_{10}(T^2)$ (dB). The teleportation gain is set to $g = 1$, which is the optimal gain when $T_A = T_B$ [4, 31]. The fidelity is calculated by Eqs. (5.17), (2.80), (5.19), (5.48), and (5.51). Fig. 5.2c shows the case of large cat states where I selectively adopted values of α_0 in the range of $\alpha_0 = 1 \to 2$. I first vary the initial squeezing r of the TMSV channel and find that the fidelity of teleportation increases as r increases, then saturates to its maximum value when $r \approx 2.5$, which I will refer to as the optimal squeezing parameter. Thus, in this figure, I plot the fidelity for $r = 2.5$ and a lower value of $r = 0.5$. I found that, for higher loss, the effect of the initial squeezing r on teleportation results becomes less significant. This implies that for long-distance communications, we need not spend too much experimental resources on enhancing the channel squeezing.

We can also see from Fig. 5.2c that the fidelity of DV-mode teleportation stays the same regardless of α_0, while the fidelities of CV-mode teleportation and direct distribution decrease when α_0 increases. In particular, for $r = 2.5$, my simulation shows that when $\alpha_0 > 1.2$, the fidelity of DV-mode teleportation is always higher than direct distribution, and the difference further increases with increasing α_0 and higher channel loss. When α_0 decreases below 1.2, the fidelity of direct distribution starts to become higher than DV-mode teleportation at low channel loss. However, as the loss increases, the fidelity of

[4] The same simulation was run with complex values of α_0 as well. However, for both direct distribution and DV-mode teleportation, I found that the fidelity is the highest when the initial cat states are small and real.

direct distribution quickly decreases, while the fidelity of DV-mode teleportation decreases slower then saturates to a higher value. The loss level where the crossover occurs (which I will henceforth refer to as the 'crossover loss') increases as α_0 decreases, and varies from 0 dB go 5 dB when α_0 varies from 1.2 to 1. This crossover can be explained by how the channel loss enters the calculations of the direct distribution scheme (via both DV and CV loss components) as compared to the teleportation channel (via two CV loss components). Ultimately, my detailed mathematical models offer the explanation of these findings.

In addition, in Fig. 5.2c, under all loss conditions, teleporting the DV mode of the hybrid entangled state is always better or equal to teleporting the CV mode. The difference becomes more significant when α_0 increases. My results can be explained by the notion that for a given squeezing level and a given loss level in the CV teleportation channel, the teleportation of larger Fock states will provide for less fidelity than smaller Fock states. Only in the limit of zero loss would this not be the case. As such, superpositions of Fock states weighted to excitations of small photon numbers should be 'easier' to teleport. The DV state can be considered loosely as such a superposition of Fock states.

Fig. 5.2d shows the case of small cat states where I selectively simulated $\alpha_0 = 0.1 \rightarrow 0.5$. In this case, we can see that the fidelities of the three schemes all remain almost unchanged, and the difference cannot be seen from the curves in the plot. For losses below 7dB, we can also see that direct distribution gives a higher fidelity than teleportation. However, when the loss increases above 7dB, teleportation is always better. In addition, for all loss conditions, I find that it does not matter to teleport either the DV or CV mode of hybrid entanglement, since the output fidelity is the same. This symmetry can be explained by the fact that when $\alpha_0 < 0.5$, Eq. (5.9) gives $s < 0.1$, so that the SMSV and 1PS states in Eq. (5.8) are very lightly squeezed. Intuitively, we can understand that when the cat states become small, their average photon numbers approach either 0 or 1. As a result, the cat states approach $|0\rangle$ and $|1\rangle$, and the approximated hybrid entangled state in Eq. (5.10) approaches a DV entangled state, which is spatially symmetric. In general, we can see that lower photon-number states, especially qubit states, are less sensitive to channel loss. Thus, the case of small α_0 provides the upper bounds for the fidelities of the three schemes.

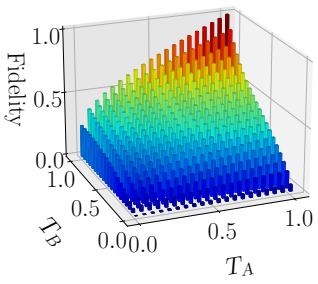

(a) Direct Distribution

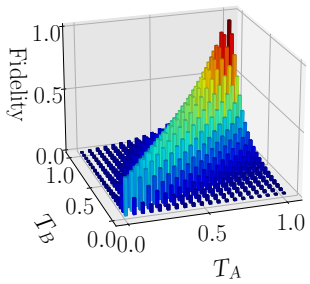

(b) DV-mode Teleportation, $g = 1$

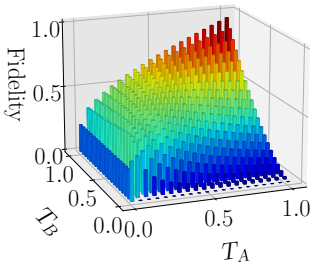

(c) DV-mode Teleportation, $g = \sqrt{\frac{T_B}{T_A}}$

Figure 5.3: The fidelities of direct distribution (a) and DV-mode teleportation (b,c) is plotted where T_A and T_B are independently varied. I fixed $\alpha_0 = 1.5$, $r = 2.5$, and $g = 1$ (b) or $g = \sqrt{T_B/T_A}$ (c). (Taken from [51].)

For cat states of intermediate sizes where $0.5 < \alpha_0 < 1$, my simulations show that the fidelity of DV-mode teleportation still stays unchanged, while the fidelities of direct distribution and CV-mode teleportation decrease monotonically as α_0 increases. For this intermediate range, the fidelities naturally stay in between the bounds set by large and small α_0.

Next, I investigate the effect of teleportation gain-tuning by varying g in order to find the maximal fidelity. The results are plotted in Fig. 2c and Fig. 2d. As can be seen, when $r = 2.5$, for all loss conditions below 15dB, the optimal gain g is approximately 1, and tuning the gain further does not improve the fidelity. However, when $r = 0.5$, gain-tuning

improves the fidelity of both DV and CV teleportation. Please note that for high loss conditions, the fidelity of DV-mode teleportation (or CV-mode teleportation with small α_0) can be brought above 0.5 by maintaining a low initial squeezing while optimizing the teleportation gain.

To study asymmetric channels, I next vary T_A and T_B independently, while plotting the 3D map for the fidelity. Since large cat states are more useful for quantum computations, in this simulation, I fix $\alpha_0 = 1.5$ and $r = 2.5$, respectively. Since my simulations have shown that DV-mode is always preferable over CV-mode teleportation, especially for large α_0, I will only plot the fidelity for direct distribution and DV-mode teleportation. From the plot of direct distribution (Fig. 5.3a), we see that the fidelity decreases monotonically with T_A and T_B. Especially, the fidelity decreases faster with the loss in the CV mode (mode B). For DV-mode teleportation, in order to study the effect of gain-tuning, I set the gain to either $g = 1$ or $g = \sqrt{T_B/T_A}$.[(5)] As can be seen in Fig. 5.3b, when $g = 1$, the output attains the highest level of entanglement when the channels are symmetric $T_A = T_B$, but quickly drops to near zero when $T_A \neq T_B$. In Fig. 5.3c, we can see that tuning the teleportation gain to $g = \sqrt{T_B/T_A}$ significantly improves the fidelity for asymmetric channels [31]. During gain tuning, it is especially important to maintain a high transmissivity in Bob's down-link channel, since when T_B is high, the fidelity remains reasonably high for all different values of T_A.

In the next simulation, I use the same parameters as the previous one, but I plot the logarithmic negativity using Eq. (2.76). From the results in Fig. 5.4, we see that the logarithmic negativity follows the same trend as the fidelity, however, the former decreases more sharply with low transmissivities and channel asymmetry as compared to the latter. We also see that tuning the gain to the optimal value of $g = \sqrt{T_B/T_A}$ significantly improves the quality of the teleportation outcomes.

I also perform a series of similar simulations where the initial hybrid entangled cat state

[(5)] This g value was previously found to be optimal with regard to logarithmic negativity (see section 5.4.1 and [31]).

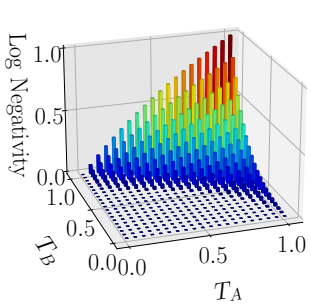

(a) Direct Distribution

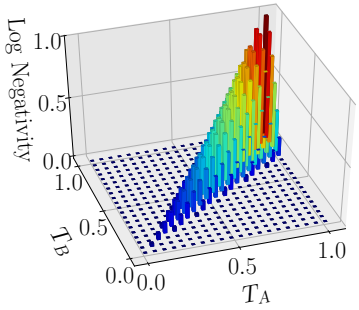

(b) DV-mode Teleportation, $g = 1$

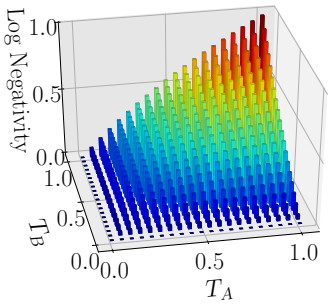

(c) DV-mode Teleportation, $g = \sqrt{\frac{T_B}{T_A}}$

Figure 5.4: The logarithmic negativity of direct distribution (a) and DV-mode teleportation (b,c) with $\alpha_0 = 1.5$, $r = 2.5$, and $g = 1$ (b) or $\sqrt{\frac{T_B}{T_A}}$ (c). (Taken from [51].)

in Eq. (5.1) is replaced by a hybrid coherent state of the form [80, 81]

$$(|\alpha_0\rangle_C|0\rangle_D + |-\alpha_0\rangle_C|1\rangle_D)/\sqrt{2}. \tag{5.52}$$

I find that for large α_0, all my conclusions found for the cat hybrid state remain intact. Indeed, the detailed results show trends for both direct and teleported states very similar to those shown in Fig. 5.2c. For small α_0, clear differences in both the direct and teleported states can be identified relative to Fig. 5.2d. However, again I emphasize that the large α_0 states are the states of interest for almost all hybrid DV-CV quantum protocols. States beyond large cat states remain worthy of study, particularly in regard to upper bounds on the teleported fidelities.

5.6 Conclusion

Hybrid technologies play an important role in interfacing mixed quantum protocols, which will in turn help accelerate the global development of quantum networks. In this chapter, I studied, for the first time, the teleportation of either mode of a hybrid entangled state via a lossy TMSV channel, and compared such teleportation to the case where the hybrid entanglement is generated on board a satellite and directly distributed to Earth. Due to the complexity of the hybrid entangled state, especially in the cross-diagonal matrices with multi-photon numbers, I resorted to the characteristic function formalism. By identifying symmetries within this formalism, I then developed a novel mathematical framework to calculate the fidelity of the teleported hybrid state. Our results showed that when the initial cat states have $\alpha_0 > 1.2$, it was always preferable to teleport the DV mode of the hybrid entangled state. For cat states with $\alpha_0 < 1.2$, direct distribution gave a higher fidelity than teleportation at low channel loss. However, for losses higher than 7dB, the teleportation of the DV mode was always better, regardless of α_0. Please note, losses above 7dB are expected for satellite-to-Earth channels for transceiver apertures of reasonable sizes. For all loss conditions, I found CV-mode teleportation always gave a fidelity that is less than or equal to DV-mode teleportation, where the equality happens when the cat states become small ($\alpha_0 < 0.5$). Similar results to the above were found for a hybrid state in which the cat states were replaced by large coherent states of opposite phases. Our results will be important for next-generation heterogeneous quantum communication networks, whose teleportation resource is sustained by standard TMSV entanglement distribution from LEO satellites.

Chapter 6

Conclusion

Hybrid teleportation protocols provide the interface between DV and CV technologies, helping to interconnect different elements of the future quantum network. Such a hybrid protocol has the combined benefits of pure DV and CV teleportation: it yields an enhanced success rate while, at the same time, preserving the fidelity of the teleported state. For long-distance communication, the teleportation channel can be pre-distributed by a satellite from LEO to two far-apart ground stations, thus expanding the quantum network to the global scale. In this thesis, I study in detail the CV teleportation channel based on the TMSV state, taking into account, for the first time, the transmission loss typical for long-distance communication.

In past studies, the CV teleportation channel has previously been studied in conditions where there is no transmission loss. In Chapter 2, I studied the effect of channel loss on such a protocol. I derived for the first time the mathematical model for the attenuated CV teleportation channel and calculated the output after teleporting an arbitrary input mode. Specifically, I studied the case where the input mode is part of a DV entangled state in the photon-number basis. By simulating a wide range of different teleportation parameters, I showed the conditions where the teleported DV entangled state can achieve higher entanglement quality as compared to direct distribution from the satellite. To further compare the teleported and directly-distributed DV entangled state, I applied

them to a QKD protocol and compare the resulting key rates.

In Chapter 3, I applied the mathematical model from the previous chapter to teleport a Schrödinger's cat state. Past studies have shown that CV teleportation can preserve the quantum character of the cat state. In this chapter, I take into consideration the effect of channel transmission loss and found that the quantum character is lost after 5dB of fix-attenuation. In addition, I investigate the free-space channel from a satellite in LEO down to Earth, with about 500km in height and 30dB of loss. In such a channel, the transmissivity varies probabilistically following the atmospheric turbulence at around 100km above the Earth's surface. By using two different mathematical models for the probability distribution - the beam-wandering model and the elliptic model, I find that the free-space channel can preserve a higher level of fidelity than the fixed-attenuation channel of the same averaged loss.

In chapter 4, I studied for the first time the teleportation of a hybrid entangled state over a lossy CV teleportation channel. For the typical average loss of the satellite-to-Earth channel, my detailed calculations show that teleporting the DV mode of the hybrid entanglement is always better than teleporting the CV mode or directly distributing both modes from the satellite.

Appendix A

Supplementary Materials for Satellite-based Distribution of Hybrid Entanglement

A.1 CV-mode teleportation of an exact hybrid entangled state

This appendix uses the exact mathematical form of the hybrid entangled state (Eq. (5.2)) to calculate the characteristic function and fidelity after CV-mode teleportation. The mathematical model below is especially useful for hybrid states with intermediate sizes ($0.5 < \alpha_0 < 1$), where a simple approximation does not exist.

The characteristic function of the exact hybrid entangled state is found by substituting

Eq. (5.2) into Eqs. (2.37) and (5.23), giving

$$\chi_h^{(exact)}(\beta_D,\beta_C) = \frac{1}{2}\Big[X_{|0\rangle\langle 0|}(\beta_D)X_{|cat_-\rangle\langle cat_-|}(\beta_C) + X_{|1\rangle\langle 1|}(\beta_D)X_{|cat_+\rangle\langle cat_+|}(\beta_C) + X_{|0\rangle\langle 1|}(\beta_D)X_{|cat_-\rangle\langle cat_+|}(\beta_C) + X_{|1\rangle\langle 0|}(\beta_D)X_{|cat_+\rangle\langle cat_-|}(\beta_C)\Big]. \tag{A.1}$$

To find the fidelity after teleporting the CV mode, we follow the calculations in section 5.4.3, giving

$$\begin{aligned} F_{tel}^{(exact)} = \frac{1}{4}\Big[& \int d^2\beta_D \frac{1}{\pi}|X_{|0\rangle\langle 0|}(\beta_D)|^2 \times \int d^2\beta_{B''}\frac{1}{\pi}|X_{|cat_-\rangle\langle cat_-|}(\beta_{B''})|^2 \chi_{TMSV}^{(T_A,T_B)}(-\beta_{B''}^*,-\beta_{B''}) \\ & + \int d^2\beta_D \frac{1}{\pi}|X_{|1\rangle\langle 1|}(\beta_D)|^2 \times \int d^2\beta_{B''}\frac{1}{\pi}|X_{|cat_+\rangle\langle cat_+|}(\beta_{B''})|^2 \chi_{TMSV}^{(T_A,T_B)}(-\beta_{B''}^*,-\beta_{B''}) \\ & + \int d^2\beta_D \frac{1}{\pi}X_{|1\rangle\langle 0|}(\beta_D)X_{|0\rangle\langle 1|}(-\beta_D) \\ & \quad \times \int d^2\beta_{B''}\frac{1}{\pi}X_{|cat_+\rangle\langle cat_-|}(\beta_{B''})X_{|cat_-\rangle\langle cat_+|}(-\beta_{B''})\chi_{TMSV}^{(T_A,T_B)}(-\beta_{B''}^*,-\beta_{B''}) \\ & + \int d^2\beta_D \frac{1}{\pi}X_{|0\rangle\langle 1|}(\beta_D)X_{|1\rangle\langle 0|}(-\beta_D) \\ & \quad \times \int d^2\beta_{B''}\frac{1}{\pi}X_{|cat_-\rangle\langle cat_+|}(\beta_{B''})X_{|cat_+\rangle\langle cat_-|}(-\beta_{B''})\ \chi_{TMSV}^{(T_A,T_B)}(-\beta_{B''}^*,-\beta_{B''})\Big]. \end{aligned} \tag{A.2}$$

The integrations over mode D are still giving unity, for the integrations in mode B'', after applying Eq. (5.44), the exact fidelity can be given by

$$F_{tel}^{(exact)} = \frac{1}{4}(f_{++cat} + f_{--cat} + f_{+-cat} + f_{-+cat}), \tag{A.3}$$

where

$$\begin{aligned} f_{++cat} &= \int d^2\beta_{B''}\frac{1}{\pi}X_{|cat_+\rangle\langle cat_+|}(\beta_{B''})X_{|cat_+\rangle\langle cat_+|}(-\beta_{B''})e^{-\sigma|\beta_{B''}|^2}, \\ f_{--cat} &= \int d^2\beta_{B''}\frac{1}{\pi}X_{|cat_-\rangle\langle cat_-|}(\beta_{B''})X_{|cat_-\rangle\langle cat_-|}(-\beta_{B''})e^{-\sigma|\beta_{B''}|^2}, \\ f_{+-cat} &= \int d^2\beta_{B''}\frac{1}{\pi}X_{|cat_+\rangle\langle cat_-|}(\beta_{B''})X_{|cat_-\rangle\langle cat_+|}(-\beta_{B''})e^{-\sigma|\beta_{B''}|^2}, \\ f_{-+cat} &= \int d^2\beta_{B''}\frac{1}{\pi}X_{|cat_-\rangle\langle cat_+|}(\beta_{B''})X_{|cat_+\rangle\langle cat_-|}(-\beta_{B''})e^{-\sigma|\beta_{B''}|^2}. \end{aligned} \tag{A.4}$$

In order to calculate the above integrations, we first apply Eq. (2.4) to find

$$
\begin{aligned}
X_{|cat_+\rangle\langle cat_+|}(\beta) &= \frac{1}{N_+^2}(X_{|\alpha_0\rangle\langle\alpha_0|} + X_{|-\alpha_0\rangle\langle-\alpha_0|} + X_{|\alpha_0\rangle\langle-\alpha_0|} + X_{|-\alpha_0\rangle\langle\alpha_0|}),\\
X_{|cat_-\rangle\langle cat_-|}(\beta) &= \frac{1}{N_-^2}(X_{|\alpha_0\rangle\langle\alpha_0|} + X_{|-\alpha_0\rangle\langle-\alpha_0|} - X_{|\alpha_0\rangle\langle-\alpha_0|} - X_{|-\alpha_0\rangle\langle\alpha_0|}),\\
X_{|cat_+\rangle\langle cat_-|}(\beta) &= \frac{1}{N_+N_-}(X_{|\alpha_0\rangle\langle\alpha_0|} - X_{|-\alpha_0\rangle\langle-\alpha_0|} - X_{|\alpha_0\rangle\langle-\alpha_0|} + X_{|-\alpha_0\rangle\langle\alpha_0|}),\\
X_{|cat_-\rangle\langle cat_+|}(\beta) &= \frac{1}{N_+N_-}(X_{|\alpha_0\rangle\langle\alpha_0|} - X_{|-\alpha_0\rangle\langle-\alpha_0|} + X_{|\alpha_0\rangle\langle-\alpha_0|} - X_{|-\alpha_0\rangle\langle\alpha_0|}).
\end{aligned}
\tag{A.5}
$$

We then define the following integrations

$$
f_{jlmn} = \int d^2\beta_{B''}\frac{1}{\pi}X_{|j\alpha_0\rangle\langle l\alpha_0|}(\beta_{B''})X_{|m\alpha_0\rangle\langle n\alpha_0|}(-\beta_{B''})e^{-\sigma|\beta_{B''}|^2},
\tag{A.6}
$$

where $j,l,m,n \in \{+,-\}$. By substituting Eq. (5.28) into the above equation and using Mathematica to calculate, we find

$$
\begin{aligned}
f_0 &= f_{\pm\pm\pm\pm} = \frac{1}{1+\sigma},\\
f_1 &= f_{\pm\mp\mp\pm} = \frac{1}{1+\sigma}\exp\left(-\alpha_0\frac{4\sigma}{1+\sigma}\right),\\
f_2 &= f_{\pm\pm\mp\mp} = \frac{1}{1+\sigma}\exp\left(-\alpha_0\frac{4}{1+\sigma}\right),\\
f_3 &= f_{\pm\mp\pm\mp} = \frac{1}{1+\sigma}\exp\left(-4\alpha_0\right),\\
f_4 &= f_{\pm\pm\pm\mp} = f_{\mp\mp\pm\mp} = f_{\pm\mp\pm\pm} = f_{\pm\mp\mp\mp} = \frac{1}{1+\sigma}\exp\left(-2\alpha_0\right).
\end{aligned}
\tag{A.7}
$$

We can then find that

$$
\begin{aligned}
f_{++cat} &= \frac{2}{N_+^4}(f_0 + f_1 + f_2 + f_3 + 4f_4),\\
f_{--cat} &= \frac{2}{N_-^4}(f_0 + f_1 + f_2 + f_3 - 4f_4),\\
f_{+-cat} &= f_{-+cat} = \frac{2}{N_+^2N_-^2}(f_0 + f_1 - f_2 - f_3).
\end{aligned}
\tag{A.8}
$$

From Eqs. (A.3), (A.7), and (A.8), we can find the exact fidelity of CV-mode teleportation. From my simulation, I can find that for cat states with intermediate sizes ($0.5 < \alpha_0 < 1$), the fidelity stays between that of large and small cat states, and decreases monotonically as α_0 increases.

A.2 Direct distribution over a lossy channel

This section derives the attenuated hybrid entangled state after the direct distribution in Fig. 5.1a and section 5.3. The original hybrid entangled state in Eq. (5.1), together with two auxiliary vacuum modes, can be written together as the four-mode state

$$|\psi_{A\epsilon_A B\epsilon_B}\rangle = \frac{1}{\sqrt{2}}\left\{\frac{|\alpha_0\rangle_A - |-\alpha_0\rangle_A}{N_-}|0\rangle_{\epsilon_A}\otimes|0\rangle_B|0\rangle_{\epsilon_B} + \frac{|\alpha_0\rangle_A + |-\alpha_0\rangle_A}{N_+}|0\rangle_{\epsilon_A}\otimes\hat{a}_B^\dagger|0\rangle_B|0\rangle\epsilon_B\right\}, \tag{A.9}$$

where $N_\pm$ is given in Eq. (2.5). The two lossy down-link channels are modeled by two beam splitters. Let $t_l = \sqrt{T_l}$ and $r_l = \sqrt{1-T_l}$ with $l \in \{A, B\}$, after the two beam splitter transformations in Eqs. (5.12) and (5.13), the state becomes

$$\begin{aligned}|\psi_{A'\epsilon_{A'}B'\epsilon_{B'}}\rangle = \frac{1}{\sqrt{2}}\Bigg\{&\frac{|t_A\alpha_0\rangle_{A'}|r_A\alpha_0\rangle_{\epsilon_{A'}} - |-t_A\alpha_0\rangle_{A'}|-r_A\alpha_0\rangle_{\epsilon_{A'}}}{N_-}\otimes|0\rangle_{B'}|0\rangle_{\epsilon_{B'}}\\ &+\frac{|t_A\alpha_0\rangle_{A'}|r_A\alpha_0\rangle_{\epsilon_{A'}} + |-t_A\alpha_0\rangle_{A'}|-r_A\alpha_0\rangle_{\epsilon_{A'}}}{N_+}\\ &\otimes\left(t_B|1\rangle_{B'}|0\rangle\epsilon_{B'} + r_B|0\rangle_{B'}|1\rangle_{\epsilon_{B'}}\right)\Bigg\}.\end{aligned} \tag{A.10}$$

The corresponding density matrix can be written as

$$\begin{aligned}\rho_{A'\epsilon_{A'}B'\epsilon_{B'}} = \frac{1}{2}\Bigg\{&|1\rangle_{\epsilon_{B'}}\langle 1|\otimes\left[\frac{r_B^2}{N_+^2}|0\rangle_{B'}\langle 0|\otimes(\rho_{++}+\rho_{--}+\rho_{-+}+\rho_{+-})\right]\\ &+|0\rangle_{\epsilon_{B'}}\langle 0|\otimes\Bigg[\frac{t_B^2}{N_+^2}|1\rangle_{B'}\langle 1|\otimes(\rho_{++}+\rho_{--}+\rho_{-+}+\rho_{+-})\\ &\quad+\frac{1}{N_-^2}\ |0\rangle_{B'}\langle 0|\otimes(\rho_{++}+\rho_{--}-\rho_{-+}-\rho_{+-})\\ &\quad+\frac{t_B}{N_+N_-}|0\rangle_{B'}\langle 1|\otimes(\rho_{++}-\rho_{--}+\rho_{-+}-\rho_{+-})\\ &\quad+\frac{t_B}{N_+N_-}|1\rangle_{B'}\langle 0|\otimes(\rho_{++}-\rho_{--}-\rho_{-+}+\rho_{+-})\Bigg]\\ &+|0\rangle_{\epsilon_{B'}}\langle 1|\otimes(\cdots)+|1\rangle_{\epsilon_{B'}}\langle 0|\otimes(\cdots)\Bigg\},\end{aligned} \tag{A.11}$$

where

$$\begin{aligned}\rho_{\pm\pm} &= |\pm t_A\alpha_0\rangle_{A'}\langle\pm t_A\alpha_0|\otimes|\pm r_A\alpha_0\rangle_{\epsilon_{A'}}\langle\pm r_A\alpha_0|,\\ \rho_{\pm\mp} &= |\pm t_A\alpha_0\rangle_{A'}\langle\mp t_A\alpha_0|\otimes|\pm r_A\alpha_0\rangle_{\epsilon_{A'}}\langle\mp r_A\alpha_0|.\end{aligned} \tag{A.12}$$

The states indicated by the triple dots are not important, because when tracing out the auxiliary mode $\epsilon_{B'}$ from the state $\rho_{A'\epsilon_{A'}B'\epsilon_{B'}}$, the terms with $|0\rangle_{\epsilon_{B'}}\langle 1|$ and $|1\rangle_{\epsilon_{B'}}\langle 0|$ are removed. The tracing of $\epsilon_{B'}$ also equates $|1\rangle_{\epsilon_{B'}}\langle 1|$ and $|0\rangle_{\epsilon_{B'}}\langle 0|$ to unity. The tracing of $\epsilon_{A'}$ can be done by applying the integrations in Eq. (5.16), which transforms $\rho_{\pm\pm}$ and $\rho_{\pm\mp}$ to

$$\begin{aligned}\rho'_{\pm\pm} &= |\pm t_A\alpha_0\rangle_{A'}\langle\pm t_A\alpha_0|,\\ \rho'_{\pm\mp} &= |\pm t_A\alpha_0\rangle_{A'}\langle\mp t_A\alpha_0|e^{-2r_A^2\alpha_0^2},\end{aligned} \tag{A.13}$$

respectively. After tracing out $\epsilon_{A'}$ and $\epsilon_{B'}$, we can find the two-mode directly distributed state

$$\begin{aligned}\rho_{A'B'} = \mathrm{Tr}_{\epsilon_{A'}\epsilon_{B'}}\left[\rho_{A'\epsilon_{A'}B'\epsilon_{B'}}\right] =& \frac{1}{2}\left\{\frac{r_B^2}{N_+^2}\,|0\rangle_{B'}\langle 0|\otimes(\rho'_{++}+\rho'_{--}+\rho'_{-+}+\rho'_{+-})\right.\\ &+\frac{t_B^2}{N_+^2}\,|1\rangle_{B'}\langle 1|\otimes(\rho'_{++}+\rho'_{--}+\rho'_{-+}+\rho'_{+-})\\ &+\frac{1}{N_-^2}\,|0\rangle_{B'}\langle 0|\otimes(\rho'_{++}+\rho'_{--}-\rho'_{-+}-\rho'_{+-})\\ &+\frac{t_B}{N_+N_-}|0\rangle_{B'}\langle 1|\otimes(\rho'_{++}-\rho'_{--}+\rho'_{-+}-\rho'_{+-})\\ &\left.+\frac{t_B}{N_+N_-}|1\rangle_{B'}\langle 0|\otimes(\rho'_{++}-\rho'_{--}-\rho'_{-+}+\rho'_{+-})\right\}.\end{aligned} \tag{A.14}$$

By rearranging the terms, we come to the directly-distributed state given by Eq. (5.17).

References

[1] S. Barnett and P. M. Radmore, *Methods in theoretical quantum optics.* Oxford, UK: Clarendon Press, 2002.

[2] G. S. Agarwal, *Quantum optics.* Cambridge, UK: Cambridge University Press, 2013.

[3] S. L. Braunstein and P. van Loock, "Quantum information with continuous variables," *Review Modern Physics*, vol. 77, p. 513, 2005.

[4] S. Takeda, T. Mizuta, M. Fuwa, H. Yonezawa, P. van Loock, and A. Furusawa, "Gain tuning for continuous–variable quantum teleportation of discrete–variable states," *Physical Review A*, vol. 88, p. 042327, 2013.

[5] P. van Loock, T. D. Ladd, K. Sanaka, F. Yamaguchi, K. Nemoto, W. J. Munro, and Y. Yamamoto, "Hybrid quantum repeater using bright coherent light," *Physical Review Letters*, vol. 96, p. 240501, 2006.

[6] C. C. Gerry, "Generation of optical macroscopic quantum superposition states via state reduction with a Mach–Zehnder interferometer containing a Kerr medium," *Physical Review A*, vol. 59, p. 4095, 1999.

[7] H. Jeong, "Using weak nonlinearity under decoherence for macroscopic entanglement generation and quantum computation," *Physical Review A*, vol. 72, p. 034305, 2005.

[8] O. Morin, K. Huang, J. Liu, H. Le Jeannic, C. Fabre, and J. Laurat, "Remote creation of hybrid entanglement between particle–like and wave–like optical qubits," *Nature Photonics*, vol. 8, p. 570, 2014.

[9] D. Sychev, A. Ulanov, A. Pushkina, E. Tiunov, V. Novikov, and A. Lvovsky, "Entanglement and teleportation between polarization and wave–like encodings of an optical qubit," *Nature Communications*, vol. 9, p. 3672, 2018.

[10] K. Huang, H. Le Jeannic, O. Morin, T. Darras, G. Guccione, A. Cavaillès, and J. Laurat, "Engineering optical hybrid entanglement between discrete– and continuous–variable states," *New Journal of Physics*, vol. 21, no. 8, p. 083033, 2019.

[11] E. Knill, R. Laflamme, and G. Milburn, "A scheme for efficient quantum computation with linear optics," *Nature*, vol. 409, p. 46, 2001.

[12] E. Tiunov, D. Sychev, A. Ulanov, A. Pushkina, I. Surov, V. Novikov, and A. Lvovsky, "Towards interconversion between discrete– and continuous–variable encodings in quantum optics," vol. 1936, 2018, p. 020017.

[13] L. A. Farias, "Continuous variable teleportation with non–Gaussian resources in the characteristic function representation," Ph.D. dissertation, University Degli Studi Di Salerno, 2009. [Online]. Available: https://arxiv.org/abs/0903.5406

[14] K. P. Seshadreesan, J. P. Dowling, and G. S. Agarwal, "Non–Gaussian entangled states and quantum teleportation of Schrödinger–cat states," *Physica Scripta*, vol. 90, no. 7, p. 074029, 2015.

[15] F. Dell'Anno, D. Buono, G. Nocerino, S. De Siena, and F. Illuminati, "Non–Gaussian swapping of entangled resources," *Quantum Information Processing*, vol. 18, p. 20, 2018.

[16] S. Takeda, M. Fuwa, P. Loock, and A. Furusawa, "Entanglement swapping between discrete and continuous variables," *Physical Review Letters*, vol. 114, p. 100501, 2015.

[17] M. B. Plbnio and S. Virmani, "An introduction to entanglement measures," *Quantum Information Computation*, vol. 7, p. 1, 2007.

[18] F. Mintert, C. Viviescas, and A. Buchleitner, *Basic Concepts of Entangled States*, 2009.

[19] S. Tserkis and T. C. Ralph, "Quantifying entanglement in two–mode gaussian states," *Physical Review A*, vol. 96, p. 062338, 2017.

[20] G. Vidal and R. Werner, "Computable measure of entanglement," *Physical Review A*, vol. 65, p. 032314, 2002.

[21] S. Kamaruddin and J. S. Shaari, "Device–independent quantum key distribution using single–photon entanglement," *Europhysics Letters*, vol. 110, p. 260, 2015.

[22] K. Banaszek and K. Wódkiewicz, "Testing quantum nonlocality in phase space," *Physical Review Letters*, vol. 82, p. 2009, 1999.

[23] S.-K. Liao, W.-Q. Cai, W.-Y. Liu, L. Zhang, Y. Li, J.-G. Ren, J. Yin, Q. Shen, Y. Cao, Z.-P. Li *et al.*, "Satellite–to–ground quantum key distribution," *Nature*, vol. 549, no. 7670, p. 43, 2017.

[24] C. H. Bennett, G. Brassard, C. Crépeau, R. Jozsa, A. Peres, and W. K. Wootters, "Teleporting an unknown quantum state via dual classical and Einstein–Podolsky–Rosen channels," *Physical Review Letters*, vol. 70, p. 1895, 1993.

[25] J. L. Park, "The concept of transition in quantum mechanics," *Foundations of Physics*, vol. 1, no. 1, p. 23, 1970.

[26] D. Dieks, "Communication by EPR devices," *Physics Letters A*, vol. 92, no. 6, p. 271, 1982.

[27] W. K. Wootters and W. H. Zurek, "A single quantum cannot be cloned," *Nature*, vol. 299, p. 802, 1982.

[28] H. Takesue, S. W. Nam, Q. Zhang, R. H. Hadfield, T. Honjo, K. Tamaki, and Y. Yamamoto, "Quantum key distribution over a 40 dB channel loss using superconducting single photon detectors," *Nature Photonics*, vol. 1, p. 343, 2007.

[29] B. Korzh, C. C. W. Lim, R. Houlmann, N. Gisin, M. J. Li, D. Nolan, B. Sanguinetti, R. Thew, and H. Zbinden, "Provably secure and practical quantum key distribution over 307 km of optical fibre," *Nature Photonics*, vol. 9, no. 3, p. 163, 2015.

[30] C.-Z. Peng, T. Yang, X.-H. Bao, J. Zhang, X.-M. Jin, F.-Y. Feng, B. Yang, J. Yang, J. Yin, and Q. Zhang, "Experimental free–space distribution of entangled photon pairs over 13 km: Towards satellite–based global quantum communication," *Physical Review Letters*, vol. 94, no. 15, p. 150501, 2005.

[31] H. Do, R. Malaney, and J. Green, "Hybrid entanglement swapping for satellite–based quantum communications," *IEEE Globecom*, p. 1, 2019.

[32] L. Vaidman, "Teleportation of quantum states," *Physical Review A*, vol. 49, p. 1473, 1994.

[33] S. L. Braunstein and H. J. Kimble, "Teleportation of continuous quantum variables," *Physical Review Letters*, vol. 80, p. 869, 1998.

[34] J. Liu, J. Li, and G. Guo, "Improving the fidelity of continuous–variable quantum teleportation by tuning displacement gain," *China Optical Letters*, vol. 1, p. 114, 2003.

[35] M. Ladislav, R. Filip, and A. Furusawa, "Continuous–variable teleportation of a negative Wigner function," *Physical Review A*, vol. 82, p. 012322, 2010.

[36] A. P. Lund, T. C. Ralph, and H. L. Haselgrove, "Fault–tolerant linear optical quantum computing with small-amplitude coherent states," *Physical Review Letters*, vol. 100, p. 030503, 2008.

[37] H. Do, R. Malaney, and J. Green, "Teleportation of a Schrödinger's–cat state via satellite–based quantum communication," *IEEE Globecom Workshop*, p. 1, 2019.

[38] J. Yin, Y. Cao, Y.-H. Li, S.-K. Liao, L. Zhang, J.-G. Ren, W.-Q. Cai, W.-Y. Liu, B. Li, H. Dai *et al.*, "Satellite–based entanglement distribution over 1200 kilometers," *Science*, vol. 356, no. 6343, p. 1140, 2017.

[39] N. Hosseinidehaj, Z. Babar, R. Malaney, S. X. Ng, and L. Hanzo, "Satellite–based continuous–variable quantum communications: State–of–the–art and a predictive outlook," in *IEEE Communications Surveys Tutorials*, vol. 21, no. 1, 2019, p. 881.

[40] D. Y. Vasylyev, A. A. Semenov, and W. Vogel, "Toward global quantum communication: Beam wandering preserves nonclassicality," *Physical Review Letters*, vol. 108, no. 22, p. 220501, 2012.

[41] D. Vasylyev, A. A. Semenov, and W. Vogel, "Atmospheric quantum channels with weak and strong turbulence," *Physical Review Letters*, vol. 117, no. 9, p. 090501, 2016.

[42] N. Lee, H. Benichi, Y. Takeno, S. Takeda, J. Webb, E. Huntington, and A. Furusawa, "Teleportation of nonclassical wave packets of light," *Science*, vol. 332, no. 6027, p. 330, 2011.

[43] B. Schumacher, "Sending entanglement through noisy quantum channels," *Physics Review A*, vol. 54, p. 2614, 1996.

[44] Y. Guo, C. Xie, P. Huang, J. Li, L. Zhang, D. Huang, and G. Zeng, "Channel–parameter estimation for satellite–to–submarine continuous-variable quantum key distribution," *Physical Review A*, vol. 97, no. 5, p. 052326, 2018.

[45] L. C. Andrews and R. L. Phillips, *Laser beam propagation through random media*. SPIE press Bellingham, WA, 2005, vol. 152.

[46] V. V. Dodonov, I. A. Malkin, and V. I. Man'ko, "Even and odd coherent states and excitations of a singular oscillator," *Physica*, vol. 72, no. 3, p. 597, 1974.

[47] T. C. Ralph, A. Gilchrist, G. J. Milburn, W. J. Munro, and S. Glancy, "Quantum computation with optical coherent states," *Physical Review A*, vol. 68, p. 042319, 2003.

[48] J. Brask, I. Rigas, E. Polzik, U. Andersen, and A. Sorensen, "A hybrid long–distance entanglement distribution protocol," *Physical Review Letters*, vol. 105, p. 160501, 10 2010.

[49] N. Sangouard, C. Simon, N. Gisin, J. Laurat, R. Tualle-Brouri, and P. Grangier, "Quantum repeaters with entangled coherent states," *Journal of the Optical Society of America B*, vol. 27, no. 6, p. A137, 2010.

[50] K. Park and H. Jeong, "Entangled coherent states versus entangled photon pairs for practical quantum–information processing," *Physical Review A*, vol. 82, p. 062325, 2010.

[51] H. Do, R. Malaney, and J. Green, "Satellite–based distribution of hybrid entanglement," *Quantum Engineering*, p. 776, 2021.

[52] P. Huang, G. He, J. Fang, and G. Zeng, "Performance improvement of continuous–variable quantum key distribution via photon subtraction," *Physical Review A*, vol. 87, no. 1, p. 012317, 2013.

[53] H. Le Jeannic, A. Cavaillès, J. Raskop, K. Huang, and J. Laurat, "Remote preparation of continuous–variable qubits using loss-tolerant hybrid entanglement of light," *Optica*, vol. 5, no. 8, p. 1012, 2018.

[54] A. Cavaillès, H. Le Jeannic, J. Raskop, G. Guccione, D. Markham, E. Diamanti, M. D. Shaw, V. B. Verma, S. W. Nam, and J. Laurat, "Demonstration of Einstein–Podolsky–Rosen steering using hybrid continuous– and discrete–variable entanglement of light," *Physical Review Letters*, vol. 121, p. 170403, 2018.

[55] C. Branciard, E. G. Cavalcanti, S. P. Walborn, V. Scarani, and H. M. Wiseman, "One–sided device–independent quantum key distribution: Security, feasibility, and the connection with steering," *Physical Review A*, vol. 85, p. 010301, 2012.

[56] H. L. Yin and Z. B. Chen, "Coherent–state–based twin–field quantum key distribution," *Scientific Reports*, vol. 9, 2019.

[57] ——, "Finite–key analysis for twin–field quantum key distribution with composable security," *Scientific Reports*, vol. 9, p. 17113, 2019.

[58] S. Zhang, "Improving long–distance distribution of entangled coherent state with the method of twin–field quantum key distribution," *Optical Express*, vol. 27, no. 25, p. 37087, 2019.

[59] R. E. S. Polkinghorne and T. C. Ralph, "Continuous variable entanglement swapping," *Physical Review Letters*, vol. 83, p. 2095, 1999.

[60] S. Takeda, T. Mizuta, M. Fuwa, P. van Loock, and A. Furusawa, "Deterministic quantum teleportation of photonic quantum bits by a hybrid technique," *Nature*, vol. 500, p. 315, 2013.

[61] S. Lie and H. Jeong, "Limitations of teleporting a qubit via a two–mode squeezed state," *Photonics Research*, vol. 7, p. A7, 2019.

[62] T. Ide, H. Hofmann, T. Kobayashi, and A. Furusawa, "Continuous variable teleportation of single photon states," *Physical Review A*, vol. 65, p. 012313, 2001.

[63] S. M. Zhao, J. Leach, L. Y. Gong, J. Ding, and B. Y. Zheng, "Aberration corrections for free–space optical communications in atmosphere turbulence using orbital angular momentum states," *Optics Express*, vol. 20, no. 1, p. 452, 2012.

[64] M. Li, M. Cvijetic, Y. Takashima, and Z. Yu, "Evaluation of channel capacities of OAM–based FSO link with real–time wavefront correction by adaptive optics," *Optics Express*, vol. 22, p. 31337, 2014.

[65] Y. Lim, J. Joo, T. P. Spiller, and H. Jeong, "Loss–resilient photonic entanglement swapping using optical hybrid states," *Physical Review A*, vol. 94, p. 062337, 2016.

[66] A. E. Ulanov, D. Sychev, A. A. Pushkina, I. A. Fedorov, and A. I. Lvovsky, "Quantum teleportation between discrete and continuous encodings of an optical qubit," *Physical Review Letters*, vol. 118, p. 160501, 2017.

[67] G. Guccione, T. Darras, H. Le Jeannic, V. B. Verma, S. W. Nam, A. Cavaillès, and J. Laurat, "Connecting heterogeneous quantum networks by hybrid entanglement swapping," *Science Advances*, vol. 6, no. 22, p. 1, 2020.

[68] M. Takeoka, M. Sasaki, and M. Ban, "Continuous variable teleportation as a quantum channel," *Optics and Spectroscopy*, vol. 94, p. 675, 2003.

[69] O. Morin, K. Huang, J. Liu, H. Le Jeannic, C. Fabre, and J. Laurat, "Remote creation of hybrid entanglement between particle–like and wave–like optical qubits," *Nature Photonics*, vol. 8, p. 570, 2013.

[70] A. E. B. Nielsen and K. Mølmer, "Transforming squeezed light into a large–amplitude coherent–state superposition," *Physical Review A*, vol. 76, p. 043840, 2007.

[71] A. Gilchrist, K. Nemoto, W. J. Munro, T. C. Ralph, S. Glancy, S. L. Braunstein, and G. J. Milburn, "Schrödinger cats and their power for quantum information processing," *Journal of Optics B: Quantum and Semiclassical Optics*, vol. 6, no. 8, p. S828, 2004.

[72] R. C. Parker, J. Joo, M. Razavi, and T. P. Spiller, "Hybrid photonic loss resilient entanglement swapping," *Journal of Optics*, vol. 19, no. 10, p. 104004, 2017.

[73] R. C. Parker, J. Joo, and T. P. Spiller, "Photonic hybrid state entanglement swapping using cat state superpositions," *Proceedings of the Royal Society A: Mathematical, Physical and Engineering Sciences*, vol. 476, no. 2243, p. 20200237, 2020.

[74] F. Dell'Anno, S. de Siena, and F. Illuminati, "Realistic continuous-variable quantum teleportation with non–Gaussian resources," *Physical Review A*, vol. 81, p. 145, 2010.

[75] R. J. Glauber, "Coherent and incoherent states of the radiation field," *Physical Review Journals Archive*, vol. 131, p. 2766, 1963.

[76] E. C. G. Sudarshan, "Equivalence of semiclassical and quantum mechanical descriptions of statistical light beams," *Physycal Review Letter*, vol. 10, p. 277, 1963.

[77] F. A. M. de Oliveira, M. Kim, P. Knight, and V. Buek, "Properties of displaced number states," *Physical Review A*, vol. 41, p. 2645, 1990.

[78] P. Marian and T. Marian, "Continuous–variable teleportation in the characteristic–function description," *Physical Review A*, vol. 74, p. 042306, 2006.

[79] R. C. Parker, "A loss resilient entanglement swapping protocol using non–classical states of light," Ph.D. dissertation, University of York, 2018. [Online]. Available: etheses.whiterose.ac.uk/22822

[80] K. Kreis and P. van Loock, "Classifying, quantifying, and witnessing qudit–qumode hybrid entanglement," *Physical Review A*, vol. 85, p. 032307, 2012.

[81] Y.-B. Sheng, L. Zhou, and G. Long, "Hybrid entanglement purification for quantum repeaters," *Physical Review A*, vol. 88, p. 022302, 2013.